Northumbria University
NEWCASTLE

DOCTORAL THESIS

Wintertime land surface albedo of forested environments

Johanna T. Malle

Supervisors: Dr. Nick Rutter, Dr. Tobias Jonas, Dr. Leanne Wake

A thesis submitted in partial fulfilment of the requirements of the University of Northumbria at Newcastle for the degree of Doctor of Philosophy

January 2021

Abstract

Forest canopies are complex 3-D structures at the interface between the atmosphere and the land surface which greatly affect radiative processes, especially across seasonally snow-covered domains. The increase in process complexity associated with these areas continues to be a source of uncertainty in land surface modelling. Model development has been hampered by a limited amount of in-situ radiation measurements, together with contrasting spatial scales of measurements and model resolution. Here, a bespoke cable car system was used to measure incoming and outgoing shortwave and longwave radiation below an evergreen forest stand, while an uncrewed aerial vehicle (UAV) system, equipped with up- and down-looking shortwave radiation sensors, was used to measure land surface albedo (LSA) above alpine, sub-alpine and boreal forest stands. These in-situ measurements were combined with point-scale simulations of the Community Land Model Version 5.0 (CLM5), enabling process level assessment of algorithms used within global climate modelling frameworks. Analysis of diurnal radiation patterns, obtained via the cable car and UAV systems, revealed canopy structural shading of the snow surface as a main control on both the sub-canopy shortwave radiation budget and overall LSA. Furthermore, diurnal patterns of measured LSA revealed a strong dependency on both solar azimuth and zenith angles. Corresponding CLM5 simulations did not adequately represent the measured spatial and temporal variability in LSA and sub-canopy incoming shortwave radiation. In sparse forested environments, CLM5 performed especially poorly, as LSA was overestimated by up to 66%. The use of effective Plant Area Index (PAI) values as a simple first-order correction for this discrepancy between measured and simulated LSA substantially improved model results (64-76% RMSE reduction). That being said, such large biases suggest the need for a more robust solution, especially as the use of effective PAI values did not improve the ability of CLM5 to replicate diurnal variability in LSA and sub-canopy shortwave radiation. Hence, a time-varying transmissivity for direct shortwave radiation was integrated into CLM5, meaning that directionality of solar irradiance could be taken into account. Results with this modified version of CLM5 showed measured variability of sub-canopy incoming shortwave radiation was replicated more accurately, suggesting this approach may help to decrease uncertainty in LSA simulations across seasonally snow-covered forested environments. This has far reaching implications for simulations of the snow albedo feedback strength over the entire Northern Hemisphere Extratropics.

Contents

List of Figures

List of Tables

List of Abbreviations

AWS	Automatic Weather Station
CC	Canopy coverage
CESM2	Community Earth System Model version 2.0
CH	Switzerland
CHM	Canopy Height Model
CLM5	Community Land Model Version 5.0
CMIP	Coupled Model Intercomparison Project
DSM	Digital Surface Model
DTM	Digital Terrain Model
ECV	Essential Climate Variables
FIN	Finland
GCM	General Circulation Model
GHF	Ground heat flux
HS	Snow depth
LAI	Leaf Area Index
LiDAR	Light detection and ranging
LSA	Land surface albedo
LSM	Land Surface Models
LWR	Longwave radiation
MAE	Mean Absolute Error
MaTH	Maximum tree height
MODIS	Moderate Resolution Imaging Spectroradiometer
MTH	Mean tree height
NCAR	National Center for Atmospheric Research
NET	Needle-leaf evergreen tree
PAI	Plant Area Index
PCH	Phase change heat flux
PFT	Plant Functional Type

PHF	Precipitation heat flux
PTCLM5	Point version of CLM5
RMSE	Root Mean Square Error
ROS	Rain on snow
RQ	Research question
SAF	Snow Albedo Feedback
SAI	Stem Area Index
SCE	Snow Cover Extent
SNICAR	SNow ICe and Aerosol Radiation model
SWE	Snow Water Equivalent
SWR	Shortwave radiation
THF	Turbulent heat fluxes
UAV	Uncrewed Aerial Vehicle
VF	View fraction
WP	Waypoint

List of Symbols

ρ_b	Bulk snow density [kg m^{-3}]
ρ_{bf}	Fresh snow density [kg m^{-3}]
SWE	Snow water equivalent [mm]
HS	Snow depth [m]
$\frac{dU_s}{dt}$	Internal energy of the snow pack [W m^{-2}]
α	Land surface albedo [-]
σ	Stefan Bolzmann constant [W m^{-2} K^{-4}]
H_S	Sensible heat flux [W m^{-2}]
H_L	Latent heat flux [W m^{-2}]
LAI	Leaf Area Index [-]
LWR	Longwave radiation [W m^{-2}]
SWR	Shortwave radiation [W m^{-2}]
LWR$_{atm}$	Longwave Radiation of atmosphere [W m^{-2}]
PCH	Energy of snowpack phase changes [W m^{-2}]
GHF	Heat exchange with the ground [W m^{-2}]
PHF	Precipitation heat flux [W m^{-2}]
P$_s$	Surface air pressure [Pa]
ρ_a	Density of air [kg m^{-3}]
Q	Specific humidity at reference height [g kg^{-1}]
Q$_0$	Specific humidity at snow surface [g kg^{-1}]
c_{pa}	Specific heat of air at constant pressure [J kg^{-1} K^{-1}]
L_{vi}	Latent heat of sublimation for ice [J kg^{-1}]

C_H	Bulk transfer coefficients for heat [-]
C_Q	Bulk transfer coefficients for water vapour [-]
u	Wind speed at reference height [m s^{-1}]
VF_{Sky}	Sky View Fraction [-]
ε	Emissivity [-]
ε_c	Emissivity of the canopy [-]
T_c	Canopy temperature [K]
T_{air}	Temperature of the air [K]
T_{atm}	Temperature of the atmosphere [K]
k	Extinction factor to account for clumping of canopy elements [-]
θ	Solar zenith angle [°]
$\overline{\mu}$	Average inverse diffuse optical depth per unit plant area [-]
K	Optical depth of the direct solar beam per unit plant area [-]
β	Upscatter parameter for diffuse radiation [-]
β_0	Upscatter parameter for direct radiation [-]
β_{snow}	Upscatter parameter for intercepted snow [-]
ω	Scattering coefficient [-]
ω_{leaf}	Scattering coefficient for leaves [-]
ω_{snow}	Scattering coefficient for intercepted snow [-]
$frac_{interc}$	Canopy intercepted snow fraction [-]
α_{gr}	Ground albedo [-]
α_{soil}	Soil albedo [-]
α_{snow}	Snow albedo [-]
$fsno$	Snow cover fraction [-]
uaf	Wind speed within the canopy [m s^{-1}]
u_m	Wind speed at an open area [m s^{-1}]
u^*	Friction velocity [m s^{-1}]

ram	Aerodynamical resistance [s m^{-1}]
z_0	Roughness length of ground [m]
$csoil_b$	Turbulent transfer coefficient over bare soil [-]
$csoil_c$	Turbulent transfer coefficient for soil under canopy [-]
$csoil_{cn}$	Turbulent transfer coefficient for less-than-dense canopy [-]
w	Canopy density [-]
$FSno$	Fractional snow covered area [-]
σ_{topo}	Standard deviation of topography within a grid cell [-]
n_{melt}	Snow covered area shape function [-]
W	Simulated snow water equivalent at current time step[mm]
W_{max}	Maximum simulated SWE of the snow season [mm]
$snocan$	Amount of intercepted snow in the canopyn [mm]
$fcansno$	Fraction of canopy that is snow covered [-]
$fveg_{nosno}$	Fraction of vegetation that is not covered by snow [-]
$vegt$	Fraction of vegetation that is not covered by snow * PAI [-]
$dewmx$	Maximum allowed dew [mm]
$dewmxi$	Inverse of maximum allowed dew [mm^{-1}]
τ	Transmittance of shortwave radiation [-]
τ_{dir}	Transmittance of direct beam shortwave radiation [-]
τ_{dif}	Transmittance of diffuse beam shortwave radiation [-]
τ_t	Time-varying transmissivity [-]

Declaration of Authorship

I declare that the work contained in this thesis has not been submitted for any other award and that it is all my own work. I also confirm that this work fully acknowledges opinions, ideas and contributions from the work of others. Any ethical clearance for the research presented in this thesis has been approved.

I declare that the Word Count of this thesis is 37 282.

Name: Johanna Teresa Malle

Signature: Johanna Malle

Date: March 8, 2021

At the time of submission, the contents of three chapters in this thesis have either been published or are under review in peer-reviewed journals:

Chapter 4 is published as: Malle, J., Rutter N., Mazzotti, G., and Jonas, T (2019). Shading by Trees and Fractional Snow Cover Control the Subcanopy Radiation Budget. *Journal of Geophysical Research:Atmospheres*, 124(6), 3195–3207, doi: 10.1029/2018JD029908.

Chapter 5 and Chapter 6 are in review as: Malle, J., Rutter N., Webster, C., Mazzotti, G., Wake, L. and Jonas, T (2020). Effect of forest canopy structure on wintertime Land Surface Albedo: Evaluating CLM5 simulations with in-situ measurements. *Journal of Geophysical Research:Atmospheres*, in review.

Acknowledgements

First, I would like to thank Dr. Nick Rutter, Dr. Tobias Jonas and Dr. Leanne Wake, who formed a very complementary supervision team. Thank you for your guidance and support throughout the course of this project, for reassuring me at times and for pushing me at others. Needless to say that this thesis would have not happened without all your help.

This work was supported by an RDF studentship from Northumbria University, which I am grateful for. The field campaign in Sodankylä received funding from INTERACT under the European Union H2020 Grant Agreement No.871120, project IME4Rad. I'd like to thank Dr. Steve Hancock for collecting and providing TLS data in Sodankylä, and Dr. Richard Essery for his help in the field and for being a source of calmness during our campaign. I am also grateful to Dr. Anna Kontu and Dr. Leena Leppänen for their campaign planning help, for their hospitality at FMI and for providing meteorological and snow survey data.

I'm thankful to the entire snow-hydrology team at SLF, for interesting discussions and patient explanations, alongside extended coffee breaks. A special thank you goes to the forest snow sub-team, Dr. Clare Webster and Dr. Giulia Mazzotti, whose work ethics and forest-snow knowledge are a constant source of inspiration. I'm especially thankful to Dr. Clare Webster for teaching me her drone knowledge and to Dr. Giulia Mazzotti for all the joined field work planning, and the good collaboration with both of them in general. A lot of field work was conducted in Switzerland, field assistance from students and interns of the snow hydrology group was greatly appreciated, namely of Elena Stautzenbach, Luca Iacolettig, Sarah Barr, Mira Ehrler, Benedikt Friedrich, Robin Maedel, Kalliopi Koutantou and Eliane Brändle. I would also like to express my gratitude to the SLF electronics and mechanics workshop crew, especially Marco Collet, Andi Moser and Laurens Perseus, for all their help, patience and flexibility during the development of the field systems.

The highs are higher and the lows are more bearable/often disappear when you are surrounded by the right people. From office mates in Newcastle, to fellow PhD students at SLF, to climbing and skiing partners, to friends from around the world - thank you from the bottom of my heart, y'all have and continue to enrich my life immensely. I feel very

lucky to have so many wonderful people in my life, one of which I am especially grateful for.

Last, but definitely not least, I want to express my deepest gratitude to my family. Thank you Luki and Toni for all the laughter and distractions, and for just being the best siblings out there. Thank you mum and dad for all your unwavering support, for all the things you have taught me and for always leading by example. Thank you for always believing in me.

Chapter 1

Introduction

1.1 Rationale and aims

The earth's climate system is constantly changing as a result of both natural and anthropogenic influences (Karl and Trenberth, 2003) but more recently the rate of change has been observed to be accelerating. Global mean temperatures in the year 2020 are 1.2±0.1°C higher than during the pre-industrial era (WMO, 2020) and warming has exceeded an average of 0.25°C decade^{-1} between 1979-2012 (Hartmann et al., 2013). The main driver of these changes are anthropogenic (Vaughan et al., 2013, Medhaug et al., 2017) through the release of greenhouse gases into the atmosphere, altering the earth's energy budget via the greenhouse effect (Petit et al., 1999, Saunois et al., 2016, Zhang et al., 2017). This anthropogenic climate change will have substantial socioeconomic consequences in the future, as globally averaged temperatures are predicted to continue to rise over the next century (e.g. Stott, 2016). These include sea level rise (Church and White, 2006, Nerem et al., 2018), food and water security (Gudmundsson et al., 2017, Pritchard, 2019), changes in the frequency and intensity of extreme weather events (Stott, 2016, Burrell et al., 2020) and reduction in natural capital (e.g. Hoegh-Guldberg et al., 2007). These impacts and many others drive an urgent need to better understand the global and regional effects of a changing climate in order to help mitigate and prepare for them.

The continuous warming trend has profound implications for the cryosphere, as it leads to decreases in the Greenland and Antarctic ice sheets (Gregory, 2004, Pattyn et al., 2018) and a diminished snow cover across the northern hemisphere (Derksen and Brown, 2012, Kunkel et al., 2016, Pulliainen et al., 2020). Snow cover reduction has been observed in alpine (Hock et al., 2019) and arctic regions (Meredith et al., 2019), and can be largely attributed to a temperature-induced shift in precipitation patterns from snow towards rain (e.g. Hamlet et al., 2005, Barnett et al., 2008, Berghuijs et al., 2014). It is, however,

difficult to synthesize these changes, as snow packs in different climatic zones show different sensitivities to climate warming (López-Moreno et al., 2020).

The presence or absence of snow, which profoundly alters energy transfer at the Earth's surface, is a key state variable influencing the climate system. The amount of precipitation falling as snow, the length of snow cover seasons, the onset date of spring melt and the interlinked melt-rates are all important climate indicators (Musselman et al., 2017). In turn, relationships have been identified between large weather phenomena (e.g. North Atlantic Oscillation, monsoon circulation) and snowfall events in preceding seasons (e.g Hahn and Shukla, 1976, Zhao and Moore, 2004, López-Moreno et al., 2011), while regional climate change itself can be driven by snow feedbacks (Hall, 2004, Thackeray and Fletcher, 2016). Due to the high reflectivity (albedo) of snow relative to other elements of the earth surface (Flanner et al., 2011), a shrinking snow cover will result in more energy absorbed by the earth, reinforcing a positive feedback mechanism which is commonly referred to as Snow Albedo Feedback (SAF). On a global scale, SAF is assumed to have a minor influence on climate (Thackeray and Fletcher, 2016). However, SAF drives regional climate change over the northern hemisphere extratropics (Hall, 2004, Thackeray and Fletcher, 2016), where longer snow-free seasons exert the strongest feedback (Chapin, 2005). SAF was also found to be the second largest contributing mechanism to a phenomenon termed Arctic Amplification (Pithan and Mauritsen, 2014), whereby temperatures in high-latitudes are rising at up to twice the speed of the global average (Serreze et al., 2009), resulting in unprecedented changes in northern high latitude environments (Serreze et al., 2000, Swann et al., 2010).

Earlier seasonal snow melt-out also impacts the biosphere, leading to an earlier start of ecosystem functioning across boreal forests (Pan et al., 2011). The resulting increase in photosynthesis enhances carbon uptake (3.7% per decade between 1979 and 2015), creating a negative feedback on radiative climate forcing (Pulliainen et al., 2017). Conversely, amplified air temperatures increase permafrost thaw (Bonfils et al., 2012), which leads to increased mobilization of carbon previously stored in permafrost (Schuur et al., 2015, Natali et al., 2019). Hence, the relationship between snow cover, temperature and carbon emissions in high latitude regions is an important but complex part of the earth's carbon cycle.

The Global Climate Observing System (GCOS, https://gcos.wmo.int/) has identified a group of 54 "Essential Climate Variables" (ECV), including both Land Surface Albedo (LSA), defined as the fraction of incoming shortwave radiation that is reflected by the surface of the earth (Dickinson, 1983), and Snow Cover Extent (SCE), defined as the area of land covered by snow. This further underlines the importance of LSA and SCE for monitoring climate change and the critical role those two inter-related variables have in

regulating the energy balance of the planet. Variability of SCE in a changing climate has presented substantial socio-economic challenges, as snow stores water during winter, and is a fresh-water resource during spring and summer. Agricultural irrigation often heavily relies on snow-melt for food production (Qin et al., 2020), while more than one sixth of the world's population is dependent on water from glaciers or snow melt (Barnett et al., 2005), highlighting the importance of glaciers and snow for human water demand (Mankin et al., 2015, Pritchard, 2019). Consequently, accurate forecasting of hydrological change is imperative for future water management. Furthermore, the aforementioned snow to rain transition in precipitation has substantial financial implications, with an estimated annual cost of between 10.8-48.6 billion US Dollars (Sturm et al., 2017).

The ability of climate models to accurately simulate SCE and LSA is critical in order to forecast SAF under future climate scenarios. Consensus between different General Circulation Models (GCMs), however, remains small: Qu and Hall (2007) highlighted a large inter-model spread in SAF using simulations from the Third Coupled Model Intercomparision Project (CMIP3), which persisted into the more recent generation of models participating in the CMIP5 (Fletcher et al., 2015). The spread in simulated snow surface albedo across CMIP5 models ranged from 0.39 to 0.75, which consequently leads to a spread in SAF from 0.18 - 0.78 W m^{-2} K^{-1} across the northern hemisphere (Qu and Hall, 2014). Much inter-model spread in SAF has been attributed to snow-vegetation masking, which is sensitive to the parameterisation scheme each GCM applies to represent vegetation structure in snow-covered areas (Essery et al., 2013, Qu and Hall, 2014). This discrepancy remained evident through both CMIP3 and CMIP5 (Wang, Erb, Schaaf, Sun, Liu, Yang, Shuai, Casey and Román, 2016, Mudryk et al., 2020). Given that during peak annual global snow-extent, almost half of the terrestrial snow-covered area overlaps with forests (Kim et al., 2017), it is paramount to reduce such uncertainties in land surface model (LSM) albedo simulations.

Accurate simulations of land surface-atmosphere energy fluxes and melt water runoff from snow-dominated forested watersheds also require reliable estimates of radiative transfer processes through vegetation canopies (Lawler and Link, 2011, Seyednasrollah and Kumar, 2014). Evaluation and development of simulated LSA and radiative transfer through forest canopies has been hampered by spatial discontinuities between measurement scale and model resolution. GCMs are usually run at coarse horizontal resolutions ($\sim$50 – 200 km grid cells), leaving satellite data as the only way to assess simulated LSA (e.g. Wang et al., 2004, Malmros et al., 2018). However, forest heterogeneity (canopy gaps and edges) is not commonly resolved by globally available satellite data (e.g. MODIS MOD10A1 500m grids). While higher resolution satellite albedo retrievals are becoming more widely available (e.g. 30m LANDSAT or sub-meter scale Worldview4 by Digital

Globe), the spatial and temporal resolution is still not high enough for such data to be used as a benchmark to evaluate variability in simulations of wintertime LSA and sub-canopy radiation. Consequently, high quality in-situ radiation measurements are still indispensable to evaluate and improve process-scale understanding of radiative processes through a canopy. However, the use of a single stationary radiometer below the canopy is not adequate to represent the heterogeneity of a forest stand (Link et al., 2004), nor is a single tower measuring LSA above the canopy. Such point-scale measurements struggle to represent areas greater than the sensor footprint, which would be required to represent the spatially integrated perspective of a coarse grid cell. New observational techniques capable of capturing the spatially and temporally highly variable radiation regime of a forest are hence needed to improve radiation parametrization of current land surface model schemes for forested regions (Wild et al., 2001, Qu and Hall, 2014).

This thesis addresses this research gap by presenting highly temporally and spatially resolved measurements of sub-canopy radiation and of LSA above forest canopies at six different forested sites in boreal, alpine and sub-alpine environments. Furthermore, the aim of this research is to evaluate the representation of these parameters and processes in a state-of-the-art, physically-based LSM. Above-canopy LSA measurements from a bespoke airborne platform allowed variable measurement heights and flexibility to obtain measurements at multiple locations above a forest canopy. A moving cable car system making below-canopy radiation measurements allowed similar spatially distributed measurements. The gap to coarse grid cell model resolution was closed by combining such spatially distributed measurements with point-scale simulation of the Community Land Model 5.0, the land component of the Community Earth System Model version 2.0 (CESM2). This approach allowed evaluation of algorithms used within global climate modelling frameworks at the process level. In the remainder of this chapter, a general background on forest-snow-atmosphere interactions is presented alongside the limitations of their representation in LSM. Finally, objectives and research questions are stated and the structure of this thesis is described to conclude this chapter.

1.2 Forest-snow-atmosphere interactions

Annual maximum global snow cover extent is approximately 47 x 10^6 km^2, covering more than 40% of the terrestrial Northern Hemisphere (Robinson and Frei, 2000, Lemke et al., 2007). This has profound implications for energy and mass exchanges between the lower atmospheric boundary layer and the land surface. Heat and moisture exchanges are largely controlled by the high reflectivity (Flanner et al., 2011) and the low thermal conductivity properties of snow (Zhang, 2005). Where seasonal snow cover overlaps with forested

environments ($\sim$ 9 x 10^6 km^2, Rutter et al., 2009), the presence of trees exerts a principal control on snow dynamics (Musselman and Pomeroy, 2017, Roth and Nolin, 2017), which further impacts eco-hydrological processes (Trujillo et al., 2012, Lundquist et al., 2013). In turn, snow dynamics also directly affect forests by influencing forest productivity and tree growth (Carlson et al., 2017, Sanmiguel-Vallelado et al., 2021).

At a local scale, forested environments create micro-climates, causing high temporal and spatial variability in snow dynamics (Ellis et al., 2011, Lundquist et al., 2013), as every mass and energy flux to the snow pack is altered compared to open areas. Sub-canopy radiation, controlled by forest heterogeneity, is a major cause of variability in sub-canopy snow dynamics (Link and Marks, 1999, Sicart et al., 2004, Ellis et al., 2011). Compared to open areas, a forest canopy attenuates shortwave radiation and enhances longwave radiation (thermal emissions) by absorption of shortwave and re-emittance as longwave energy (e.g. Sicart et al., 2004, Webster et al., 2016*b*), further affecting timing, intensity, and duration of snow melt (Male and Granger, 1981). Forests also reduce wind speeds, which leads to suppressed turbulent fluxes and often causes forests to act as cold air sinks (Link and Marks, 1999, Webster et al., 2016*b*).

Complex snow dynamics in forests are largely controlled by the 3-D canopy structure (Varhola et al., 2010), resulting in small-scale variability of energy fluxes, which are challenging to represent in modelling frameworks. The Snow Model Inter-comparison Project's second phase (SnowMIP2) evaluated 33 snow models and identified major deficiencies of forest snow process representations (Rutter et al., 2009, Essery et al., 2009). Since then, knowledge of forest snow processes has been substantially improved by an abundance of field based studies (Mahat et al., 2013, Webster et al., 2016*b*, Roth and Nolin, 2017, Mazzotti et al., 2019, Sanmiguel-Vallelado et al., 2020, Hotovy and Jenicek, 2020) which have led to enhanced representation of forest snow dynamics in snow models across multiple scales (Mahat et al., 2013, Gouttevin et al., 2015, Broxton et al., 2015, Todt et al., 2018, Sun et al., 2018, Mazzotti, Essery, Moeser and Jonas, 2020). Despite much progress, one limiting factor remains the representation of the complex 3-D forest canopy structure in land surface schemes of Earth System Models. Although some model developments have started to incorporate 3-D canopy structures (e.g. Yuan et al., 2014), it remains a model development challenge in most land surface schemes. Furthermore, some CMIP5 models continue to use unrealistic snow albedo values (Thackeray et al., 2019), together with often unrealistic vegetation parameters, further resulting in erroneous LSA simulations (Loranty et al., 2014, Wang, Erb, Schaaf, Sun, Liu, Yang, Shuai, Casey and Román, 2016).

From an overall land surface perspective, e.g. influencing the earth's radiation budget at the top of the atmosphere, the low albedo of trees has the potential to mask high snow

albedo (Bonan, 2008), decreasing the overall reflectivity of the land surface (Betts and Ball, 1997), and resulting in a warming effect on climate (Abe et al., 2017). However, over complex forested land surfaces, reflected shortwave radiation is strongly modulated by canopy structural shading of snow-covered ground (Webster and Jonas, 2018). Wintertime LSA further changes in response to the spatial heterogeneity of intercepted snow in forest canopies (Bartlett and Verseghy, 2015), canopy species (Kuusinen et al., 2012) and canopy structure (Bright et al., 2018). All of these components add a great deal of complexity to the overall energy budget in these regions, much of which is not captured by the current generation of climate models.

1.3 Research questions and objectives

The main aim of this research is to decrease the uncertainty in LSM parametrizations of LSA in seasonally snow-covered forested environments. Two main research questions drive this research:

1. **What processes control the sub-canopy radiation budget (RQ1a) and LSA (RQ1b) in seasonally snow-covered forested environments?**

2. **How well are radiative processes of seasonally snow-covered forested environments simulated by LSM? Are radiative regimes implemented in LSM capable of representing measured spatial and temporal variability in LSA (RQ2a) and sub-canopy radiation (RQ2b)?**

In order to answer these research questions, a combination of extensive field measurement and model experiments were required. A cable car system, providing spatio-temporal sub-canopy radiation measurements and an Uncrewed Aerial Vehicle (UAV) System with up- and down-looking shortwave radiation sensors mounted allowed processes controlling sub-canopy radiation budgets and LSA to be quantified. The following objectives were set in order to answer RQ1:

(i) Develop and use a cable car system to obtain distributed sub-canopy radiation measurements across a range of forest structures in seasonally snow-covered environments.

(ii) Analyse diurnal and seasonal radiation patterns below a forest stand and quantify: (1) the influence of shading on both outgoing shortwave radiation as well as effective albedo below forest stands, (2) the effect of solar angle and forest structure on the sub-canopy radiation budget, (3) the effect of fractional snow cover on outgoing

longwave radiation, and (4) the relative importance of shortwave and longwave radiation on the sub-canopy all-wave radiation budget.

(iii) Use an UAV system to measure above canopy LSA over a large range of discontinuous forest canopies in alpine, sub-alpine and boreal forest environments.

(iv) Investigate the effects of solar angle, intercepted canopy snow, meteorological boundary conditions and fractional snow cover on LSA.

The Community Land Model 5 (CLM5), the land component of the Community Earth System Model (CESM v2.0), was used to address RQ2. CLM5 is a state of the art, process-based land surface model that simulates carbon, nitrogen and energy exchange between the atmosphere and the terrestrial earth (Lawrence et al., 2019). The following objectives were set to answer research question 2:

(i) Apply the global-scale modelling algorithms of CLM5 to the site scale by running CLM5 in point mode (PTCLM) as a single grid-cell, forced by hourly point-scale meteorological driving data and site-specific canopy descriptors.

(ii) Evaluate CLM5 simulations of LSA spatially and temporally as a function of solar angle and canopy structure by comparing model output to in-situ UAV measurements (RQ2a).

(iii) Evaluate CLM5 simulations of radiative transfer through forest canopies using in-situ cable car measurements (RQ2b).

(iv) Assess the effectiveness of the usage of (a) an effective Plant Area Index and (b) a time-varying transmissivity for seasonal LSA simulations.

1.4 Thesis structure

The structure of this thesis is summarised here:

Chapter 2: Theoretical Background

The energy budget of seasonally snow-covered environments (open and forested) and typical representations in LSM is discussed in this chapter. Radiative transfer through forest canopies and the governing equations behind them are explained in detail. The Community Land Model 5.0 is introduced and a detailed description of its representation of forested and/or snow-covered grid cells is provided.

Chapter 3: Observational field data collection

Methods used for observational field data collection of radiation data are introduced: the custom-made cable car system for below canopy radiation measurements and the

UAV system for above-canopy LSA measurements. Meteorological reference data, necessary to provide boundary conditions (RQ1a+b) and to generate CLM5 forcing data (RQ2a+b), are discussed. All field sites located in a) sub-alpine, alpine and b) boreal forest environments are described in detail.

Chapter 4: Impacts of shading and fractional snow cover on the sub-canopy radiation budget

Results from sub-canopy radiation measurements are shown and discussed (RQ1a). Down-looking hemispherical imagery, to determine the spatial extent of shaded/sunlit snow and ground, are presented with concurrent radiation measurements, to quantify the controls shading and fractional snow cover exert on the below canopy radiation budget.

Chapter 5: Land surface albedo in seasonally snow-covered forest stands

RQ1b is addressed by investigating driving factors controlling LSA in seasonally snow-covered forest environments. UAV measurements of LSA coupled to coincident down-looking hemispherical images over snow-covered forests are used to investigate the effects of: (a) tree species, (b) intercepted snow, (c) solar angle, (d) meteorological boundary conditions, and (e) fractional snow cover on wintertime LSA.

Chapter 6: Effect of forest canopy structure on wintertime Land Surface Albedo: Evaluating CLM5 simulations with in-situ measurements

Algorithms of CLM5 are applied in point mode (PTCLM), forced by hourly point-scale meteorological driving data and site-specific canopy descriptors (RQ2a). Model performance of CLM5 is evaluated using UAV measurements of LSA.

Chapter 7: Impacts of time-varying transmissivity on CLM5 simulations of sub-canopy shortwave radiation

This chapter investigates the ability of CLM5 to replicate sub-canopy shortwave radiation (RQ2b). Additionally, a time-varying transmissivity is integrated into CLM5. Results from this modified version of CLM5 are compared to the original CLM5 simulations.

Chapter 8: Summary and Outlook

In the last chapter, the outcomes of this research are summarized. Future observational methods and priorities for model development to improve representation of forest-snow-atmosphere interactions in the next generation of LSM are suggested.

Chapter 2

Theoretical background

This chapter will present theoretical background of snow dynamics and land surface modelling in three parts. Section 2.1 focuses on snow dynamics in open, unforested areas and introduces energy balance components relevant for this study. In Section 2.2, snow dynamics of forested areas and their interaction with the atmosphere are described, with emphasis on radiative processes. Finally, Section 2.3 introduces the land surface model used in this thesis, the Community Land Model 5.0, and examines its representation of vegetation and snow, with focus on processes affecting land surface albedo.

2.1 Snow dynamics - unforested areas

At the interface between the atmosphere and the earth's surface, snow substantially influences heat and moisture exchange, with implications for the dynamics of the atmospheric boundary layer. Snow models, which are often part of land surface models, aim to numerically describe the physics at this interface using snow process parametrizations. These snow models vary greatly in sophistication and complexity, and although definitions and perceptions about model complexity vary widely (Baartman et al., 2020), existing snow models can broadly be put into three categories as suggested by Boone and Etchevers (2001):

1. Simple single snow layer models (Verseghy et al., 1993, Slater et al., 1998)
2. Multi-layer snow models with detailed internal-snow-process schemes (Anderson, 1976, Lehning et al., 2002)
3. Intermediate complexity snow models, which use simple versions of parametrizations and a minimal number of layers to enhance computational efficiency (Sun et al., 1999, Boone and Etchevers, 2001).

Ultimately, however, snow models compute energy and mass balances of snow on the ground through semi-empirical and theoretically-based equations, the physical principles of which will be discussed in the following sections.

2.1.1 Mass balance

The mass balance of a snow pack consists of two parts: accumulation and ablation of snow. Snow mass accumulation refers to periods where mass from consecutive snowfall events is cumulatively added to the mass of the snow pack. As snow on the ground is a mixture of air and all three water phases, several boundary conditions must be satisfied for snowfall to occur. Firstly, clouds must form. Clouds form in the atmosphere when air rises and cools until saturation is reached and water vapour condenses on to cloud condensation nuclei (CCN) to form droplets. In order for snow to form the cloud must then continue to cool. However, cloud droplets do not immediately freeze at 0°C and liquid can persist in a supercooled state down to temperatures as low as -38°C. Ice nucleating particles (INPs) are required for ice formation at warmer temperatures; they provide a surface for ice to form on to and so trigger the freezing of some of the supercooled droplets to form ice crystals. These crystals form in an environment that is supersaturated with respect to ice so they grow rapidly by vapour diffusion – eventually becoming snowflakes that are large enough to precipitate. Snow flakes can also grow by aggregation, where smaller crystals collide and stick together (Lohmann et al., 2016).

The amount of snow that accumulates is usually measured in millimeters of snow water equivalent (SWE), describing the amount of liquid water stored within the snow pack. SWE and snow depth (HS) are related by the bulk density of the snow (ρ_b) as

$$HS = \frac{SWE}{\rho_b} \tag{2.1}$$

HS measurements are much less time consuming to obtain than SWE measurements, hence several regional parametrizations exist to estimate SWE based on measurements of HS and estimates of ρ_b (e.g. Jonas et al., 2009, Sturm et al., 2010). Fresh snow density largely depends on the climate and on prevalent air temperatures; Hedstrom and Pomeroy (1998) found it to to vary from 68 to 143 kg m^{-3} in a dry climate in northern Canada. While each snow model uses different parametrizations for ρ_b, the Flexible Snow Model (FSM, Essery, 2015), for example, sets fresh snow density (ρ_{bf}) to 100 kg m^{-3}, which increases with time as the snow pack settles, until maximum cold snow (300 kg m^{-3}) or wet snow values (500 kg m^{-3}) of snow density are reached. If rain on snow (ROS) events occur and rain refreezes within the snow pack, higher densities can be reached. In open snow areas with high exposure to wind, blowing snow fluxes further affect the mass balance

of the snow pack (Mott et al., 2010), a redistribution effect that is often neglected in snow models used for larger scale and spatially distributed applications (Xie et al., 2019). Sublimation of the blowing snow and the associated mass loss additionally contribute to wind redistribution effects in open environments (Male and Granger, 1981).

Ablation refers to the removal of snow water equivalent (SWE) from the land surface. If there is sufficient energy to warm the surface layer above the melting point of snow (0°C), snow melt can occur. It is a two-step process of warming, then melting, which is usually driven by a net positive radiation balance. However, during patchy snow cover conditions, local advection of sensible heat can substantially contribute to ablation (Pohl et al., 2006, Mott et al., 2011). Melt occurring at the top of the snow pack often percolates through and refreezes within the snow pack, hence not every melt event will result in mass loss. Substantial melt can only occur once the entire snow pack is isothermal at 0°C; and any positive change in the internal energy of the snow pack will then result in ablation (Anderson, 1976). Ultimately, snow melt reduces the snow mass until the entire snow pack has melted.

2.1.2 Energy balance

The energy budget of the snow pack is made up of net shortwave radiation (SWR_{net}), net longwave radiation (LWR_{net}), turbulent heat fluxes (THF), energy of the snow pack phase changes (PCH), heat exchanged with the ground (GHF) and heat advected by precipitation (PHF). Principles of energy conservation mean the change in internal energy of the snow pack, per unit area and time step ($\frac{dU_s}{dt}$) in units of W m^{-2}, is the sum of those terms:

$$\frac{dU_s}{dt} = SWR_{net} + LWR_{net} + THF + PCH + GHF + PHF \tag{2.2}$$

Shortwave radiation

Shortwave radiation lies in the spectral band from 0.2 to 3.5µm, including wavelengths in the visible, near-infrared and near-ultraviolet spectra (White et al., 1998), with the majority lying between 0.3 and 2µm (Melloh et al., 2002). Under most conditions, incident shortwave radiation ($\downarrow SWR$) is the most important energy source for the snow pack, although during homogeneous cloud cover conditions, longwave radiation can be a similar or even larger energy source due to the enhanced atmospheric emissivity (Granger and Gray, 1990, Sicart et al., 2006). Top of atmosphere incoming shortwave radiation is averaged at ∼1370 W m^{-2}. Due to absorption and scattering by molecules of gases, liquids and solids in the atmosphere, this is reduced before reaching the surface of the earth. Therefore, solar beams arriving at the earth consist of a direct and a diffuse component;

direct beam if it has not been scattered while passing through the atmosphere, and diffuse otherwise, whereby the relative contribution of each is largely dependent on atmospheric conditions. On a clear-sky day, the contribution of direct beam radiation can lie between 0.4 and 0.8, while on overcast days it approaches 0 as diffuse radiation dominates (Carroll, 1985). Diurnal and seasonal change in the magnitude of direct solar radiation is controlled by the position of the sun in the sky, described by zenith and azimuth angle, and hence has a strong directional component. The converse is true for diffuse radiation, which emanates from the entire sky hemisphere, but with a varying intensity distribution. The proportion of diffuse radiation, as part of total incoming shortwave radiation, increases with increasing solar zenith angle as the potential for radiation attenuation through scattering increases with increasing solar beam path length.

Net shortwave radiation is

$$SWR_{net} =\downarrow SWR - \uparrow SWR =\downarrow SWR(1-\alpha) \tag{2.3}$$

where $\uparrow SWR$ is the upwelling shortwave radiation and α is the land surface albedo (LSA). LSA describes the spectrally integrated reflectance of the earth's surface, which is strongly dependent on optical properties, as well as on surface roughness and the angular and spectral distribution of $\downarrow SWR$. The extremely reflective nature of snow results in a large proportion of incoming shortwave radiation being reflected, as fresh snow has an overall albedo of up to 0.95, which decreases to about 0.4-0.5 as it ages (Wiscombe and Warren, 1980).

Generally, snow albedo decreases with time, and is refreshed with every snow fall. As snow ages, snow grain size of snow increases due to liquid water filling the air between grains. This metamorphosis of snow causes a reduction in snow albedo due to an increased chance of a photon of light being absorbed (Warren, 1982). From a spectral perspective, snow albedo is high in the shorter wavelengths (near-UV and visible, $<0.7\mu m$) and low for longer wavelengths (e.g. near-IR, 0.8-1.5μm). Studies have further found snow albedo to increase as zenith angle increases (Yang et al., 2008) and more recently the importance of azimuth angle for snow albedo has been highlighted by Manninen et al. (2020). Cloud cover also majorly affects the spectral distribution of the incoming solar beam, which leads an increase in snow albedo. Snow depth only affects snow albedo in very shallow snow packs, as once HS exceeds a few centimeters the ground does not contribute and snow albedo approaches its asymptotic value (Wiscombe and Warren, 1980). Albedo of snow-covered surfaces is further affected by light-absorbing particles (dust, black carbon, microbial growth), which can lead to substantial reductions in snow albedo, especially in the visible spectrum (Skiles et al., 2018).

Longwave radiation

Radiation in the spectral range from 4 to 100µm is classified as longwave radiation, which is emitted by both the atmosphere and the earth itself. Net longwave radiation consists of down-welling longwave radiation from the atmosphere ($\downarrow LWR$) and emitted longwave radiation from the earth ($\uparrow LWR$), both of which are assumed to be non-directional (i.e. isotropic):

$$LWR_{net} = \downarrow LWR - \uparrow LWR \tag{2.4}$$

Down-welling longwave radiation is dependent on atmospheric temperature, water vapour and carbon dioxide distribution. Emitted longwave radiation depends on radiative temperature and emissivity of the surface. LWR is usually calculated following the Stefan Boltzmann law, which relates radiant heat power emittance of any body to that of an idealized black body, which it states to be proportional to the forth power of its absolute temperature:

$$LWR = \sigma \epsilon T^4 \tag{2.5}$$

where σ is the Stefan Boltzmann constant ($5.67 \cdot 10^{-8} W m^{-2} K^{-4}$), ϵ is the emissivity of the body (0 - 1), and T is temperature in Kelvin (atmospheric temperature for $\downarrow LWR$ and surface temperature for $\uparrow LWR$ calculations). When calculating $\downarrow LWR$, the emissivity is strongly affected by cloud cover, as clouds are strong emitters with emissivities close to 1, while under clear sky conditions, ϵ can be as low as 0.6 (Berdahl and Fromberg, 1982). For calculation of $\uparrow LWR$, snow behaves almost as a perfect black body, with ϵ generally assumed to be as high as 0.98 (Warren, 1982).

Turbulent fluxes

Turbulent eddies in the surface boundary layer are responsible for heat fluxes, where turbulent mixing of air molecules transfers heat and moisture to and from the snow surface (Morris, 1989). Turbulent heat fluxes are partitioned into sensible (H_S) and latent heat flux (H_L), where sensible heat fluxes are associated with convection and driven by the temperature gradient between the snow surface and the atmosphere, and latent heat fluxes are driven by differences in vapour pressure between the surface and the atmosphere and is therefore related to the phase change of water. Hence, sensible and latent heat fluxes can be described by the covariance of vertical air velocity with changes in temperature (T) and specific humidity (Q) respectively, which are approximated by logarithmic profiles of temperature, humidity and wind above the surface.

Turbulent fluxes are calculated as:

$$H_S = \rho_a c_{pa} C_H u (T_a - T_0) \tag{2.6}$$

$$H_L = \rho_a L_{vi} C_Q u(Q - Q_0) \tag{2.7}$$

where ρ_a is the density of air, c_{pa} is the specific heat of air at constant pressure (1.01 x 10^3 J kg^{-1} K^{-1}), L_{vi} is the latent heat of sublimation for ice (2.838 $\times$ 10^6 J kg^{-1} at 0°C), u is the wind speed at reference height z, T_a and Q are the air temperature and specific humidity at reference height z, and T_0 and Q_0 are the temperature and specific humidity at the snow surface. C_H and C_Q are the bulk transfer coefficients for heat and water vapour respectively, which depend on atmospheric stability and surface roughness calculated by Monin–Obukhov surface layer similarity theory (Monin and Obukhov, 1954).

Remaining fluxes

The ground heat flux (GHF), is advected or conducted at the interface between the ground and the snow pack. The energy of snow pack phase changes (PCH) accounts for latent heat fluxes, e.g. melt-water refreezing in a snow pack. Heat advection by precipitation (PHF) results from the temperature of precipitating water (snow/rain) differing from the snow pack temperature. While the relative contribution of the different energy balance fluxes depends on prevailing meteorological and topographical conditions, PCH, GHF and PHF generally contribute on a minor level to the overall energy balance of the snow pack. PHF and PCH are mostly neglected in large-scale models.

2.2 Snow dynamics - forested areas

From Section 2.1 it is clear that snow pack dynamics consist of a myriad of often interlinked processes and are therefore difficult to simulate. Where snow packs are overlain by a forest canopy, the presence of trees exerts a principal control on these snow pack dynamics and further increases complexity (Musselman and Pomeroy, 2017, Roth and Nolin, 2017) by changing every part of the energy exchange between the land surface and the atmosphere. Figure 2.1 visualizes a partially snow-covered forest stand, with individual energy fluxes highlighted.

2.2.1 Mass balance - intercepted snow

From a mass balance perspective, intercepted snow in the canopy, which subsequently is unloaded, melted, redistributed or sublimated, can be the dominant component of the mass budget. During a snow-fall event in mid-winter, up to 60% can be stored as interception by the forest canopy, and throughout a winter period, 30-40% of it can be returned back to the atmosphere as water vapor via sublimation, as shown in a dry and cold climate

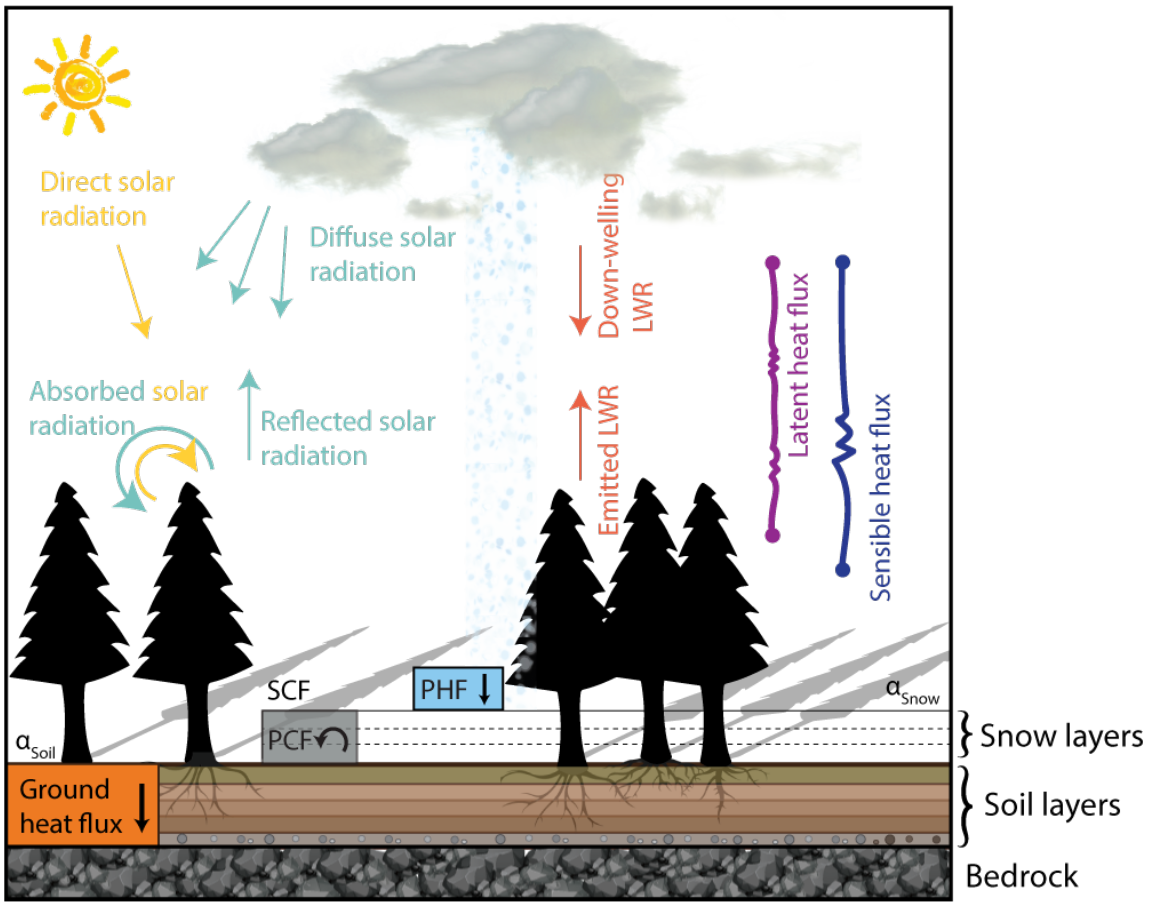

Figure 2.1: Schematic of forest-snow-atmosphere energy fluxes, adapted from Jonas and Essery (2011). The following abbreviations are used in the graphic: LWR is longwave radiation, SWR is shortwave radiation, PCF is the energy of snow pack phase changes, PHF is heat advection by precipitation, SCF is snow-covered fraction, α_{snow} is the snow albedo and α_{soil} is the albedo of the soil.

in Canada by Pomeroy and Schmidt (1993). Intercepted snow further affects the energy budget, as the presence of snow on the canopy alters the amount of solar radiation that is reflected by the land surface (Leonard and Eschner, 1968), which will be addressed in the subsequent sections.

2.2.2 Energy balance - surface radiation

Radiation exerts a primary control on the snow cover energy budget in forested environments (Sicart et al., 2004, Ellis et al., 2011); during springtime it can account for up to 92% of the energy available for snow-melt (Link and Marks, 1999). Consequently, accurate simulation of energy fluxes between the land surface and the atmosphere, with resulting melt-water runoff from snow-dominated forested watersheds, requires reliable estimates of radiative transfer processes through vegetation canopies (Lawler and Link, 2011, Seyednasrollah and Kumar, 2014). Compared to open areas, the presence of a forest

canopy attenuates shortwave radiation and enhances longwave radiation by absorption of shortwave radiation and re-emittance as longwave (e.g. Sicart et al., 2004), further affecting the timing, intensity, and duration of snow melt (Male and Granger, 1981). Forest structure and atmospheric conditions determine the relative importance of longwave and shortwave radiation (Pomeroy et al., 2009, Klos and Link, 2018). During periods of low solar irradiance, in combination with full snow cover and low atmospheric emissivity, canopy-induced attenuation of shortwave radiation is offset by longwave enhancement (Sicart et al., 2004, Webster et al., 2016*b*).

Longwave Radiation

The presence of trees often enhances longwave radiation reaching the sub-canopy snow surface. In dense forest stands, this longwave enhancement can be as high as 1.5 (Webster et al., 2016*b*, 2017). During spring-time, this has substantial impacts on melting, as on clear sky days net longwave radiation fluxes into the snow pack can exceed 40 W m^{-2} (Webster et al., 2016*b*). In order to account for this, downwelling longwave radiation needs to be split into two parts: downwelling longwave radiation from the atmosphere (LWR_{ac}) and incoming fluxes from the surrounding trees; the respective weights of each are determined by a factor describing the density of the forest canopy. The combined sub-canopy incoming longwave radiation at a point on the snow surface can be calculated by:

$$\downarrow LWR = VF_{Sky} LWR_{ac} + (1 - VF_{Sky}) \sigma \epsilon_c T_c^4 \tag{2.8}$$

where VF_{Sky} is the sky view fraction for the point of interest, which ranges from 0 to 1 where 0 means the sky is obscured completely (dense forest) and 1 means no trees are present. This parameter is interchangeable with other canopy density descriptors, e.g. Plant Area Index (PAI) and Canopy Coverage (CC), depending on which model is used. The emmisivity of the canopy (ϵ_c) is assumed to be 0.98 for forests (Essery, Pomeroy, Ellis and Link, 2008). The canopy temperature (T_c) is often assumed to equal air temperature above the canopy (Essery, Pomeroy, Ellis and Link, 2008).

However, especially during high insolation periods, canopy temperatures exceed air temperatures (Pomeroy et al., 2009), which can result in simulation errors of up to 40 W m^{-2} as demonstrated by Webster et al. (2016*b*) based on extensive field measurements in midlatitude coniferous forest stands. Webster et al. (2016*b*) mitigated this problem by incorporating a measured trunk view component and trunk temperature into Equation (2.8). Todt et al. (2018) further observed an overestimated range of longwave enhancement in the Community Land Model 4.5 (CLM4.5) and demonstrated improved model performance upon partitioning the vegetation canopy into two layers.

Shortwave Radiation

Net shortwave radiation of forested, snow-covered areas is more challenging to compute than net shortwave radiation of open snow-covered areas, particularly in discontinuous forest stands that consist of clearings and gaps (Baldocchi and Collineau, 1994). From an above-canopy perspective, the low albedo of trees can mask high sub-canopy snow albedo (Bonan, 2008), which decreases the overall reflectivity of the land surface (Betts and Ball, 1997). However, intercepted snow following snow-fall events can lead to temporary increases in LSA (Betts and Ball, 1997, Kuusinen et al., 2012). Below the forest canopy, the presence of forest litter has been found to substantially reduce forest floor snow albedo (Melloh et al., 2001). Wintertime LSA of forested environments also changes in response to tree species (Kuusinen et al., 2014), and varies in terms of forest structure (Bright et al., 2018) and seasonality (Kuusinen et al., 2012). Webster and Jonas (2018) further highlighted the importance of canopy structural shading of the snow surface for LSA during clear sky conditions by demonstrating shading-induced variations in LSA to be equally as important as interception-induced variations. All these factors collectively control LSA and net shortwave radiation of seasonally snow-covered forests, but uncertainty persists about how well they are represented by hydrological and land surface models.

As outgoing shortwave radiation is governed by reflection and scattering, sub-canopy radiation processes are vital for both forest floor snow dynamics and overall LSA. Trees strongly modify the transmission of solar radiation to the snow pack, which results in sub-canopy radiation fluxes that are highly variable in space and time, and controlled by the forest canopy architecture (Link et al., 2004, Malle et al., 2019). Transmissivity (τ) is the dimensionless ratio of radiation transmitted through a forest canopy to that incident above the canopy. Very dense forests prevent almost all incoming shortwave radiation from reaching the forest floor and hence have transmissivities approaching zero, while discontinuous forests can have transmissivities exceeding 50% (Reid and Essery, 2013).

τ is commonly estimated by an adaption of the Beer-Lambert's Law, which assumes an exponential reduction in SWR as it passes through the canopy (e.g. Nijssen and Lettenmaier, 1999, Hellström, 2000):

$$\tau = e^{-k \cdot LAI} \tag{2.9}$$

where k is an empirical extinction factor to account for orientation and clumping of canopy elements as well as for the direction of the incident solar radiation, and LAI is the leaf area index, which characterizes canopy density. LAI is also interchangeably referred to as Vegetation Area Index (VAI) or Plant Area Index (PAI) (Jonckheere et al., 2004), and

definitions vary, with the most universal being that LAI equals half of the total leaf area per unit ground surface area (Chen et al., 1997).

While there are many variations of the Beer-Lambert approach, it generally assumes the canopy to be an isotropic, homogeneous scattering medium with a random distribution of leaves and a spherical foliage angle distribution (Sicart et al., 2004). Directionality of direct incoming shortwave radiation is accounted for by some variation of

$$k_{dir} = \frac{1}{2cos(\theta)} \tag{2.10}$$

where θ is the solar zenith angle of the incoming solar beam. This approach allows sub-canopy radiation to be split into direct and diffuse components, where the direct component is modelled as a function of solar angle (via k_{dir}), while the diffuse component does not vary temporally and is proportional to VF_{Sky} (Link et al., 2004, Sicart et al., 2004).

More recently, Lawler and Link (2011) came up with a model that accounts for gaps exceeding the typical spacing between trees (e.g. the surrounding tree height). Other studies have also included various gap-fraction estimates (e.g. Seyednasrollah and Kumar, 2014), but such approaches still do not account for the 3-D structure of forest canopies, and hence do not replicate the temporal aspect of solar beam and canopy element interaction. Emerging errors due to this simplification are highest in late spring and heterogeneous forest stands (Musselman et al., 2013). More detailed approaches are also available, for example the geometric optical radiative transfer (GORT) model (Li et al., 1995), which includes multiple scattering within the canopy as well as between the canopy and the forest floor and further takes the exact 3-D geometry of the canopy into account. 3-D ray tracing models are emerging, (e.g. Musselman et al., 2013) but the computational efficiency is not yet sufficient to be used over large spatiotemporal extents. Kükenbrink et al. (2020), for example, recently came up with a 3-D radiative transfer model parameterization using Light detection and ranging (LiDAR) and spectroscopy data for tropical and temperate forest stands, and showed that the structure of a forest stand has a more pronounced impact on the light regime than leaf optical properties itself. Due to computational demands, however, their study sites were limited to two 60 x 60 m plots, further underlining that the the computational efficiency of such approaches is not yet sufficient to be used over large spatiotemporal extents.

2.3 Modelling forest-snow-atmosphere interactions with CLM5

The Community Land Model 5.0 (CLM5) is the land component of the Community Earth System Model (CESM v2.0) which was developed by the National Center for Atmospheric Research (NCAR). CLM5 is a state of the art, process-based land surface model that simulates carbon, nitrogen and energy exchange between the atmosphere and the terrestrial earth, a technical description of which is provided by Lawrence et al. (2018). CLM5 participates in multiple model intercomparision projects, for example the Land Surface, Snow and Soil Moisture Model Intercomparison Projects, e.g. LS3MIP (Van Den Hurk et al., 2016), which is part of the phase 6 Coupled Model Intercomparison Project (CMIP6). Furthermore, CLM5 also participates in the Earth System Model-Snow Model Intercomparison Project version 3 (ESM-SnowMIP3, Krinner et al., 2018, Menard et al., 2020), a modelling effort to evaluate current snow schemes against local and global observations in a wide variety of settings. As CLM5 is a well-documented and completely open-source community model, with advanced process representations of forest canopy and snow, which is widely used by the climate modeling community, it is an appropriate choice of model to address the research questions of this study.

2.3.1 Model structure

CLM5 by default is run over a global domain at different user-determined spatial resolutions (e.g. 0.25°, 0.5°, 1°, 2° grid-cells). Spatial land surface heterogeneity within each grid-cell is accounted for via a nested sub-grid hierarchy system which includes three levels: the land-unit level, the column level and the patch level (Figure 2.2). Each grid-cell can be split up into either one or several land-units (glacier, lake, urban, vegetated, crop whereby crop is only used if the crop model is active). Some physical state variables are already defined at this first sub-grid level (e.g. temperature, humidity).

In this study, the focus is solely on the vegetated land-unit, which has a single column assigned: the soil and snow column. This column consists of up to 20 soil layers, up to 5 bedrock layers and up to 10 snow layers. It is at this sub-grid level where variables like number of snow layers and soil roughness length are defined, and fluxes within the soil and snow are calculated, which provide a single set of upper boundary conditions. The third and final level of this hierarchy are patches, where plant functional types (PFT) are defined for vegetated land-units. Vegetation state variables (e.g. vegetation temperature, intercepted snow), which affect fluxes to and from the surface, are defined at this third sub-grid level (Oleson et al., 2010).

CLM5 differentiates between 16 possible PFT, all of which can coexist within one column. Figure 2.2 mentions 12 of those: bare ground, needle-leaf evergreen trees (temperate and boreal, NET), needle-leaf deciduous trees (boreal, NDT), broad-leaf evergreen trees (tropical and temperate, BET), broad-leaf deciduous trees (tropical, temperate and boreal, BDT), broad-leaf evergreen shrub (temperate, BLES) and broad-leaf deciduous shrub (temperate and boreal, BLDS). Omitted are 3 different kinds of grass (C_3 arctic grass, C_3 grass and C_4 grass) and un-managed, rain-fed crops.

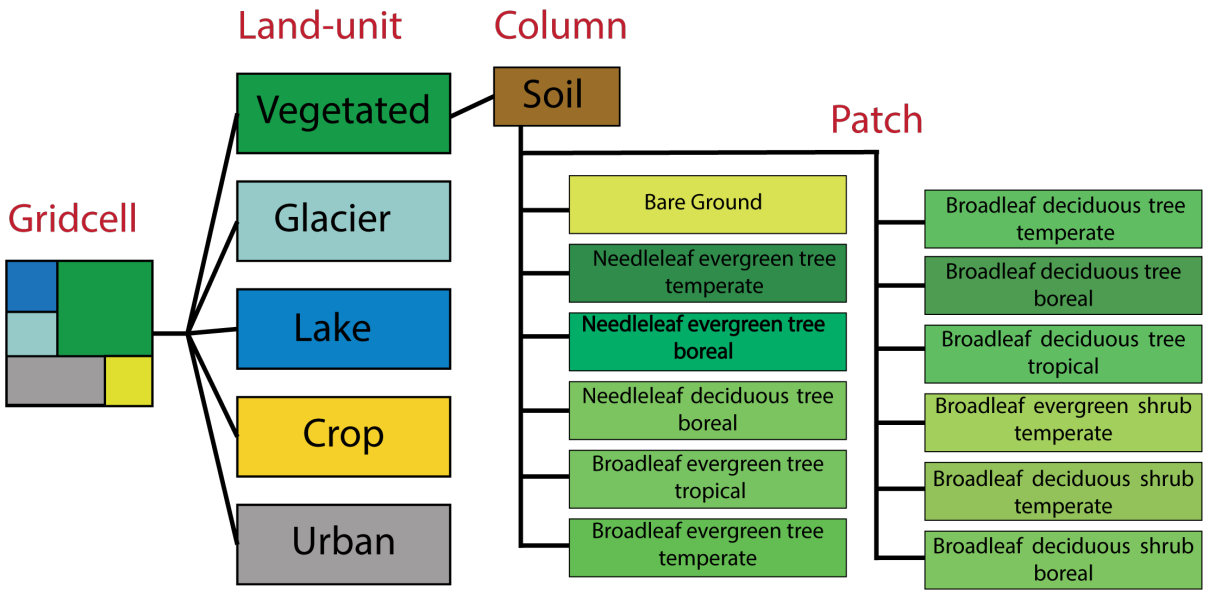

Figure 2.2: Configuration of the CLM5 subgrid hierarchy, with focus on vegetated areas.

Table 2.1: Percentage coverage and Plant Area Index across the Northern Hemisphere for PFTs of interest. Values are derived from the 0.25° surface dataset, as used by CLM5.

PFT	% coverage	Winter PAI
Needleleaf evergreen temperate	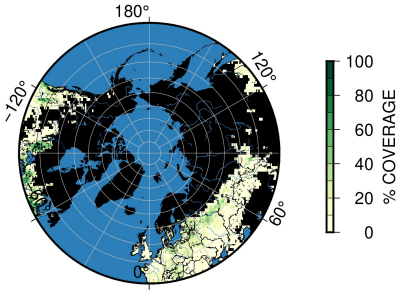	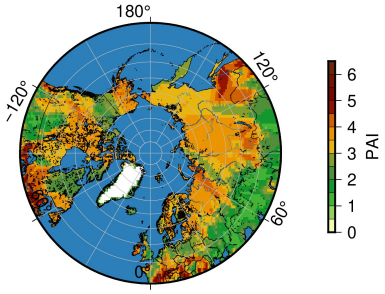
Needleleaf evergreen boreal	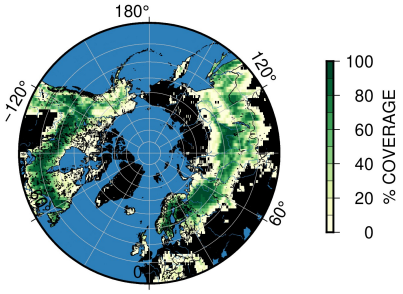	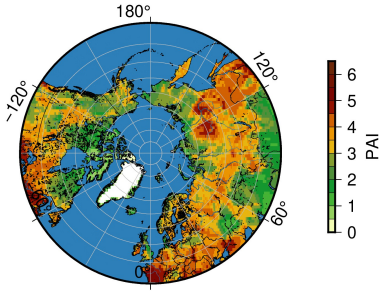
Needleleaf deciduous boreal	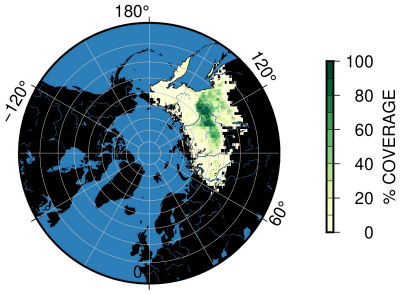	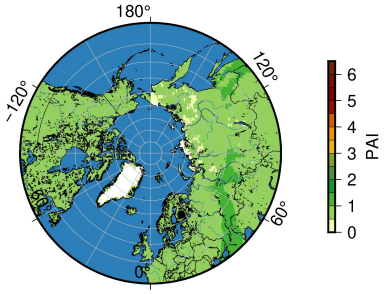
Broadleaf deciduous temperate	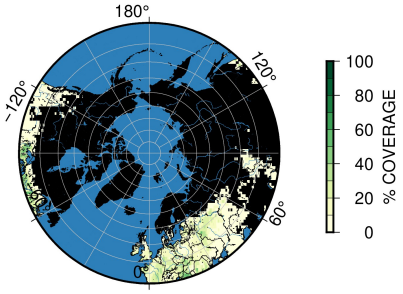	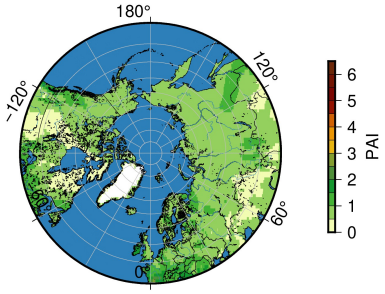
Broadleaf deciduous boreal	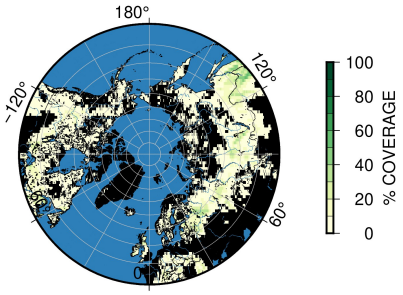	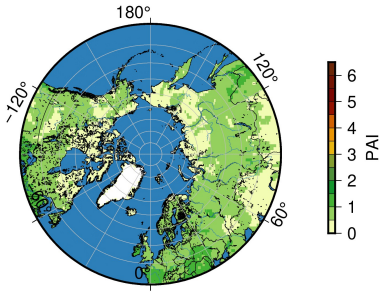

2.3.2 Canopy descriptors

Vegetation in CLM5 is conceptually represented by a homogeneous layer of leaves covering the land surface (also referred to as the big-leaf approach). Vegetation structure for each PFT is described by a monthly varying Leaf Area Index (LAI) and Stem Area Index (SAI), as well as canopy top and bottom heights. Percent PFT for each grid cell are derived from Moderate Resolution Imaging Spectroradiometer (MODIS) measurements (Lawrence and Chase, 2007), as are LAI and SAI values which vary by month. LAI and SAI are totaled to create a Plant Area Index (PAI). Table 2.1 shows percentage coverage of vegetated areas and corresponding winter-averaged (December-May) PAI values for the PFTs that overlap with snow-covered areas across the northern hemisphere. Magnitudes of percentage coverage of vegetated areas and PAI in Table 2.1 are based on a 0.25° global input surface dataset of CLM5. Note the large difference in PAI between needle-leaf and deciduous forest stands: While deciduous forests are rarely described by a PAI exceeding 2, the majority of needle-leaf forests have a PAI above 3. Canopy top and bottom heights are defined per PFT and do not vary across the globe or within a year (see Table 2.2 for PFTs in snow-covered regions).

Table 2.2: Canopy top and bottom heights for PFTs in snow-covered regions, as used by CLM5.

Plant functional Type	Canopy top height (m)	Canopy bottom height (m)
Needleleaf evergreen tree - boreal & temperate	17	8.5
Needleleaf deciduous tree - boreal	14	7
Broadleaf deciduous tree - boreal & temperate	20	11.5

2.3.3 The two-stream approximation

Shortwave radiative transfer through a single 'big leaf' layer is calculated using a two-stream approximation (Dickinson, 1983, Sellers, 1985), which provides a framework to calculate surface albedo and light absorption in the canopy while also accounting for multiple reflections by the leaves. Multi-directional scattering of photons is reduced to only two radiative fluxes, one upward and one downward. Implementation of the two-stream approximation in CLM5, described in detail by Bonan et al. (1996), consists of a coupled pair of inhomogeneous differential equations for the upward (Equation (2.11)) and downward (Equation (2.12)) radiative flux and is solved separately for the visible and near infra-red spectrum, as well as for incident direct and diffuse radiation. Ultimately, the two-stream approximation determines how forest canopies control reflection, absorption and transmission of solar energy.

When solving the two-stream approximation the following assumptions are made:

- Diffuse radiative fluxes are isotropic in upward and downward directions (Reality: as the angle between a leaf and a beam increases, the reflectivity decreases)
- Forest canopy is horizontally uniform.
- Leaves are treated as flat plates, no difference in bottom and top faces.
- Leaves are randomly arranged in space.

The vertical profile of the upward and downward diffuse radiative flux within the canopy is calculated as:

$$-\overline{\mu}\frac{dI\uparrow}{dP} + [1-(1-\beta)\omega]I\uparrow - \omega\beta I\downarrow = \omega\overline{\mu}K\beta_0 e^{-KL} \tag{2.11}$$

$$\overline{\mu}\frac{dI\downarrow}{dP} + [1-(1-\beta)\omega]I\downarrow - \omega\beta I\uparrow = \omega\overline{\mu}K(1-\beta_0)e^{-KL} \tag{2.12}$$

where $I\uparrow$ and $I\downarrow$ are the upward and downward diffuse radiative fluxes, P is the combined exposed leaf and stem area index (Plant Area Index, PAI), K is the optical depth of the direct solar beam per unit plant area, and $\overline{\mu}$ is the average inverse diffuse optical depth per unit plant area. For optical properties: β and β_0 are upscatter parameters for diffuse and direct radiation respectively, and ω is the scattering coefficient.

Equation (2.11), which describes the vertical profile of the upward diffuse radiative flux within the canopy comprises a term ($-\overline{\mu}\frac{dI\uparrow}{dP}$) which describes the attenuation of the upward diffuse flux, a term ($[1-(1-\beta)\omega]I\uparrow$) which computes the fraction that is rescattered in an upward direction following interaction with leaf elements and a term ($\omega\beta I\downarrow$) which calculates the fraction of the downward diffuse flux converted into an upward diffuse flux by back-scattering. These three terms are counter-balanced by a final term ($\omega\mu K\beta_0 e^{-KL}$), which describes the contribution of the upward diffuse flux by scattering of direct incident flux. Similar descriptions apply to Equation (2.12).

At time-steps with no snow present in the canopy, the optical parameters ω, β and β_0 are calculated based on weighted leaf and stem transmittance and reflectance, which for each PFT and wavelength are defined by Dorman and Sellers (1989) and Asner et al. (1998). In contrast to previous versions of CLM, CLM5.0 explicitly accounts for snow in the canopy via a revised snow interception scheme, which introduces separate storage terms of liquid and solid phases of water. The amount of intercepted snow in the canopy is calculated explicitly, from which a canopy intercepted snow fraction ($frac_{interc}$) can be obtained. $frac_{interc}$ is then used to adjust the overall optical reflectance parameters ω and β at time-steps where canopy snow is present:

$$\omega = (1-frac_{interc})\omega_{leaf} + (frac_{interc})\omega_{snow} \tag{2.13}$$

$$\beta = (1 - frac_{interc})\beta_{leaf} + (frac_{interc})\beta_{snow} \tag{2.14}$$

The optical properties ω_{snow} and β_{snow} are defined in Table 2.3, which are from Sellers et al. (1986).

Table 2.3: Intercepted snow optical properties

Parameter	visible	NIR
ω_{snow}	0.8	0.4
β_{snow}	0.5	0.5

2.3.4 Snow and soil albedo

In order to calculate resulting LSA using the two stream approximation, ground albedo parametrization is required. Depending on the snow cover fraction ($fsno$), the ground albedo (α_{gr}) is a weighted combination of soil and snow albedo (α_{soil} and α_{snow}):

$$\alpha_{gr} = \alpha_{soil}(1 - fsno) + \alpha_{snow} fsno \tag{2.15}$$

where α_{gr} is calculated separately for direct and diffuse radiation. This is only relevant for α_{snow}, as in CLM5 α_{soil} is identical for direct and diffuse radiation and only a function of the soil colour class and water content of the surface soil layer.

SNow ICe and Aerosol Radiation model (SNICAR)

Snow albedo in CLM5 is calculated via the SNow ICe and Aerosol Radiation model (SNICAR), which uses the two-stream radiative transfer solution of Toon et al. (1989). Albedo of the underlying substrate is a boundary condition for radiative transfer simulations of SNICAR. SNICAR considers the composition of snow (ice, carbon, dust) as well as snow ageing using separate fractions for old snow, refrozen liquid and fresh snow. Snow albedo and a snow pack vertical light absorption profile are calculated, both of which are dependent on: (a) solar zenith angle, (b) albedo of the substrate underlying the snow, (c) mass concentrations of aerosols, and (d) the snow effective grain size. SNICAR computes albedo and a vertical absorption profile for 5 spectral bands (1 visible, 4 near infra red). For the visible spectra only, SNICAR applies the Delta Eddington Approximation (Joseph and Wiscombe, 1976) to account for the strong forward scattering in snow. For each snow layer (up to 5, depending on snow depth), the following bulk optical properties have to be calculated: extinction optical depth (τ), single scatter albedo(ω) and scattering asymmetry parameter (g). Flanner and Zender (2005) gives an in-depth description of SNICAR and its implementation in CLM5.

Chapter 3

Observational field data collection

In this chapter, methods used for observational field data collection are introduced alongside data quality control measures and a detailed description of all field sites. Firstly, the custom-made cable car system, used for below canopy measurements is described (RQ1a and RQ2b). Then, the uncrewed aerial vehicle (UAV) system, used for measurements of LSA is presented (RQ1b and RQ2a). Methods used to collect meteorological reference data, necessary to provide boundary conditions on measurement days (RQ1a-b) and to generate CLM5 forcing data (RQ2a-b), are discussed. In the second part of this chapter, all field sites located in a) alpine and sub-alpine and b) boreal forest environments are described in detail.

3.1 Field methods

3.1.1 Cable car system

The cable car system, as pictured in Figure 3.1, included a 8mm steel cable tightened between two trees with a manual wire rope hoist (HABEGGER, load capacity 8kN) and a custom-made cable car, which served as a moving net-radiometer. The height of the cable varied between 1 and 3m, depending on local surface topography and snow height. The horizontal profile of the transect was maintained using a distometer (Leica Disto X310) with an accuracy of ± 1cm. The cable car included up- and down-looking short- and longwave radiation sensors (Kipp and Zonen CMP3 pyranometers and CGR3 pyrgeometers) as well as a down-looking Sony Alpha NEX6 16.1MP camera with a Yasuhara Madoka f/4 7.3mm 180° fisheye lens. Furthermore, an inclinometer (Kelag KAS901-51A) recorded the tilt of the system in x- and y direction to an accuracy of 0.01°. The cable car moved at a constant speed of 0.07m/s, while the radiation sensors, connected to a Campell Scientific CR1000 data-logger, measured at 1 second intervals. Movement was controlled by a motor

(Micro motors E192.12.67) and powered by a 5200mAh Li-Ion battery. Switches on each end of the cable car allowed for automatic reversal in direction upon reaching either end of the cable.

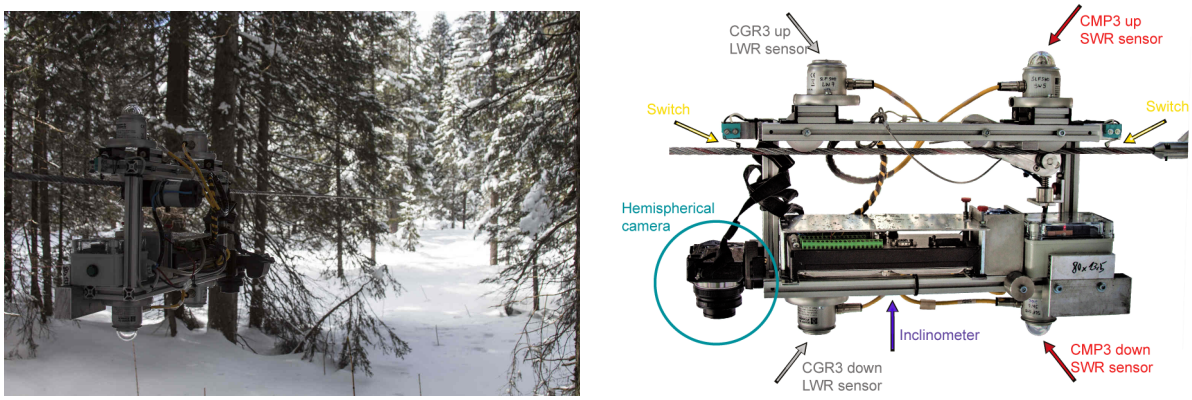

(a) **(b)**

Figure 3.1: (a) Cable car system attached to steel cable and in action at the transect in Davos Laret (CH). (b) Cable car system with up- and down-looking shortwave and longwave sensors, as well as the hemispherical camera, inclinometer and switches highlighted.

3.1.2 Uncrewed aerial vehicle (UAV) system

Above-canopy albedo was measured using a DJI S1000 spreading wings octocopter UAV, which was equipped with up- and down-looking Kipp and Zonen CMP3 shortwave radiation sensors (Figure 3.2). The radiation sensors, connected to a Campell Scientific CR300 data logger, measured at one second intervals. The UAV featured retractable legs, which assured no occlusion of the field of view of the down-looking radiation sensor.

The UAV was controlled by a WooKong-M autopilot system, and on-board navigation using integrated Global Navigation Satellite Systems (GNSS) was assured using an Inertial Measurement Unit (IMU), barometer and compass components. The UAV was powered by a 16000 mAh battery, which allowed flight times up to 15 minutes. Flight data including longitude, latitude, altitude, velocity, acceleration, pitch, roll and yaw were recorded with a DJI iOSD Mark II. A 2.4GHz data-link enabled constant connectivity between the UAV and a ground station unit. This enabled high accuracy positioning and stabilization of the UAV in winds up to 28 km/h.

A Bluetooth connection was used to enable communication between the ground station and a tablet computer, which was used to program and navigate flights using the DJI iPad Ground Station app (v. 1.4.63). While the take-off and landing of each flight was controlled manually, the flight plan was autonomous, allowing consistency in the repeat-ability and comparability between flights. A different flight plan was programmed for each field site,

all of which are shown in Section 3.2. Each flight plan covered between 8 and 13 waypoints (WPs) along total flight lines of between 160 and 250m in length. UAV flying height was 15-20m above canopy. The UAV was set to hover at each WP for 15 seconds to account for the response time of the radiation sensors. Both vertical and horizontal speeds were set to 1m/s.

Radiation data for each WP was only used if at least 6 seconds of data were within a 3m buffer in x, y and z directions around a defined WP coordinate. In addition, a filter was applied to omit any data exceeding a sensor tilt threshold of 5° or more, as suggested by Bogren et al. (2016). On clear sky days, if the standard deviation of incoming shortwave radiation throughout a flight was below 10 W m^{-2} and the difference between minimum and maximum was below 30 W m^{-2}, the mean of all measured incoming shortwave radiation data was used for LSA calculation at each WP. This further minimized the effect of directional tilt error due to the position and orientation of the up-looking UAV radiation sensor relative to the sun.

A down-looking Sony Alpha NEX6 16.1MP camera with a Yasuhara Madoka f/4 7.3mm 180° fish-eye lens was attached to the UAV. The Sony Alpha NEX6 was operated using a the Sony Time-lapse app (v. 3.40) with automatic triggering at 1 second intervals. Each down-looking hemispherical photograph captured the 180° view-field of the adjacent down-looking pyranometer.

Figure 3.2: UAV system. (a) DJI S1000 drone in action: Legs are retracted, flight data is recorded and LSA measurements are taken. (b) UAV system, with up and down-looking CMP3 shortwave radiation sensors, CR300 datalogger and Sony NEX6 camera highlighted.

3.1.3 Meteorological reference data

Meteorological reference data served two purposes in this study: firstly, it provided a continuous set of atmospheric boundary conditions for every measurement day which allowed

identification of clear-sky vs. cloudy meteorological conditions. Secondly, meteorological driving data for CLM5 model experiments was required to simulate LSA. Meteorological variables needed to drive CLM5 simulations include temperature (T_{air}), relative humidity (RH), wind speed (U_a), incident longwave radiation (LWR), incident shortwave radiation (SWR), precipitation (P) and pressure (see Table 3.1). Meteorological data were measured at 1-hour temporal resolution using automatic weather stations (AWS) in unforested, open locations within 1 km of each forest site.

The majority of data was collected at two locations: a sub-alpine environment in Davos Laret, Switzerland and an arctic boreal environment in Sodankylä, Finland. Meteorological reference data for Davos Laret was obtained from an AWS operated by MeteoSwiss (DAV2 station, 46.812969N 9.843558E 1594m.a.s.l.), while for Sodankylä, data were measured by an AWS operated by the Finnish Meteorological Institute (FMI-ARC station, 67.367N 26.629E 179m.a.s.l.). Table 3.1 summarizes the sensors at each of the AWS. At Davos Laret, meteorological data were collected in winter 2017/18 (Figure 3.3) and at Sodankylä meteorological data were collected in winter 2018/19 (Figure 3.4), both of which were used as reference data for UAV and cable car measurements, and as forcing data for all CLM5 simulations.

Table 3.1: Measured meteorological variables and sensors at Davos Laret (DAV2 station) and Sodankylä (FMI-ARC station).

Variable	**Sensor DAV2**	**Sensor FMI-ARC**
Temperature [K]	meteolabor ag VTP37	Rotronic PT100
Relative Humidity [%]	meteolabor ag VTP37	Vaisala HMP
Wind speed [m s^{-1}]	Lambrecht L14512	Vaisala WAA25
Longwave radiation [W m^{-2}]	Kipp&Zonen CG4	Kipp&Zonen CG4
Shortwave radiation [W m^{-2}]	Kipp&Zonen CM21	Kipp&Zonen CM11
Precipitation [mm s^{-1}]	Lambrecht 1518 H3	Ott Messtechnik Pluvio2
Pressure [Pa]	Vaisala PTB330	Vaisala PTB201A

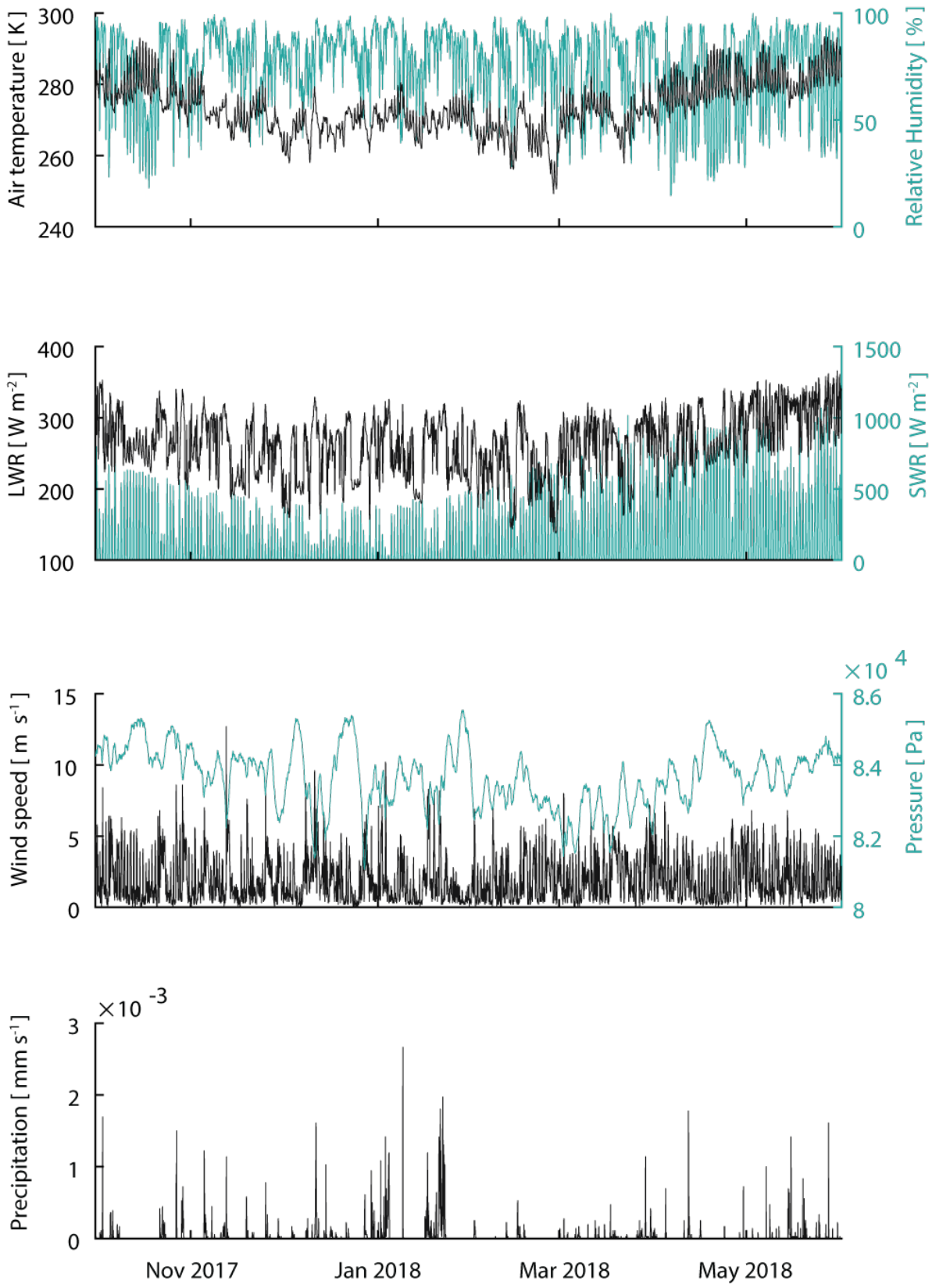

Figure 3.3: Meteorological reference data at Davos Laret, Switzerland. Data (air temperature, relative humidity, longwave radiation, shortwave radiation, wind speed, pressure and precipitation) measured at the DAV2 station.

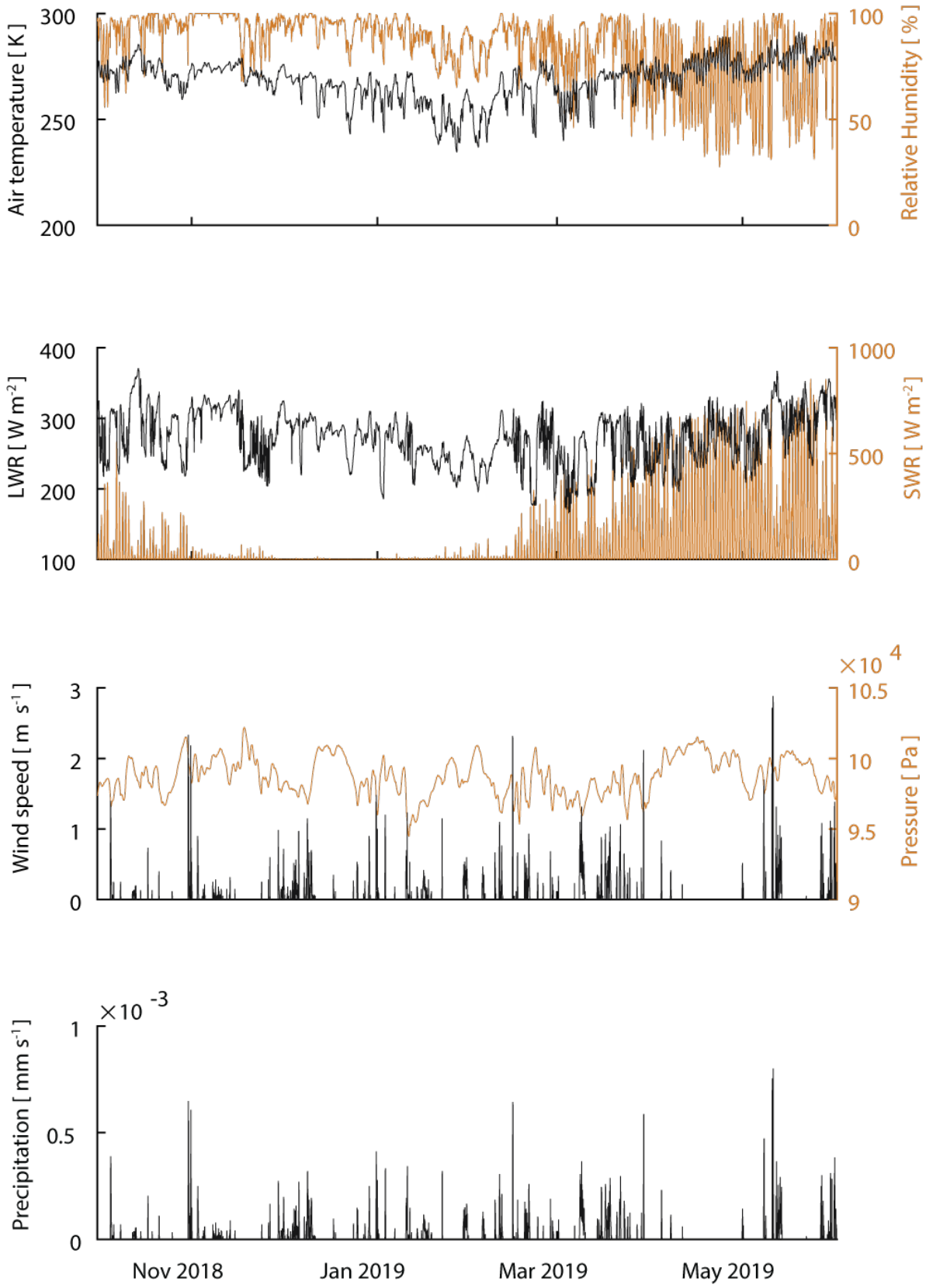

Figure 3.4: Meteorological reference data at Sodankylä, Finland. Data (air temperature, relative humidity, longwave radiation, shortwave radiation, wind speed, pressure and precipitation) measured at the FMI-ARC station.

3.1.4 Sensor calibration

The cable car and the UAV systems used identical sensors to measure shortwave radiation (Kipp and Zonen CMP3, class II instruments), while the cable car additionally used two longwave radiation sensors (Kipp and Zonen CGR3, class II instruments). Relative comparison between sensor performance is especially important when calculating albedo (ratio of outgoing and incoming shortwave radiation). Hence, several calibration campaigns were performed (e.g. Figure 3.5) during a wide range of meteorological conditions and for many solar angles. Calibration analysis showed a maximum difference of 3.8 W m^{-2} between the longwave CGR3 measurements and of 45 W m^{-2} between the shortwave CMP3 measurements. As the largest variation in SWR measurements was noted during the middle of the day, a solar angle dependent correction was applied to the down-looking SWR sensors mounted onto the UAV. Variation in the longwave instruments was within measurement uncertainty, hence no correction was applied. Details of the sensor calibrations and resulting correction can be found in Appendix A.

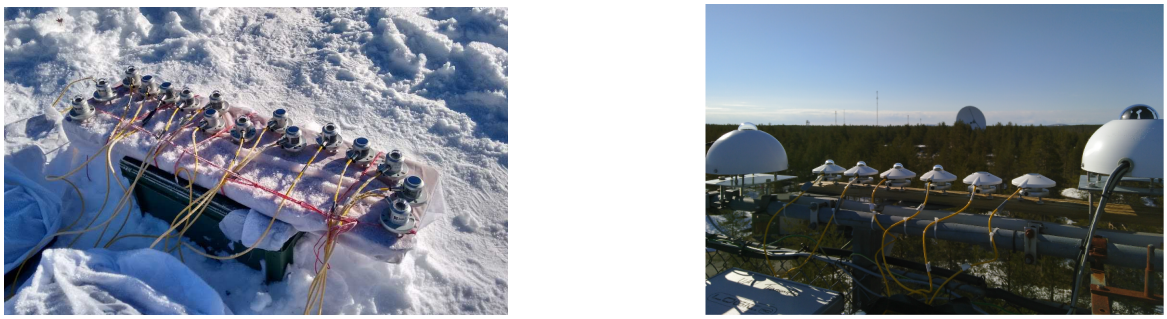

(a) **(b)**

Figure 3.5: Sensor calibration setup in (a) Davos (CH) and (b) Sodankylä (FIN).

3.2 Field sites

Data were collected at 6 field sites in two climatically different environments. Two sites were in boreal forest environment in Sodankylä, Finland, and four sites (Davos Laret, Maienfeld, Flin, Ofenpass) in sub-alpine and alpine forest environments in Switzerland (Figure 3.6). Climatically different behaviour of the Swiss and the Finnish sites is largely due to their latitudinal difference (46° vs 67°N), which strongly affects incoming shortwave radiation, e.g. very low incoming shortwave radiation between December and February in Sodankylä (Figure 3.4) and different incoming shortwave radiation and corresponding zenith angles for the same day (clear sky conditions) at both locations, as shown in Figure 3.7. While the minimum solar zenith angle at Davos Laret is 37°, the zenith in Sodankylä is never less 57°; and the maximum amount of incoming shortwave radiation

differs by 200 W m^{-2}. In addition to capturing climatic variability, locations of field sites were selected to cover a range of tree species with varying canopy structures and canopy densities. UAV measurements were made in Sodankylä during a targeted campaign in the spring of 2019 (16/04/2019 - 10/05/2019). UAV and cable car measurements were made in Switzerland throughout the 2017/18 winter season and on two specific measurement days (16.01.2019 & 12.03.2019) during the 2018/19 winter season. Site characteristics of all sub-alpine, alpine and boreal sites are summarized in Table 3.2.

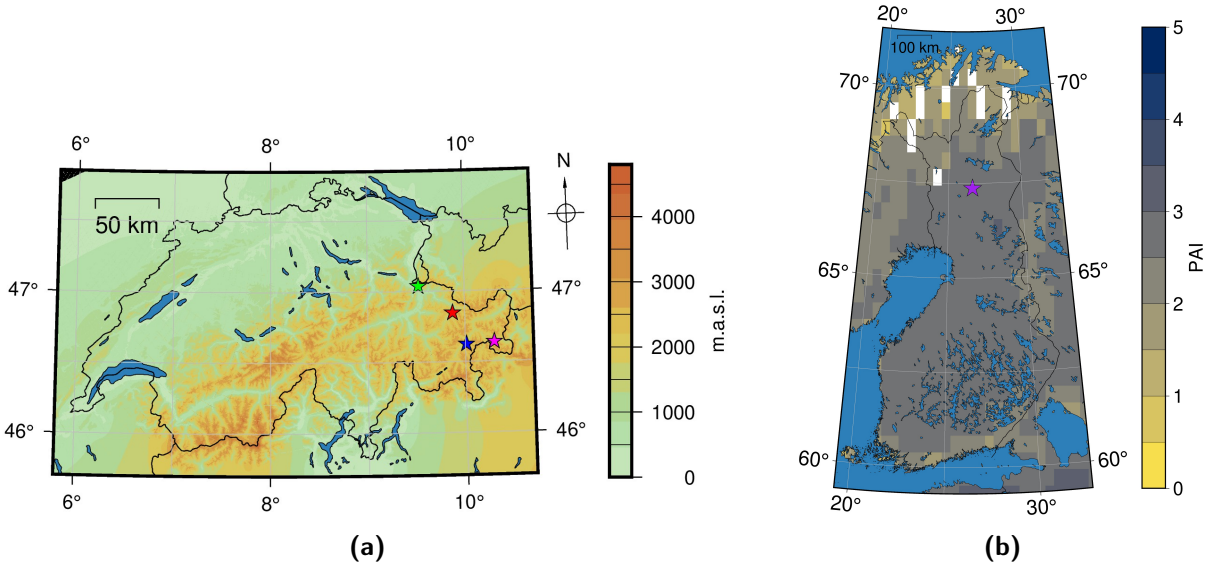

Figure 3.6: (a) Location of all field sites in Switzerland (green=Maienfeld, red=Laret, blue=Flin, pink=Ofenpass). Background reflects elevation based on a swiss-wide Digital Elevation Model. (b) Location of field sites in Sodankylä, FIN. Note that the two sites (pine, birch) were in close proximity, hence their locations overlap. Background reflects PAI magnitudes as obtained from the MODIS-based 1° CLM5 input surface dataset.

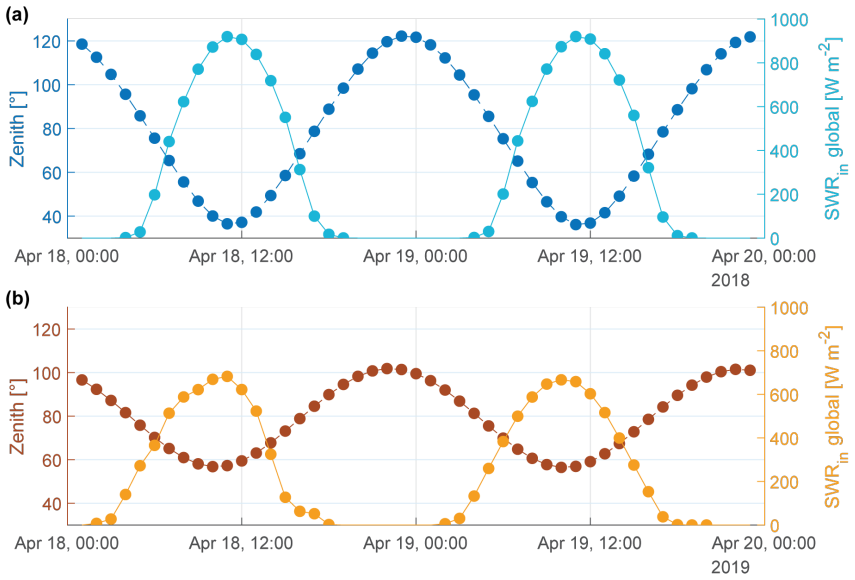

Figure 3.7: Incoming SWR and zenith angles for a) Davos Laret and b) Sodankylä.

Table 3.2: Summary of field sites locations and data collection periods for all sites in this study. Location, tree species, periods of data collection, number of UAV flights and cable car runs (CC-runs) performed at each site, as well as zenith and azimuth angle ranges are presented. Note that the same colours as in Figure 3.6 are used to denote sites.

Location **Tree species**		**Latitude** **Longitude** **Elevation**	**Data collection**	**# Flights** **# CC-runs**
Davos Laret (CH) Norway Spruce		46°50'40"N 9°52'29"E 1530m	01/2017-05/2018 03/2019	48 96
Maienfeld (CH) Beech		47°01'06"N 9°32'02"E 634m	06/02/2019	4 -
Flin (CH) Larch		46°37'24"N 10°00'36"E 1655m	14/02/2019 15/02/2019	5 -
Ofenpass (CH) Pine		46°38'17"N 10°17'44"E 2076m	27/02/2019	4 -
Sodankylä (FIN) Birch	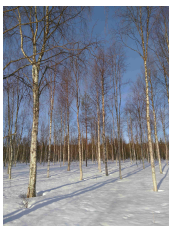	67°21'56"N 26°37'20"E 178m	04-05/2019	16 -
Sodankylä (FIN) Pine		67°21'53"N 26°38'10"E 179m	04-05/2019	19 -

3.2.1 Switzerland: Sub-alpine and alpine forests

Davos Laret - Spruce Forest

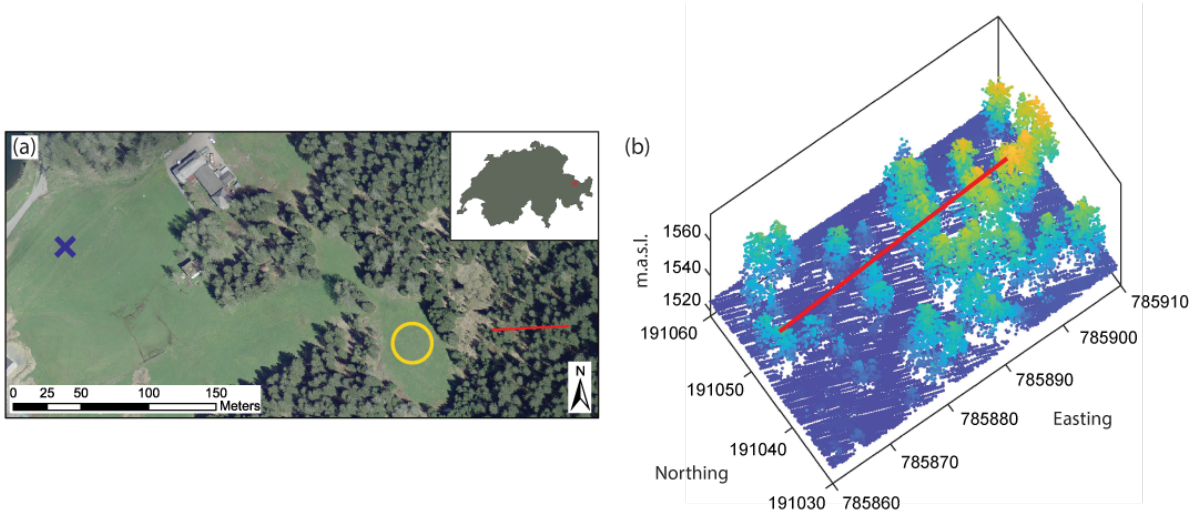

Figure 3.8: (a) Layout of the Davos Laret (CH) field site, where the red line indicates the cable car transect, the blue cross shows the reference meteorological station and the yellow circle locates the UAV start and landing area. (b) A 3-D LiDAR plot visualizing the forest stand surrounding the cable car transect.

Davos Laret served as an intensive observation area throughout this study. It is located in the very east of Switzerland, at a discontinuous forest area (46°50'40"N, 9°52'29"E, 1530 m.a.s.l) and was chosen due to suitability for UAV operations, e.g. Webster et al. (2018), and its heterogeneous forest cover which includes larger forest openings. Detailed LiDAR data (36 points/m^2) were available for Davos Laret, which were acquired in September 2010 using a helicopter-mounted Riegl LMS Q560 sensor, e.g. Moeser et al. (2014, 2015). A digital terrain model (DTM) and a digital surface model (DSM) were computed from LiDAR data, providing a detailed canopy height model (CHM) which enabled calculation of canopy descriptors. Canopy descriptors of interest for this study were canopy coverage (CC), defined as the ratio of area covered by the vertical projection of the canopy relative to ground area (Mazzotti et al., 2019), mean tree height (MTH) and maximum tree height (MaTH). The CHM was binarized based on a 2-m threshold and circular areas of 10m radii were used to compute CC, MTH and MaTH around each waypoint location.

The forest stand in Davos Laret predominately consists of Norwegian spruce (*Picea abies*), with tree heights varying from 10-40m. During 2017/18, measurements were conducted in Davos Laret on 22 days between 10 January and 15 June 2018. Meteorological conditions ranged from clear sky to 8/8 cumulus cover, interception load from no interception to full interception, and ground snow cover from full snow cover to no snow. During the 2018/19 winter, Davos Laret was revisited twice (16.01.2019 and 12.03.2019).

Figure 3.8(a) visualizes the layout of the Davos Laret site, including the location of the cable car transect, the location of an open site meteorological reference station, and the UAV take-off and landing area. Figure 3.8(b) shows the forest stand surrounding the 48m long cable car transect at Davos Laret, which was installed along the West-East axis, reaching from discontinuous to dense sections of the forest canopy. Figure 3.9a visualizes a transect through a 3-D point cloud, enhanced with stems and branches following Webster et al. (2020), along the UAV flight path. UAV flight paths went directly above the cable car transect (Figure 3.9b), which shows a CHM of the flight area with waypoint locations being indicated by red crosses. Details of the flight plan (9 WPs) are summarized in Table 3.3, which gives location, flight height and the lidar-derived canopy descriptors CC, MTH and MaTH for each waypoint location where the UAV hovered for 15seconds.

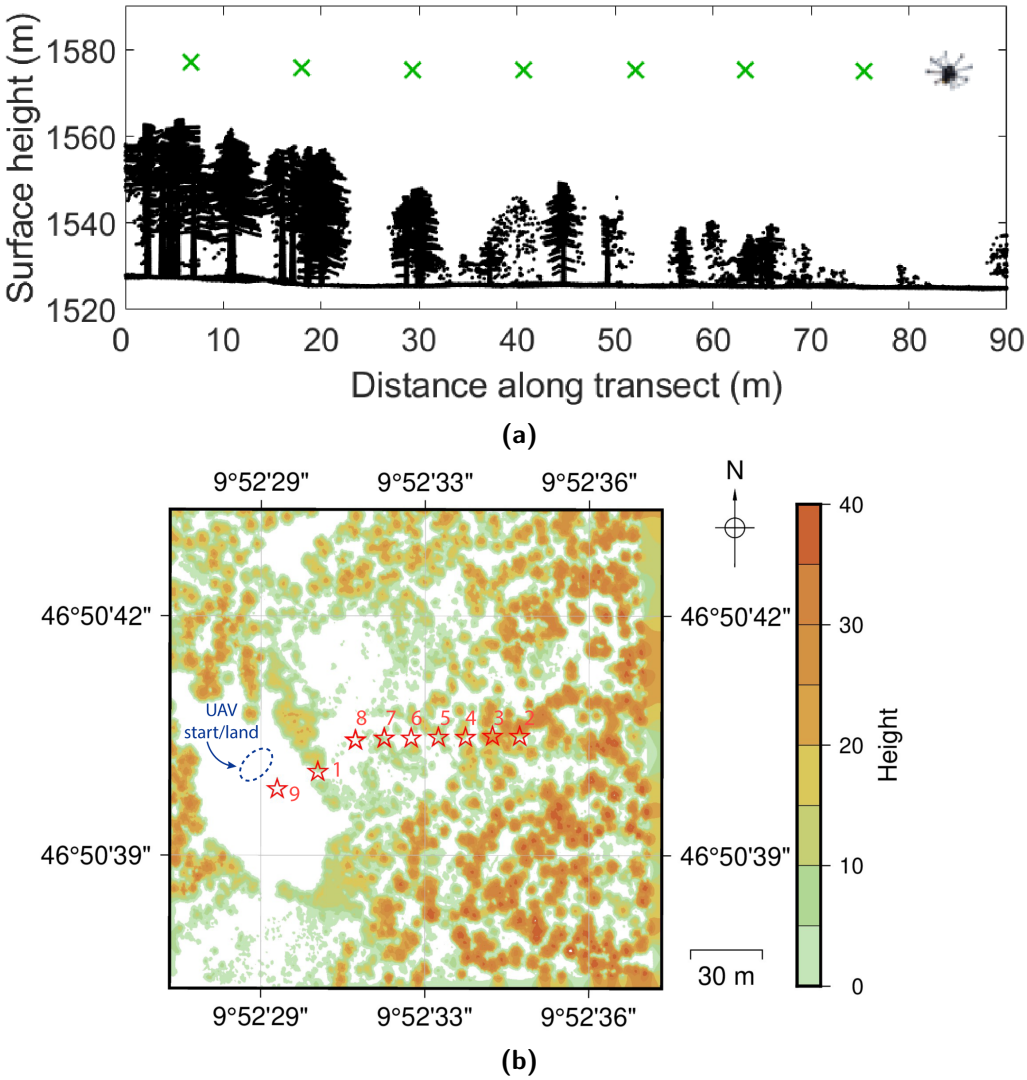

Figure 3.9: UAV-related field setup: (a) Transect through a 3-D LiDAR point cloud, which was enhanced with branches and stems (following Webster et al., 2020). Waypoints of the flight plan for Davos Laret are indicated by green crosses. (b) Canopy height map for Davos Laret with waypoint locations indicated by red stars.

Table 3.3: Davos Laret (CH): Flight plan details. Summary of location (long/lat/alt), flight height, and lidar-derived canopy characteristics for each waypoint.

WP #	Longitude	Latitude	Alt. [m.a.s.l]	Flight ht. [m]	CC_{10}	MTH_{10} [m]	$MaTH_{10}$ [m]
1	9.875112	46.844414	1525.17	50	0.33	5.37	17.73
2	9.876219	46.844547	1527.11	50	0.89	20.41	34.91
3	9.876070	46.844547	1525.78	50	0.80	16.20	30.65
4	9.875922	46.844543	1525.33	50	0.39	9.55	21.47
5	9.875773	46.844543	1525.43	50	0.40	7.68	21.86
6	9.875624	46.844540	1525.27	50	0.12	6.86	20.25
7	9.875476	46.844540	1525.24	50	0.30	4.60	13.04
8	9.875318	46.844532	1525.09	50	0.03	2.18	3.97
9	9.874889	46.844349	1527.32	50	0.00	0.00	0.00

Flin - Larch Forest

The field site at Flin (46°37'24"N 10°00'36"E, 1655m.a.s.l) is located in the upper Engadin Valley and consists of a discontinuous larch forest (*Larix decidua*), which transitions into a mixed forest (larch/spruce) towards the west of the site. Flight plan details are given in Table 3.4 and are visualized in Figure 3.10. High density airborne laser scanning data (5-30 points/m^2) were obtained in 2017 from an airplane-mounted Riegl Q-1560 at around 4000m.a.s.l. A CHM and canopy descriptors were generated from these LiDAR data. UAV measurements in Flin were made on 14 and 15 February 2019 during clear sky conditions and full ground snow cover. Six flights were performed during the second half of the both days, capturing a solar zenith range between 59° at solar noon and 85° just before sunset.

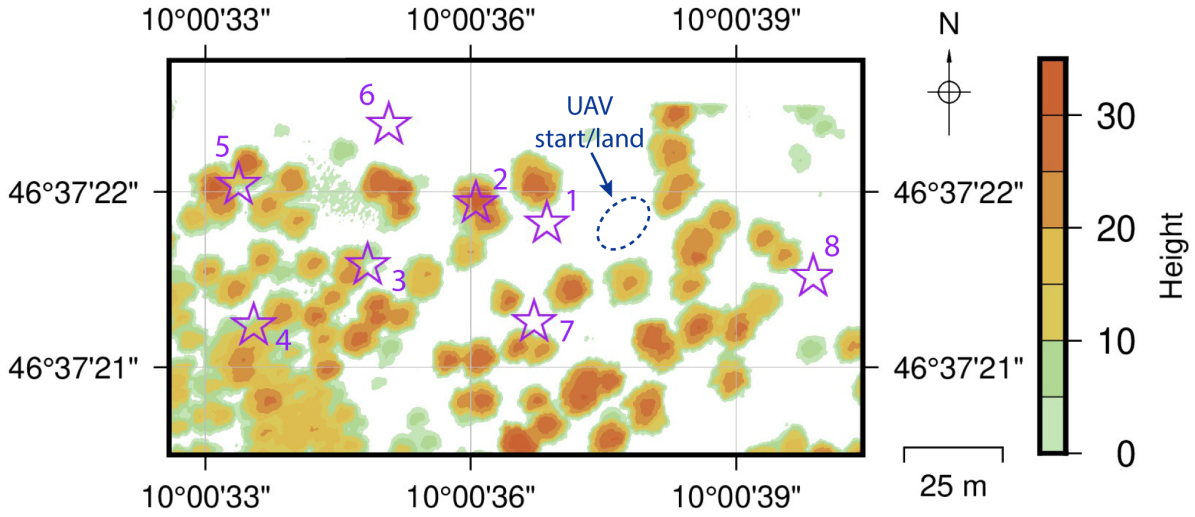

Figure 3.10: UAV WPs (purple stars) from Flin (CH) flight plan.

Table 3.4: Flin (CH), larch site: Flight plan details. Location, flight height, canopy characteristics.

WP #	Longitude	Latitude	Alt. [m.a.s.l]	Flight ht. [m]	CC_{10}	MTH_{10} [m]
1	10.010210	46.622303	1657.8	60	0.09	14.37
2	10.010017	46.622574	1657.8	60	0.61	20.07
3	10.009658	46.622433	1657.8	60	0.71	18.51
4	10.009280	46.622295	1657.8	60	0.49	12.46
5	10.009230	46.622616	1657.8	60	0.93	14.87
6	10.009728	46.622753	1657.8	60	0.61	8.15
7	10.010252	46.622528	1657.8	60	0.35	17.99
8	10.011135	46.622406	1657.8	60	0.07	6.10

Maienfeld - Beech Forest

Maienfeld (47°01'06"N 9°32'02"E, 634m.a.s.l.) served as a representative site for a deciduous forest, with the predominant species being beech (genus *Fagus*). Across Switzerland, deciduous forests are located at lower elevations and the seasonal window of opportunity to capture full ground snow cover is short. UAV measurements at the Maienfeld site were made on 6 February 2019, during clear sky conditions. Snow cover was full at part of the site and fractional elsewhere. The flight plan included ten WPs, with locations and flight height shown in Table 3.5. No detailed airborne LiDAR data was available for the Maienfeld site, so downlooking hemispherical images from UAV flights were used to calculate a "ground view fraction" (VF_{Ground}) parameter to describe canopy density, where a high ground view fraction means sparse forest environment. Section 4.1.2 expands on this concept. Five flights were performed, capturing solar zenith angles between 63 and 85° and azimuth angles between 182 and 235°.

Table 3.5: Maienfeld, beech site: Flight Plan details. Location, flight height, canopy characteristics and ground view fraction.

WP #	Longitude	Latitude	Alt. [m.a.s.l]	Flight ht. [m]	VF_{Ground}
1	9.533801	47.017403	628.5	35	0.37
2	9.533801	47.017399	628.5	50	0.47
3	9.533364	47.018040	628.5	50	0.58
4	9.533125	47.018116	628.5	50	0.65
5	9.532886	47.018208	628.5	50	0.72
6	9.532702	47.018280	628.5	50	0.69
7	9.532306	47.018436	628.5	50	0.63
8	9.532697	47.018074	628.5	50	0.73
9	9.533254	47.017780	628.5	50	0.53
10	9.533801	47.017658	628.5	50	0.48

Ofenpass - Pine Forest

The Ofenpass site (46°38'17"N 10°17'44"E 2076m.a.s.l.) is located in the very east of Switzerland and consists of an alpine pine forest environment (*Pinus pinea* and *Pinus cembra*). UAV measurements were conducted on 27 February 2019, during clear sky and full snow cover conditions. Five flights were performed in the second half of the day, each flight consisting of ten WPs at a flight height of 40m (Table 3.6). Similar to Maienfeld, no detailed LiDAR map was available for the Ofenpass site, hence VF_{Ground} from down-looking hemispherical photographs is used to describe forest density.

Table 3.6: Ofenpass, pine site: Flight Plan details. Location, flight height and ground view fraction.

WP #	Longitude	Latitude	Alt. [m.a.s.l]	Flight ht. [m]	VF_{Ground}
1	10.296439	46.638298	2072.9	40	0.33
2	10.296103	46.638508	2075.8	40	0.39
3	10.295723	46.638458	2075.9	40	0.59
4	10.295310	46.638397	2078.4	40	0.73
5	10.294989	46.638149	2077.1	40	0.62
6	10.294883	46.637917	2076.7	40	0.63
7	10.295179	46.637699	2073.9	40	0.62
8	10.295633	46.637676	2074.3	40	0.65
9	10.296101	46.637871	2074.1	40	0.57
10	10.296515	46.638065	2073.0	40	0.37

3.2.2 Sodankylä, Finland: Boreal Forests

Sodankylä is located within boreal forest in central Lapland (67°22' N, 26°39' E). A research station, operated by the Finish Meteorological Insitute (FMI), served as base station during a targeted field campaign in the spring of 2019 (18/04 - 10/05/2019) and provided infrastructure and meteorological reference data. Terrestrial LiDAR data enabled CHM generation and calculation of canopy descriptors (CC_{10}, MTH_{10}). The same methodology as used for airborne LiDAR data (see Section 3.2.1) was applied, with CHM binarization based on a 2-m threshold and circular areas of 10m radii around each waypoint location for CC and MTH computations.

During the field campaign, ground snow cover conditions ranged from full snow cover to almost complete melt out and meteorological conditions ranged from clear sky days to 8/8 cumulus. Two regular measurement sites were established at Sodankylä: one in a pine forest (*Pinus sylvestris*, Figure 3.11) and one in a birch forest stand (genus *Betula*, Figure 3.12).

Pine Site

The pine site consisted of a discontinuous forest stand. The programmed flight plan (Figure 3.11 and Table 3.7) included thirteen WPs capturing a large range of canopy densities (CC_{10} range: 0.02 - 0.84). MTH ranged from 3.3 to 7 meters. UAV measurements were performed on 26 April (full snow cover), 4 May 2019 and 9 May 2019 (fractional snow cover), which yielded an extensive LSA dataset.

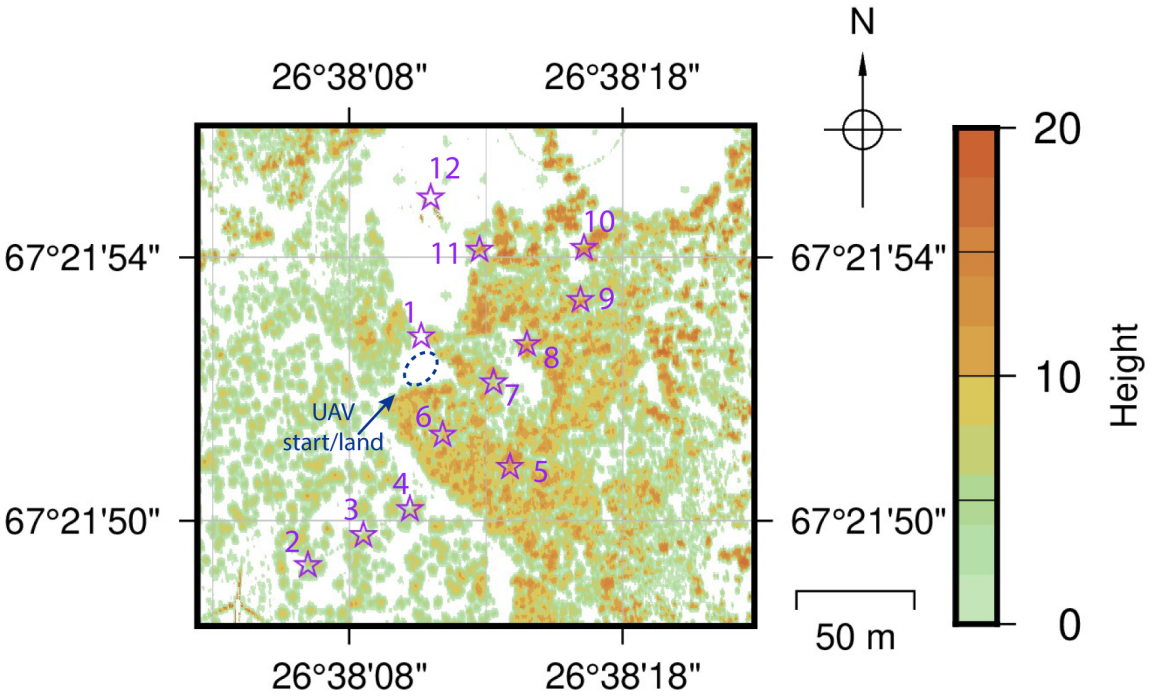

Figure 3.11: UAV WPs from pine flight plan.

Table 3.7: Sodankylä, pine site: Flight plan details. Location, flight height and canopy characteristics.

WP #	Longitude	Latitude	Alt. [m.a.s.l]	Flight ht. [m]	CC_{10}	MTH_{10} [m]
1	26.636211	67.364700	203.0	35	0.29	4.40
2	26.635092	67.363831	203.0	35	0.30	3.37
3	26.635639	67.363945	203.0	35	0.44	3.47
4	26.636099	67.364044	203.0	35	0.37	3.82
5	26.637087	67.364204	203.0	35	0.84	5.94
6	26.636421	67.364326	203.0	35	0.72	5.53
7	26.636925	67.364525	203.0	35	0.54	4.88
8	26.637255	67.36467	203.0	35	0.52	6.22
9	26.637783	67.364838	203.0	35	0.67	5.16
10	26.637817	67.365036	203.0	35	0.41	7.00
11	26.636787	67.365028	203.0	35	0.50	6.04
12	26.636303	67.365227	203.0	35	0.02	-
13	26.636324	67.364693	203.0	35	0.30	4.68

Birch Site

The birch site was located 500m to the west of the pine site, on the western side of the river Kitinen. For the first part of the campaign (- 25 April 2019), the UAV take-off and landing area was in the middle of the frozen river, which changed to an open clearing upon seasonal river ice break up (Figure 3.12). Measurements were taken on 5 different days (19 April, 29 April, 5 May, 10 May 2019), capturing ground conditions ranging from full snow cover to almost complete melt out (Table 3.8).

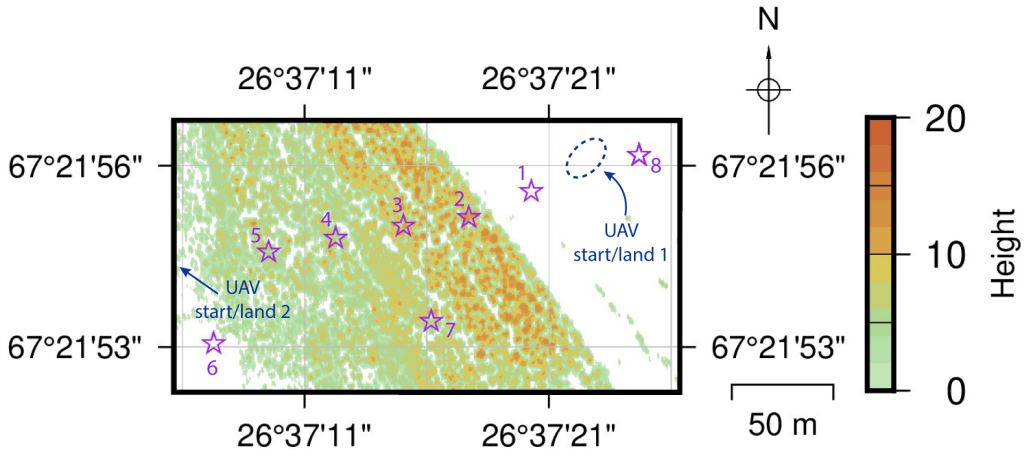

Figure 3.12: UAV WPs from birch flight plan.

Table 3.8: Sodankylä, birch Site: Flight Plan 1 details. Location, flight height and canopy characteristics.

WP #	Longitude	Latitude	Alt. [m.a.s.l]	Flight ht. [m]	CC_{10}	MTH_{10} [m]
1	26.622198	67.365486	206.0	35	0	0
2	26.621481	67.365372	206.0	35	0.70	7.34
3	26.620731	67.365334	206.0	35	0.77	7.42
4	26.619955	67.365280	206.0	35	0.53	4.80
5	26.619186	67.365219	206.0	35	0.60	4.33
6	26.618557	67.364815	206.0	35	-	-
7	26.621050	67.364914	206.0	50	0.58	6.39
8	26.623432	67.365646	206.0	80	0	0

Chapter 4

Impacts of shading and fractional snow cover on the sub-canopy radiation budget

The presence of trees has major effects on the snow cover energy budget, which is strongly controlled by radiation (Link and Marks, 1999, Sicart et al., 2004, Ellis et al., 2011). In this chapter, the focus lies upon the sub-canopy radiation budget, as RQ1a is addressed:

What are the driving factors that control the sub-canopy radiation budget in a seasonally snow-covered forest environment?

Answering this research question requires spatially and temporally distributed measurements of sub-canopy radiation in seasonally snow-covered forest stands. In lieu of fine-scale satellite remote sensing products capable of capturing sub-canopy radiative regimes at high spatial and temporal scales, in-situ radiation measurements are still indispensable when aiming to improve process-scale understanding of radiative transfer through a canopy. However, the use of a single stationary radiometer is not adequate to represent the heterogeneity of a forest stand (Link et al., 2004); previous studies have therefore used radiometer arrays of various extents (Pomeroy et al., 2009, Seyednasrollah and Kumar, 2014, Webster et al., 2016*a*), which are associated with high costs, and are not capable of capturing outgoing radiation. Moving rail systems have been used as an alternative approach to capture spatiotemporal radiation patterns below a forest stand over lengths ranging from 10 to 60 m to investigate the effects of foliage clumping (Law et al., 2001), seasonal trends of diurnal energy balance in boreal aspen forests (Blanken et al., 2001) as well as transpiration dynamics (Vrugt et al., 2002). Such a moving rail system has also been deployed in a snow-dominated environment (Stähli et al., 2009, Webster et al., 2016*b*), but the rail system only covered a relatively small distance (10 m) in a fairly dense forest. However, moving rail systems have the potential to capture radiative transfer processes

in snow- dominated, forested environments, providing high spatiotemporal sub-canopy radiation data.

Here, a novel dataset of distributed sub-canopy radiation measurements in a discontinuous evergreen needle-leaf forest stand in the Swiss Alps is presented (the "Davos Laret" site, Section 3.2.1), collected by the cable car system introduced in Section 3.1.1. This moving net radiometer was used to measure incoming and outgoing shortwave and longwave radiation, alongside a camera to quantify the hemispherical view fractions of shaded snow, sunlit snow, bare ground (all down-looking), as well as sky and canopy (up-looking). Analysis focuses on both diurnal and seasonal radiation patterns below an evergreen forest stand with four main objectives, which each quantify (1) the influence of shading on both outgoing shortwave radiation as well as sub-canopy effective albedo, (2) the effect of solar angle and forest structure on the sub-canopy radiation budget, (3) the effect of fractional snow cover on outgoing longwave radiation, and (4) the relative importance of shortwave and longwave radiation on the sub-canopy all-wave radiation budget.

This chapter has been published as "*Shading by Trees and Fractional Snow Cover Control the Subcanopy Radiation Budget*" in Journal of Geophysical Research: Atmospheres (Malle et al., 2019).

4.1 Methods

4.1.1 Meteorological conditions

Figure 4.1a and 4.1b show above canopy meteorological conditions from the open site reference station and the 17 different days between January and May 2018 when transect runs of radiation measurements were made using the cable car system. On two selected clear-sky days (red arrows in Figure 4.1a), one at the start (18.4.2018) and one in the middle (25.4.2018) of melt season, continuous radiation measurements were performed throughout the entire day from before sunrise to after sunset. Both days had very similar meteorological conditions (see Figure 4.1c-d), with the main difference being a reduction in snow cover extent. Measurements collected during these two clear-sky days were used to analyze diurnal radiation patterns of incoming, outgoing, and net shortwave as well as longwave radiation, while the data from all campaigns are used to investigate seasonal trends.

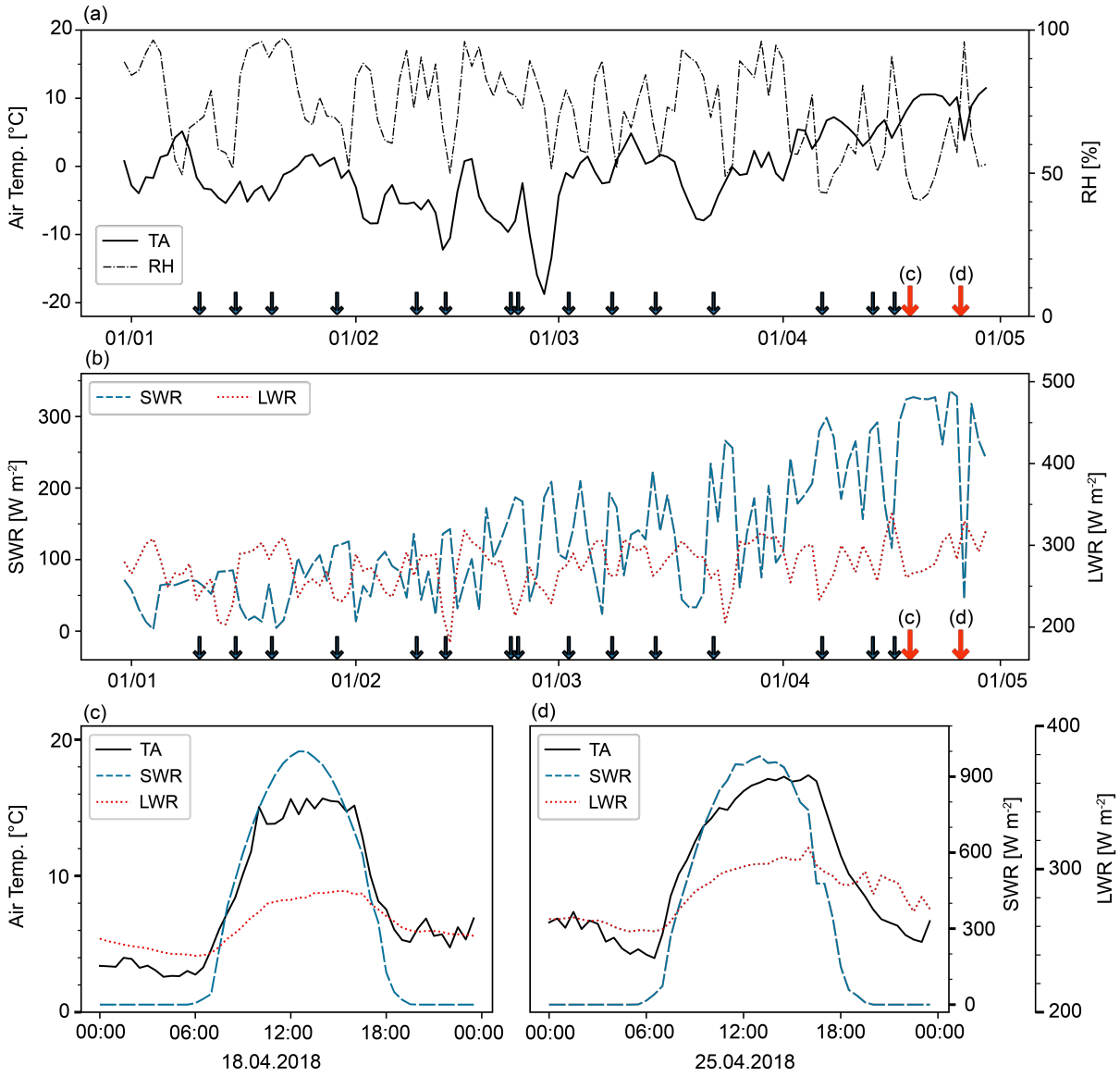

Figure 4.1: Meteorological conditions at the reference open site in Davos (CH). Daily averages from January until May 2018 are shown for (a) air temperature and relative humidity as well as for (b) incoming shortwave (SWR) and longwave radiation (LWR). Arrows at the bottom indicate days when cable car measurements were performed. Larger red arrows indicate the two days of continuous radiation measurements (18.4.2018, 25.4.2018) for which the meteorological conditions are visualized in (c) and (d).

4.1.2 Calculation of Hemispherical View-Fractions

Ground View Fractions

Ground surface conditions were obtained by analyzing down-looking hemispherical photographs. The down-looking Sony NEX6 camera (Figure 3.1) was set to trigger every 5 seconds (Sony Time-lapse App, V3.40), resulting in 110-120 images along each 48 m transit. Of those images, 42 were selected that were best collocated with the respective spatial

aggregation units of the radiation measurement. Each selected down-looking hemispherical photograph was analyzed to obtain the following hemispherical view fractions: ground view fraction (VF_{Ground}), sunlit-snow view fraction (VF_{Sun}) and shaded-snow view fraction (VF_{Shade}). VF_{Ground} refers to all snow-free surfaces, including both bare ground and canopy elements, whereas VF_{Sun} and VF_{Shade} separate snow-covered surfaces into sun-lit and shaded areas. To arrive at the different view fractions, a two stage manual thresholding was used: 1) pixels were classified into either snow (white) or ground/stems (black) to determine VF_{Ground}, 2) pixels classified as snow in stage 1 were further separated into sunlit-snow (white pixel) from shaded snow (black pixel) to determine VF_{Sun}. VF_{Shade} was then calculated as a residual using:

$$VF_{Shade} = 1 - VF_{Ground} - VF_{Sun} \tag{4.1}$$

Solar radiation of shaded areas predominantly consists of the diffuse component, further enhancing the presence of blue light, whereas bare ground and canopy elements mostly consist of red and green light. While all three RGB bands were used to select a threshold to distinguish between sun-lit and shaded snow pixels, only the blue band was used when categorizing each pixel into snow or ground. By only using the blue band, contrast between snow and bare ground/stems is improved, and cast shadows of surrounding trees are ignored (Wolter et al., 2012, Webster and Jonas, 2018). This approach has been suggested by previous studies for separation of canopy and sky pixels in traditional up-looking hemispherical photographs (Leblanc et al., 2005, Nobis and Hunziker, 2005, Zhang et al., 2005, Reid and Essery, 2013). Once the threshold was selected, each hemispherical image was discretized into 10 concentric analysis rings, and the ratio between black and white pixels within each analysis ring was calculated and further weighted by the sine of the elevation angle to determine VF_{Ground}, VF_{Sun} and VF_{Shade}, following the approach applied by Essery, Bunting, Rowlands, Rutter, Hardy, Melloh, Link, Marks and Pomeroy (2008) on upward-looking hemispherical images. When the snow cover fraction is 100%, VF_{Ground} reflects the fraction of trunks in the 180° view field of a hemispherical photograph, which gives the baseline reference for snow cover extent calculations. VF_{Ground} was only calculated once per day to account for melt-out of snow, while VF_{Sun} and VF_{Shade} had to be determined for each transit due to the changing solar angles. Figure 4.2 shows an example down-looking hemispherical photograph as well as the resulting categorized image indicating the extents of VF_{Ground}, VF_{Sun} and VF_{Shade}.

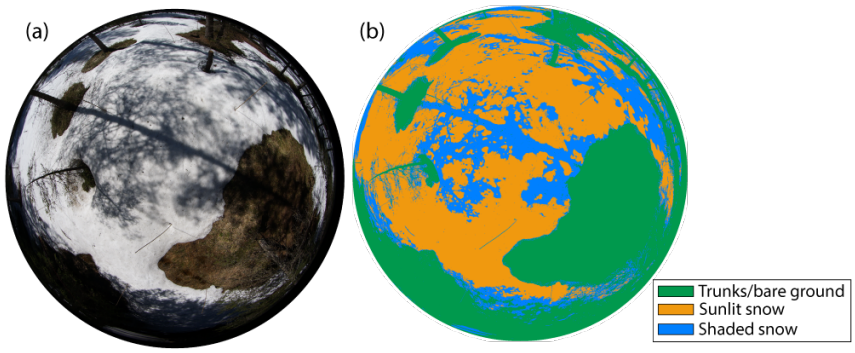

Figure 4.2: (a) Exemplary down-looking hemispherical photograph used to investigate ground conditions. (b) Analysed image, distinguishing between bare ground/stems (green), sunlit snow (orange) and shaded snow (blue).

Sky View Fractions

For each of the field sites, the Sony Alpha NEX6 camera was attached at the top of the cable car system in order to obtain Sky View Fraction (VF_{Sky}) to quantify forest density along the observed transect. This was either done during an overcast day with uniform light conditions, or before/after sunset. The images were analyzed using the same methods as for VF_{Ground}, VF_{Sun} and VF_{Shade}. As an example, Figure 4.3 shows the resulting VF_{Sky} along the transect for the Davos Laret field site, which was constant throughout the winter season. VF_{Sky} ranged from 0.10 at the dense, east end of the transect to 0.46 at the west end where the forest cover was discontinuous. Figure 4.3 further indicates how VF_{Ground} ranged from 0.01 to 0.32 during full snow cover conditions on 18 April – indicating the baseline trunk view fraction along the transect – and how it was increased to ranging from 0.16 to 0.93 on 25 April due to partial melt-out.

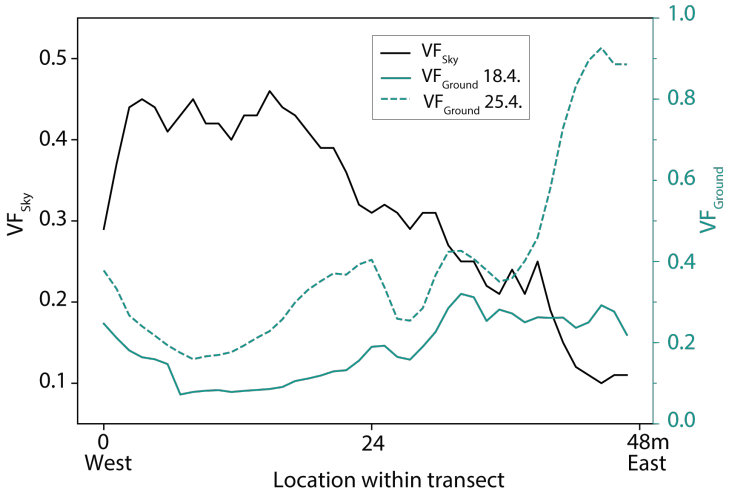

Figure 4.3: Cross sectional view of the cable car transect indicating Sky View Fraction (VF_{Sky}) and Ground View Fraction (VF_{Ground}) along the 48m transect in Davos Laret.

4.2 Results

4.2.1 Diurnal analysis

Shortwave radiation

Figure 4.4 contrasts the diurnal patterns of 18 April and 25 April 2018 of shortwave radiation fluxes and sunlit-snow view fraction. Meteorological conditions were almost identical between the two days (see Figure 4.1c-d), forest structure was constant and the solar declination angle was only changing minimally, therefore the incoming SWR patterns between 18 and 25 April were nearly the same (see Figure 4.4a-b). High spatial and temporal data resolution allowed detailed measurement of small changes in meteorological conditions (e.g. cirrus cloud moving through in the afternoon of 25 April) as well as interactions between forest structure and the changing daytime solar position. For instance, sections with high/low insolation moved over the day to the East, as the sun moved to the West, leading to diagonal patterns visible in all panels of Figure 4.4.

Outgoing sub-canopy SWR (Figure 4.4c-d) was influenced by patterns of incoming SWR, but fine-scale imprints of the forest structure were not present in the data due to a higher fraction of diffuse radiation in reflected SWR. The maximum outgoing SWR on 18 April was 403 W m^{-2}, which was lower by 24 % at 305 W m^{-2} on 25 April. Differences in outgoing SWR between the two observed days were coincident with both an increase in VF_{Ground} (smaller fractional snow cover, shallower snow pack, more trunks visible) and a decrease in the albedo of the remaining snow surface (snow age, litter). Some differences were notable at the eastern end of the transect, where most of the melt out had happened. Patterns of VF_{Sun} (Figure 4.4e-f) resembled the outgoing SWR patterns for both days, with high sunlit-snow-view fractions occurring at locations with high outgoing SWR, while locations where outgoing SWR was low were mostly shaded. Similarities between diurnal patterns of outgoing SWR and VF_{Sun} demonstrated the strong control shading had on sub-canopy radiation. This is further illustrated by Figure 4.5, which contrasts outgoing SWR and VF_{Sun} for all data points collected during full snow cover conditions (18 April 2018), further implying a strong positive relationship (correlation coefficient R=0.94) between outgoing SWR and VF_{Sun}. Figure 4.5 also shows how during low zenith angles, which occurred around local solar noon, a large variability was observed in both outgoing SWR and VF_{Sun}. During low zenith angles, the western part of the transect where canopy closure was sparse showed high values in VF_{Sun}, while the east part was too dense for sun rays to penetrate through the canopy and therefore corresponded to low VF_{Sun}. During high zenith angles, shadows were predominant throughout the entire transect, resulting in a smaller range in both outgoing SWR as well as VF_{Sun}. Effective albedo patterns are shown in Figure 4.4g-h. Measured effective albedo > 1 occurred predominantly at

transitions from continuous ($VF_{Sky} < 0.2$) to discontinuous forest, where trees sheltered the up-looking pyranometer from incoming SWR while the snow surface below was still sun-lit. At these locations, effective albedo values of up to 2 were measured on 18 April and up to 1.5 on 25 April. Contrasting effective albedo values of 18 and 25 April further shows the substantially lower effective albedo on 25 April at the eastern end of the transect where most of the snow had already melted.

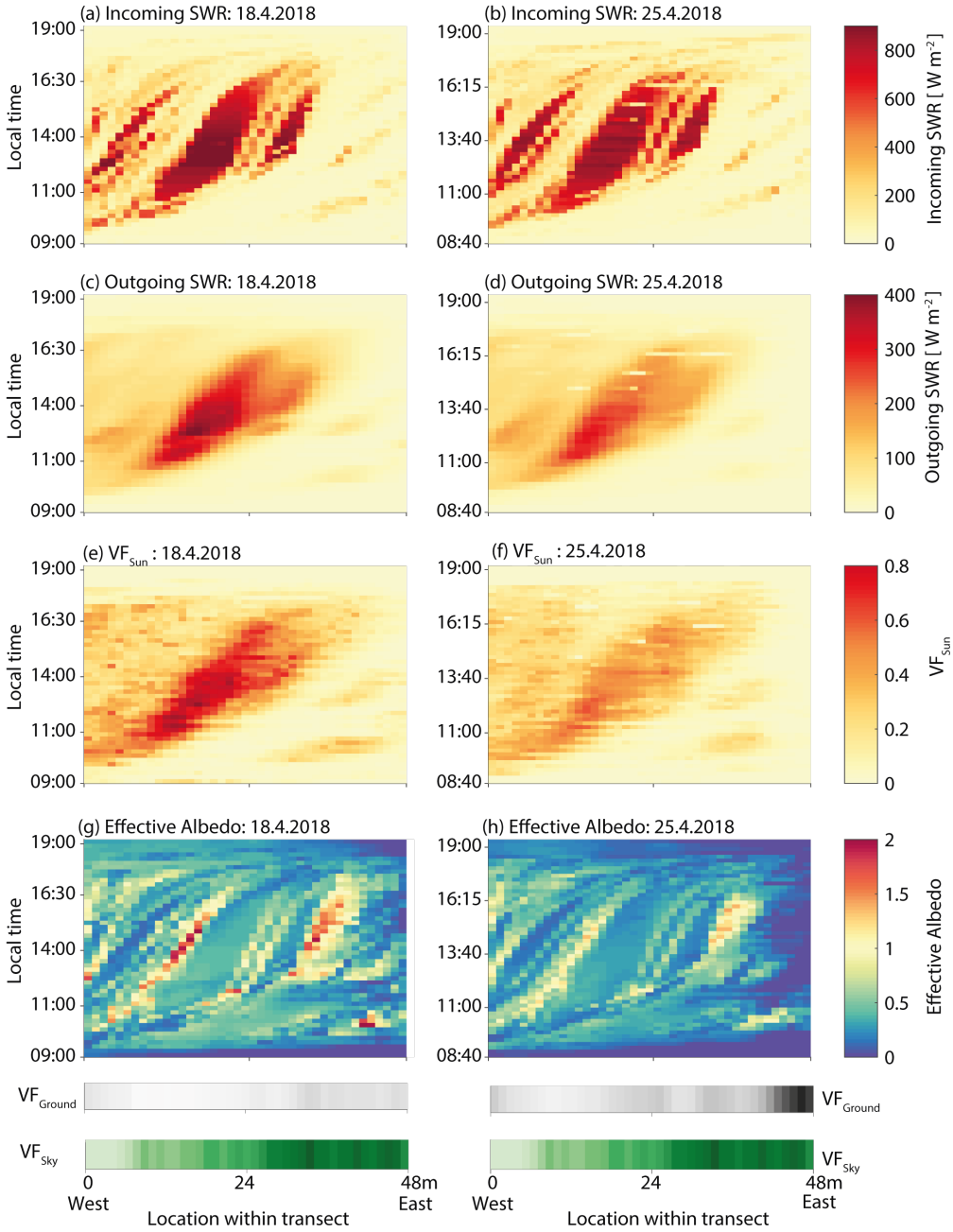

Figure 4.4: Shortwave radiation patterns for 18 April (full snow cover) and 25 April 2018 (partial snow cover). (a-b) visualize incoming SWR, (c-d) outgoing SWR, (e-f) VF_{Sun} and (g-h) effective albedo for the respective days. The colour bars below show VF_{Ground} (white = 0, black = 1) and VF_{Sky} (white = 1, dark green = 0) along the transect for each day. VF_{Ground} and VF_{Sky} are quantified in Figure 4.3.

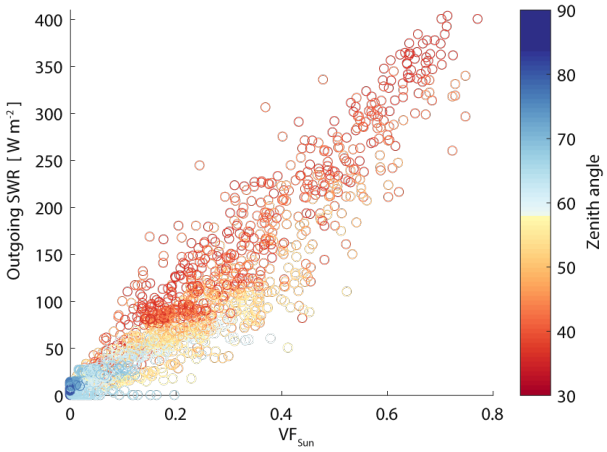

Figure 4.5: Sunlit-snow view fraction vs. outgoing shortwave radiation during a sunny day with full snow cover conditions (18 April 2018). Each data point represents a single measurement along the transits on 18 April 2018.

Longwave radiation

Figure 4.6 illustrates longwave radiation along the transect for 18 April and 25 April, respectively. In contrast to SWR-related data shown in Figure 4.4, spatiotemporal patterns of LWR include vertical as well as diagonal features, the former being related to stationary effects such as LWR irradiance from snow-free ground or canopy elements, the latter reflecting temporary heating from absorption of direct SWR. On both days sub-canopy incoming LWR was particularly high at locations with low VF_{Sky} (Figure 4.6a-b). Increases in below canopy incoming longwave radiation were especially pronounced in the afternoons, once diurnal increases in above canopy shortwave radiation had heated the forest canopy, which due to internal heat storage of the canopy, remained effective until after sunset. On 25 April, emittance of LWR from the canopy was especially enhanced due to warmer mid-day air temperatures (see Figure 4.1c and d), leading to incoming longwave radiation of up to 403 W m^{-2}. On 18 April, when sub-canopy snow cover remained continuous, daytime outgoing LWR throughout the day was constantly between 320 and 338 W m^{-2}. Because snow temperature never exceeds 0°C, which corresponds to a maximum LWR emittance of 309 W m^{-2}, the surface temperatures of both litter on the snow surface as well as of trunks and other canopy elements in the view field of the sensor were able to increase outgoing LWR by up to 30 W m^{-2}. However, on 25 April, a further increase in outgoing LWR was evident. While 25 April was warmer than 18 April, the difference in VF_{Ground} (Figure 4.3) substantially altered outgoing longwave radiation, particularly to the East of the transect. Similar to incoming LWR, outgoing LWR above snow-free areas was especially pronounced in the afternoon after several hours of high solar insolation of the ground.

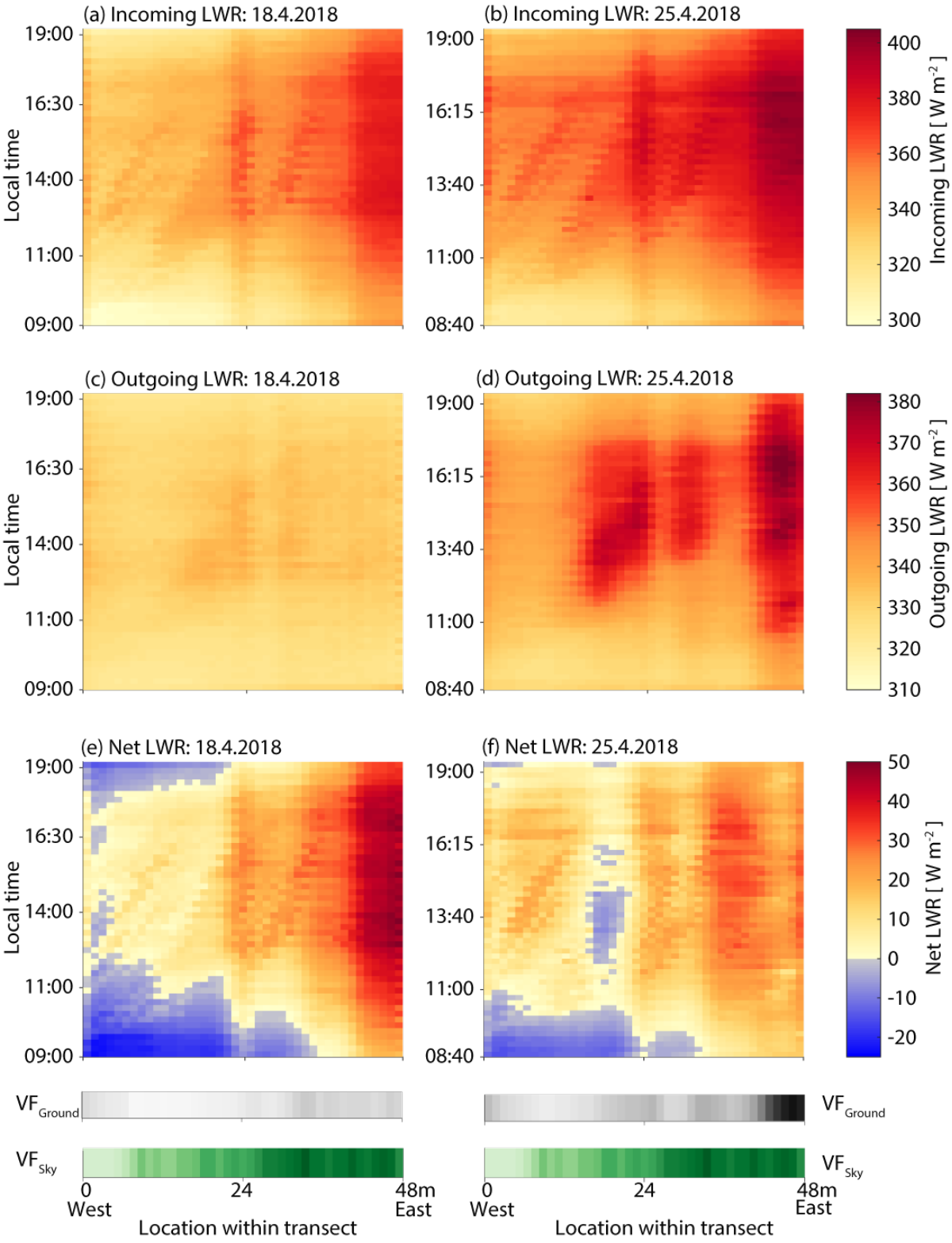

Figure 4.6: Longwave radiation patterns for 18 April (full snow cover) and 25 April 2018 (partial snow cover). (a) and (b) visualize incoming LWR, (c) and (d) outgoing LWR and (e) and (f) net LWR flux ($LWR_{incoming}$ – $LWR_{outgoing}$) for the respective days. The colour bars below show VF_{Ground} (white = 0, black =1) and VF_{Sky} (white = 1, dark green =0) along the transect for each day. Note that VF_{Ground} and VF_{Sky} are quantified in Figure 4.3

The difference between incoming and outgoing LWR resulted in a surface net longwave radiation as visualized in Figure 4.6e-f. On 18 April, the net LWR ranged from net negative downward fluxes of up to 25 W m^{-2} at the more discontinuous western part of the transect, and to a net positive downward flux of up to 50 W m^{-2} at the denser eastern part of the transect. Locations of the highest downward flux on 18 April and the associated increase in energy available for snow melt aligned well with those areas where snow disappeared between 18 and 25 April (see Figure 4.3). As the melt season progressed, increased upwelling LWR over snow-free areas resulted in an attenuation of the net positive downward flux, which occasionally even led to net negative downward fluxes (Figure 4.6f).

Net all-wave radiation

Combining the four components of the radiation budget resulted in net all-wave radiation, which is visualized in Figure 4.7a-b for 18 and 25 April 2018 respectively. At first sight it appeared shortwave radiation dominated the all-wave radiation, but this was only the case when the position of the sun, and the overlying canopy structure allowed direct insolation of the ground surface. In forests, direct insolation of the ground may be restricted to relatively short periods during clear sky days, while positive net longwave radiation may occur over extended periods and across all 24 hours of a day. In the absence of direct insolation, net LWR patterns dominate the net all-wave radiation. Negative net all-wave radiation occurred for 5% of all data points on 18 April and only for 1% of data points on 25 April. These data points tend to also have effective albedo values above 1, further emphasizing the importance of accurately representing sub-canopy effective albedo.

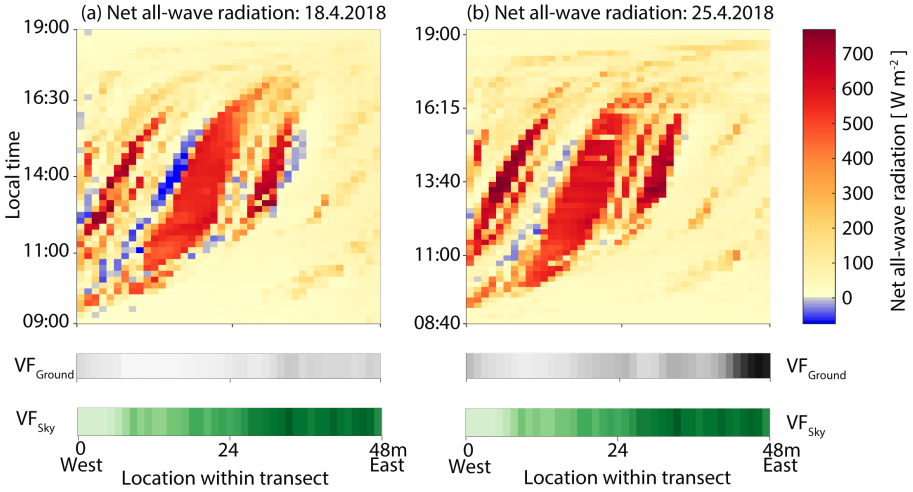

Figure 4.7: Net radiation for (a) 18 April and (b) 25 April 2018. The colour bars below show VF_{Ground} (white = 0, black =1) and VF_{Sky} (white = 1, dark green =0) along the transect for each day, as quantified in Figure 4.3.

4.2.2 Seasonal analysis of shortwave radiation

Extending the analysis to all measurements performed between January and May 2018 (Figure 4.1) allowed investigation of seasonal effects on the relationship between incoming and outgoing SWR. For the purpose of this seasonal analysis, measurements of each cable car transit were spatially averaged. Snow conditions for each measurement day were further classified into either full, partial, or no snow cover. As seen in Figure 4.8, reflected and incoming SWR were constrained by the zenith angle of the sun's position,while the effective albedo decreased with snow cover fraction. Further variation in effective albedo can be explained by snow age, litter, and the fractions of sunlit and shaded snow. Given the spatial averaging of the data presented, effective albedo values above 1 were not recorded. Note that in this analysis, only data acquired during clear sky/partially cloudy conditions (sky emissivity < 0.8) were included. During cloudy conditions, SWR is mostly diffuse and ground shading patterns are less distinct, leading to smaller variations in both incoming and outgoing SWR due to a changing solar angle.

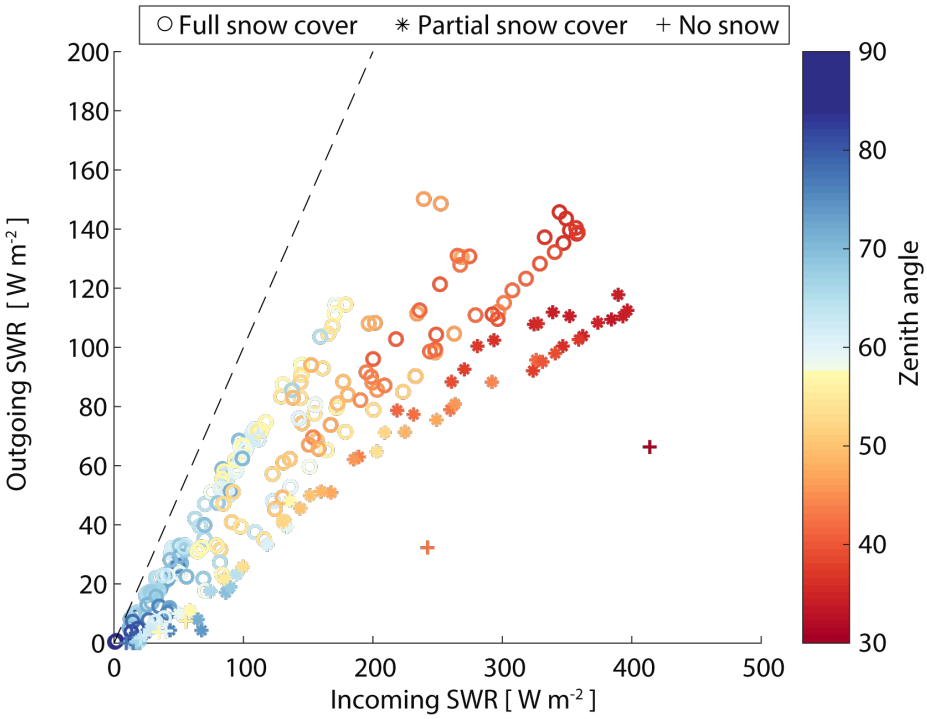

Figure 4.8: Seasonal analysis of reflected vs. incoming SWR. Each data point represents an averaged transect run, colours assign zenith angle and symbol indicates full snow/partial snow cover or no snow conditions. The dashed line is the 1:1 line, indicating an effective albedo of 1.

4.3 Discussion

In-situ measurements of wintertime sub-canopy radiation in an evergreen needle-leaf forest showed high spatiotemporal heterogeneity. Data presented build upon previous studies (Link and Marks, 1999, Sicart et al., 2004, Webster et al., 2016*b*) which monitored spatiotemporal variability of sub-canopy irradiance to illustrate the strong control solar angle and vegetation structure have on the radiation budget of a forested environment, which further governs melt patterns (Sicart et al., 2004, Ellis et al., 2010). However, the novelty of this dataset is the additional spatiotemporal quantification of the view fractions of shaded and sunlit snow, as well as snow cover extent. These were shown to exert strong influence on the outgoing radiation components below a forest stand. The importance of canopy shading for radiative processes in snow-dominated environments has been highlighted by previous studies, as Betts and Ball (1997) observed a lowering of snow albedo due to the effect of canopy shading in boreal forests and Webster and Jonas (2018) showed shading to be of significant importance for effective albedo above a needle leaf evergreen forest. Data presented in this study however, combined sub-canopy shaded/sunlit snow view fractions and radiation measurements, allowing the importance of shading to be quantified on a previously unavailable, spatially and temporally distributed scale.

Solar angle and forest structure controlled the relative position of the sun to the trees and hence the resulting size and shape of canopy shadows on the snow surface (smallest at local solar noon, largest during high zenith angles), which further govern diurnal patterns of shaded/sunlit snow view fractions. The similarity in diurnal patterns and the resulting strong linear relationship between outgoing shortwave radiation and sun-lit-snow view fraction underlines the importance of shading, further demonstrating that it is a key control of the sub-canopy radiation budget.

Energy fluxes have a high seasonal variability which were also represented by highly variable effective albedos during different land surface conditions: no-snow, partial snow, and full snow cover extent. The concept of effective albedo, which applies to complex surfaces where the ratio between up-welling and down-welling radiation is not only a function of the albedo of individual surface elements, has been used in studies investigating its dynamics over rough snow and ice surfaces (Pirazzini, 2004, Lhermitte et al., 2014), over mountainous terrain (Weihs et al., 2001) as well as in urban settings (Sailor and Fan, 2002). Surface reflectance properties are hence combined with multiple reflections and local shading phenomena. Measured effective albedo was shown to decrease through the winter season. While this study only investigated the effect of partial snow cover, littering from canopy debris (Winkler et al., 2010) as well as snow ageing due to increased surface grain

size (Wiscombe and Warren, 1980) and thinning of the snow cover (allowing absorbance by ground) further affected seasonal albedo development. The highest effective albedo values were measured mid-winter, when solar irradiance was generally low. Under these conditions, the effect of albedo on climatic processes tends to be smaller than during springtime when high insolation increases its importance (Kuusinen et al., 2012). Consequently, accurately quantifying partial snow cover when aiming to calculate sub-canopy outgoing shortwave radiation and the resulting effective albedo, is of major importance for land surface modelling.

In addition to affecting shortwave fluxes, the presence of canopies also altered longwave radiation fluxes. Forest structure determined the relative importance of longwave radiation, as proximity to denser forest surroundings coincided with stronger longwave radiation enhancement, which is in line with findings of previous studies (Pomeroy et al., 2009, Klos and Link, 2018). Sicart et al. (2004) demonstrated that during low solar irradiance, in combination with full snow cover (high effective albedo) and low atmospheric emissivity, canopy induced attenuation of shortwave radiation is offset by longwave enhancement, further increasing net all-wave radiation and impacting snow melt patterns. Results obtained from the cable car system affirm this result. During full snow cover conditions, measured net positive downward LWR fluxes during springtime were of similar magnitude (50-60 W m^{-2}) to previous studies (Webster et al., 2016*b*, Musselman and Pomeroy, 2017). Magnitudes of peak sub-canopy incoming longwave radiation further increased throughout the melt period due to amplified air and canopy temperatures, which supports results by Webster et al. (2016*b*). The cable car system further allowed quantification of snow cover extent over a spatially distributed area and related it to outgoing longwave radiation. During partial snow cover conditions, outgoing longwave radiation was dependent on snow cover extent, as areas of bare ground increased the outgoing longwave radiation by up to 60 W m^{-2}, increasing the potential for negative net longwave radiation. The relationship between solar angle and timing of heat storage and release by both the canopy and bare ground during fractional snow cover conditions is an important aspect that should be considered when modelling sub-canopy longwave radiation (Pomeroy et al., 2009, Webster et al., 2016*b*).

Furthermore, explicitly solving for shaded surfaces below a forest canopy as well as separating between direct and diffuse radiation can considerably upgrade land surface modelling. Musselman et al. (2015) found that by conceptualizing canopy gaps as circular cylinders and explicitly resolving shading in a ray tracing model environment, the spatially heterogeneous diurnal radiation of a forest gap could be simulated more reliably. The potential for inclusion of shading in large scale modelling is increasing, as recent land surface model developments have started to incorporate the 3-D canopy structures (Yuan

et al., 2014) as well modifying the commonly used two-stream approximation to account for horizontally heterogeneous canopy structures (Yuan et al., 2017). Accounting for the effects of shading and fractional snow cover on the sub-canopy radiation budget should be a priority for further land-surface model enhancement across forested environments.

4.4 Chapter summary

A custom-made cable car system enabled high-resolution up-looking and down-looking shortwave and longwave radiation measurements with simultaneous hemispherical photographs of the ground conditions. This allowed quantification of the influence of shading and fractional snow cover on the sub-canopy radiation budget. Spatiotemporal analysis of data collected during a clear-sky day revealed a strong linear relationship between outgoing shortwave radiation and sunlit snow-view fraction ($R = 0.94$), highlighting shading as a key control of the sub-canopy shortwave radiation budget. Fractional snow cover was shown to be of particular importance for outgoing longwave radiation, with locations of diminished snow cover showing an increase in outgoing longwave radiation of up to 60 W m^{-2}. Net all-wave radiation was dominated by shortwave radiation whenever direct insolation of the forest floor occurred; however, at times and locations where canopy structure inhibited direct insolation (which is the case during most of the day), longwave radiation was controlling the sub-canopy radiation budget.

Chapter 5

Land surface albedo in seasonally snow-covered forest stands

Building on results from Chapter 4, in this chapter the perspective is changed from below to above canopy radiation, as part two of research question 1 (RQ1b) is addressed:

What processes control land surface albedo (LSA) in seasonally snow-covered forested environments?

Answering this research question requires spatially and temporally distributed LSA observations over snow-covered forest stands. One method to obtain such data are tower-based weather station measurements at individual points above forest canopies (e.g. Kuusinen et al., 2012, Bartlett and Verseghy, 2015), resulting in high temporal but low spatial resolution. Another method to acquire such information is to use remotely-sensed satellite data. However, at the resolution of commonly-used satellite data (e.g. MODIS MOD10A1 500m grid), forest heterogeneities such as canopy gaps and edges are not resolved. While higher resolution satellite albedo retrievals are becoming more widely available (e.g. 30m LANDSAT or sub-meter scale Worldview4 by Digital Globe), the spatial and temporal resolution is still not high enough for such data to be used as a benchmark to investigate forest-induced variability of wintertime LSA. A possible solution towards mitigating this data gap are airborne platforms (e.g. Lundquist et al. (2018)) which, when compared to stationary tower measurements, allow for variable measurement heights and the flexibility to obtain data at many locations above a forest canopy. The resulting increased measurement resolution enables impacts of spatially and temporally varying factors to be investigated (e.g. the effect of canopy structure on LSA).

This study uses a uncrewed aerial vehicle (UAV) system, which was previously introduced in Section 3.1.2. UAV measurements of LSA coupled to coincident down-looking hemispherical images over snow-covered forests are used to investigate the effects of (a) tree species, (b)

intercepted snow, (c) solar angle, (d) meteorological boundary conditions and (e) fractional snow cover on wintertime LSA. Extensive air-borne broadband LSA measurements were taken over a large range of canopy structures in two climatically different locations (Switzerland and Finland), across wide ranges of solar zenith and azimuth angles. Field sites used for this study are described in detail in Section 3.2.

Parts of this chapter are under review as "*Effect of forest canopy structure on wintertime Land Surface Albedo: Evaluating CLM5 simulations with in-situ measurements*" in Journal of Geophysical Research: Atmospheres.

5.1 Methods

5.1.1 Calculation of hemispherical view fractions

In a similar manner to hemispherical images taken with the cable car setup (Section 4.1.2), the UAV-borne 180° down-looking hemispherical images had to be binarized, discretized and analysed. Similar techniques as introduced in Section 4.1.2 were used for this purpose: First, the land cover descriptors canopy-view fraction (VF_{Canopy}) and snow-view fraction (VF_{Snow}) were obtained from the ratio between black and white pixels within each analysis ring, which were further weighted by the sine of the elevation angle. VF_{Snow} was then split into sunlit snow-view fraction (VF_{Sun}) and shaded snow-view fraction (VF_{Shade}) based on a secondary binarization and analysis. Figure 5.1 shows an example down-looking hemispherical photograph as well as the resulting categorized image, demonstrating the spatial extents of the corresponding view-fractions.

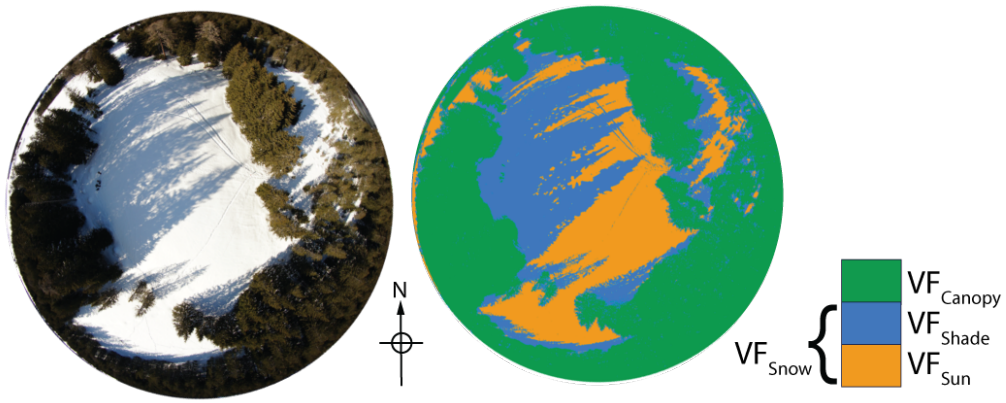

Figure 5.1: Example of a down-looking hemispherical photograph, taken on 14 March 2018, 14:02 UTC+1, at waypoint 9 (see Table 3.3) in Davos Laret, Switzerland, and the resulting analyzed hemispherical image with respective view-fractions colored in.

5.1.2 Classification of interception loads

In addition to providing means to quantify shading extents, the down-looking hemispherical images were used to classify measurements into full interception, partial interception and no interception conditions. Due to practical constraints and a limited number of interception events, this classification was done manually. Figure 5.2 gives an example of the same waypoint with an interception state of (a) full snow (b) partial snow and (c) no snow. All interception events were captured at the Davos Laret site in Switzerland. Full interception load measurements were obtained on 3 measurement days (20.01.2018, 22.03.2018, 12.03.2019), resulting in a total of 84 waypoint measurements of LSA. 5 measurement days (09.02.2018, 13.02.2018, 23.02.2018, 08.03.2018, 16.01.2019) with 99 UAV waypoint measurements were classified as partial interception conditions. An additional 5 measurement days (29.01.2018, 14.03.2018, 06.04.2018, 16.04.2018, 18.04.2018), with a total of 133 UAV measurement points of LSA were made during no snow in the forest canopy conditions.

(a) Full snow **(b)** Partial snow **(c)** No snow

Figure 5.2: Example of full snow, partial snow and no snow interception conditions at the same waypoint in Davos Laret.

5.1.3 Calculation of effective emissivity of the sky

Effective emissivity of the sky (ϵ_{Sky}) is a measure of meteorological conditions and was used in this study to distinguish various stages of overcast from clear-sky conditions. Given measured atmospheric longwave radiation (LWR_{atm}) and near-surface air temperature (T_{air}), ϵ_{Sky} is calculated by rearranging the Stefan Boltzmann equation introduced in Equation (2.5):

$$\epsilon_{Sky} = \frac{LWR_{atm}}{\sigma {T_{air}}^4} \tag{5.1}$$

For each field site and measurement campaign, LWR_{atm} and T_{air} were acquired by an Automatic Weather Station (AWS) in the vicinity of the field site (see Section 3.1.3).

During overcast conditions, only small contrasts between the brightness temperature of the sky and T_{air} exist, hence leading to ϵ_{Sky} close to 1 or even exceeding 1. For clear-sky conditions, the temperature difference is more distinct, as high incoming solar radiation increases T_{air} while simultaneously decreasing LWR_{atm}, resulting in ϵ_{Sky} values as low as 0.6.

5.2 Results

Results in the following sections are based on 1553 UAV measurement points, taken on 30 different measurement days, spread throughout two winter seasons, in two different climate zones, at 6 distinct field sites. This extensive dataset is used to investigate the impact of tree species, intercepted snow, solar angle, meteorological boundary conditions and fractional snow cover on LSA.

5.2.1 Tree species

LSA was extensively measured in alpine, sub-alpine and boreal forest biomes. Among these measurements, six different tree species were captured, three of which were classified as deciduous and three as needle-leaf evergreen trees. The captured deciduous tree species consisted of birch (genus *Betula*), larch (genus *Larix*) and beech (genus *Fagus*). Needle-leaf evergreen tree species captured by this study included spruce (genus *Picea*), Scots pine (genus *Pinus sylvestris*) and Swiss/stone pine (genus *Pinus pinea/Pinus cembra*). The locations and characteristics of these sites are further described in Section 3.2.

For each tree species, all LSA measurements taken under clear sky ($\epsilon_{Sky} < 0.85$), full snow cover, no interception conditions are combined. While each site had specific characteristics, Figure 5.3 gives indications about the overall patterns of clear sky LSA with respect to tree species. The spread in LSA within the same tree species is due to differences in canopy structure, solar angle and snow albedo itself. Differences within needle-leaf evergreen trees (pine, spruce) and within deciduous trees (birch, larch, beech) remain small and the respective interquartile ranges overlap, suggesting non statistically significant differences in LSA between the individual species. However, results show a clear distinction between deciduous and needle-leaf tree species, as deciduous forests have a higher median LSA (0.28-0.30) compared to needle-leaf forests (0.12-0.21), further underlining differences in the snow-masking effect of the respective tree species. Figure 5.4 further visualizes these differences, as a clear separation between the LSA distribution peak of deciduous and of the needle-leaf evergreen trees is evident. Furthermore, the medians lie outside of the other box entirely, and the interquartile ranges are not overlapping.

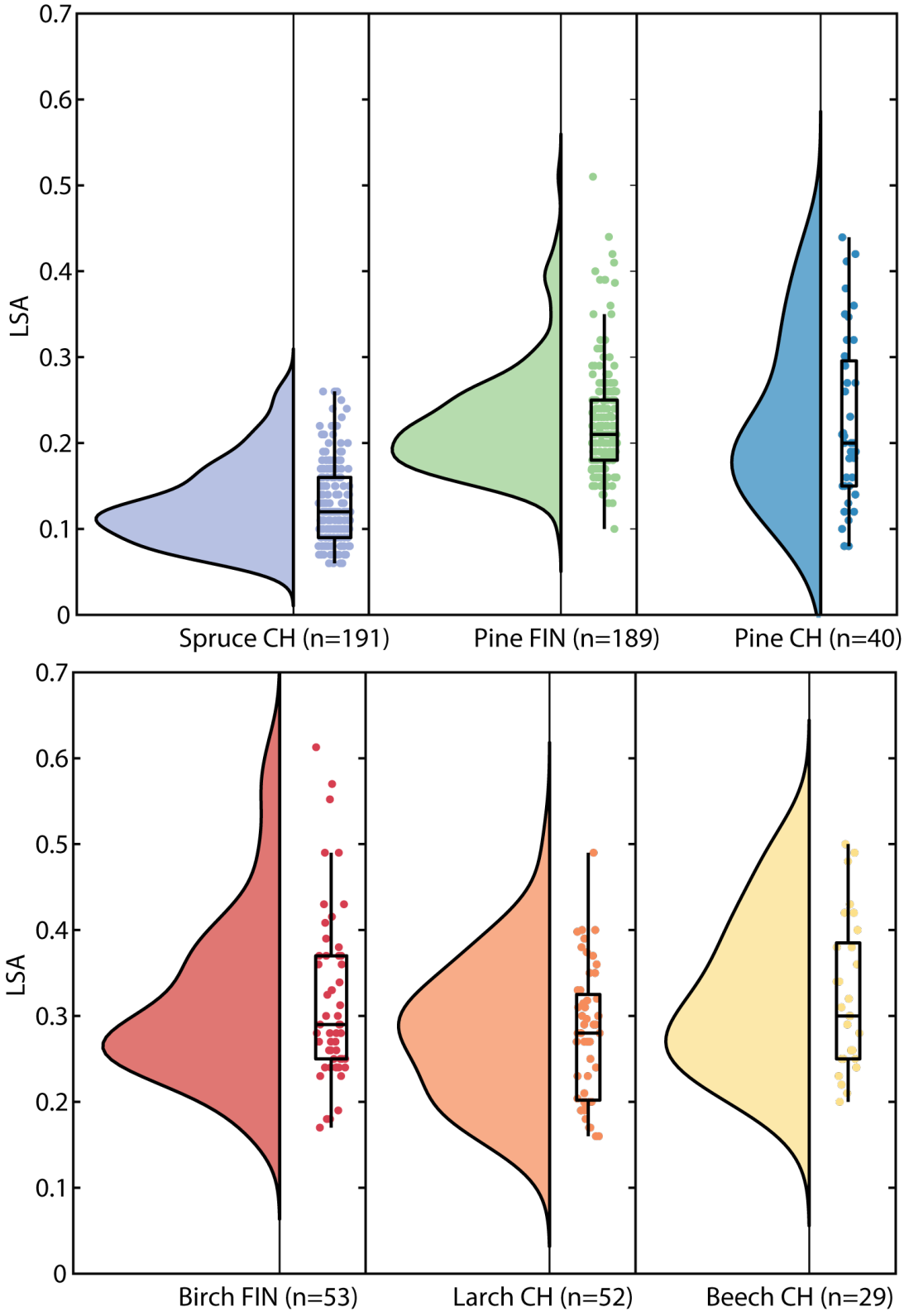

Figure 5.3: Raincloud plots (Allen et al., 2019) showing distribution, box plot and data points of LSA measurements for various tree species. Only data collected on clear sky days ($\epsilon_{Sky} < 0.85$) with no interception in the forest canopies are included. Bottom and top of each box indicate 25% and 75% percentiles, central line represents the median and whiskers indicate 1.5 times the interquartile range.

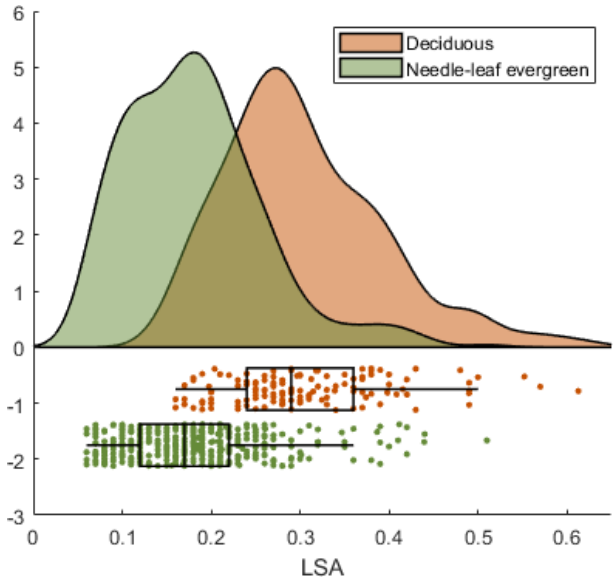

Figure 5.4: Raincloud plot (Allen et al., 2019) showing distribution, box plot and data points of LSA measurements for deciduous and needle-leaf evergreen trees. Only data collected on clear sky days ($\epsilon_{Sky} < 0.85$) with no interception in the forest canopies are included. Bottom and top of each box indicate 25% and 75% percentiles, central line represents the median and whiskers indicate 1.5 times the interquartile range.

5.2.2 Interception

Intercepted snow in the canopy decreases the snow-masking effect of forests, leading to increased LSA values of forested environments following snowfall events (Stähli et al., 2009). Intercepted snow conditions were captured at the Davos Laret field site with the predominant species being Norway spruce. Figure 5.5(a) contrasts LSA and VF_{Snow} (the fraction of snow visible from the view-point of the down-looking radiation sensor, used as a measure of forest sparsity here), for flights performed under under "No interception", "Partial interception" and "Full interception" conditions. Each data-point represents data from UAV measurements at one unique WP. Note that in this analysis, VF_{Snow} does not take intercepted snow into account, which explains the vertical alignment of measurement points for the respective waypoints. The maximum measured difference in LSA between "No interception" and "Full interception" was 0.32. Higher VF_{Snow} showed a larger overall spread in LSA, while lower VF_{Snow} showed a larger difference between no interception, partial interception and full interception conditions. Figure 5.5(b) visualizes the differences in median LSA between full interception (0.22), partial interception (0.16) and no interception (0.12). From Figure 5.6 it becomes evident that although medians between no interception and full interception conditions differed substantially, there is much distribution overlap. This occurs due to the large spread in full-interception LSA measurements, which can be partially attributed to the integration across the spatial dimension, e.g. across all waypoints. A Wilcoxon–Mann–Whitney rank test (Wilks, 2006),

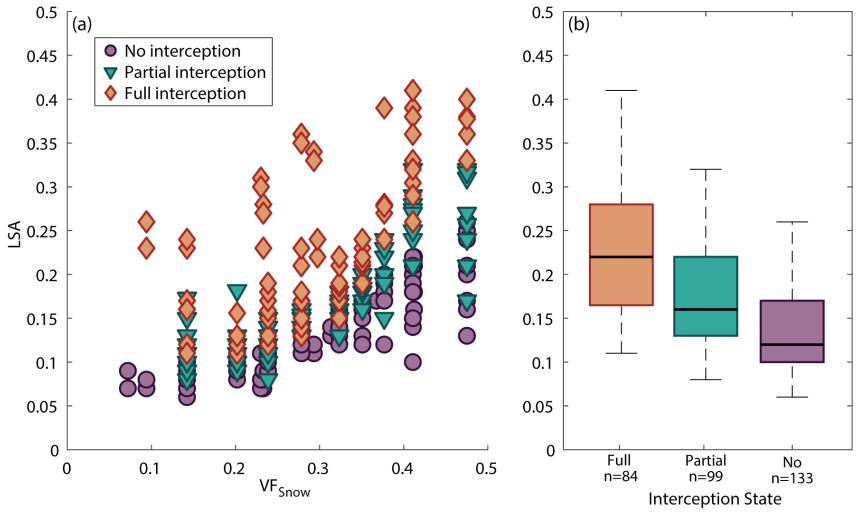

Figure 5.5: Effects of partial and full interception on LSA above a spruce forest stand in Switzerland. (a) LSA vs. VF_{Snow} for full interception, some interception and no interception conditions. (b) visualization of summary statistics for measured LSA under the three interception stages: bottom and top of each box indicate 25% and 75% percentiles, central line represents the median and whiskers indicate 1.5 times the interquartile range.

which is a nonparametric test with no assumptions about the underlying distribution of the data, was applied to determine whether differences in LSA under varying interception conditions were significant. Results indicate that differences between intercepted and no intercepted conditions were significant ($p < 0.0002$), further underlining that intercepted snow on the forest canopy is a driver of LSA, and needs to be accounted for in land surface models across scales.

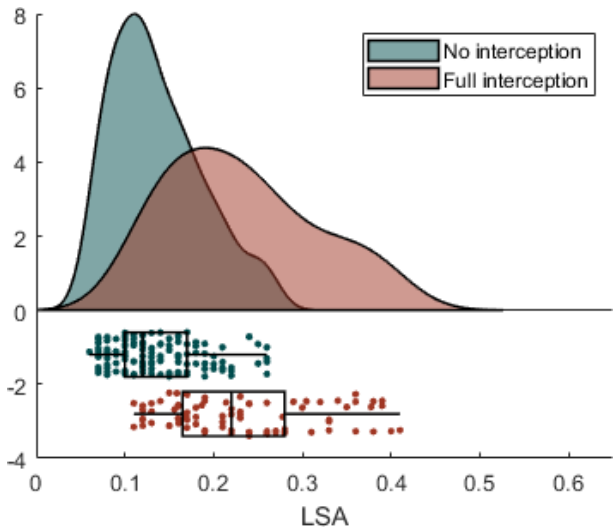

Figure 5.6: Raincloud plot (Allen et al., 2019) contrasting distribution, box plot and data points for LSA measurements taken during full and no interception conditions.

5.2.3 Solar Angle and Shading

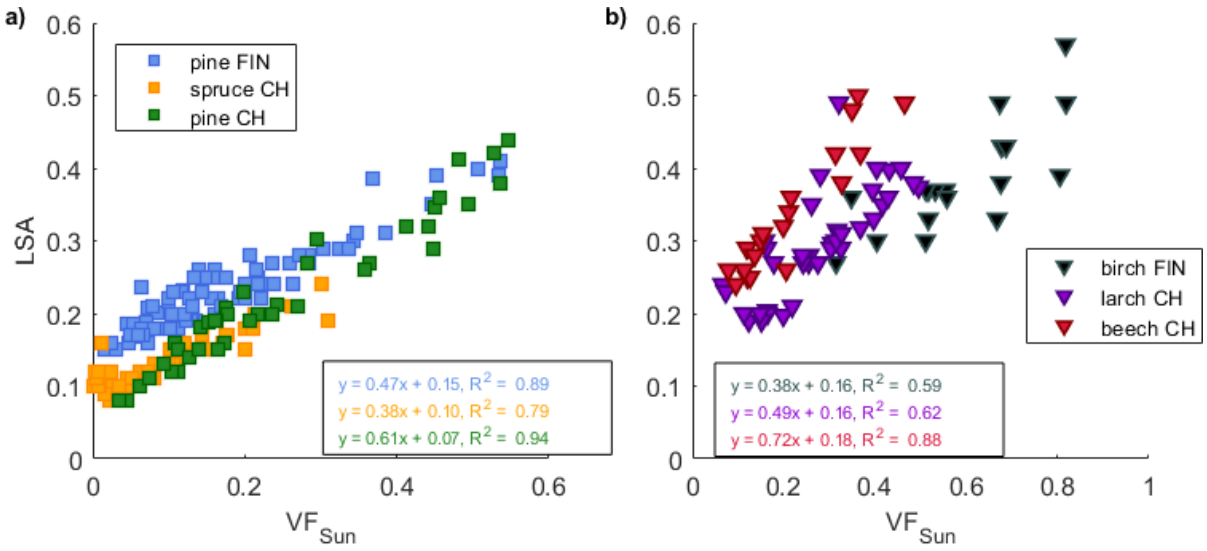

Figure 5.7: UAV measurements of LSA compared with VF_{Sun} for a) needleleaf, and b) deciduous forest environments. Data were collected during clear sky days. All correlations were statistically significant with p-values < 0.0002.

In forested environments, solar angle influences LSA by changing the extent of the canopy structural shading of the snow surface. In this part of the study, the UAV-borne LSA measurements allowed a diurnal analysis of LSA in relation to solar position and canopy structure at needle-leaf and broad-leaf forests. Figure 5.7 shows all LSA measurements taken during clear sky ($\epsilon_{Sky} < 0.85$), full snow cover, and no interception conditions. Each data point represents a measurement captured at a WP, unique in terms of its LSA and locally-measured VF_{Sun}, the sun-lit snow view fraction. Thus, the dataset presented in Figure 5.7 again integrates across the spatial (different WPs within each site) and temporal (repeated measurements throughout the day) dimension. Strong positive relationships between LSA and VF_{Sun} were found at all sites, all of which were statistically significant. Relationships were stronger for needle-leaf sites ($R^2 = 0.79 - 0.94$) compared to deciduous sites ($R^2 = 0.59 - 0.88$). A linear regression model was fitted to data points from each field site, indicating y-intercepts between 0.07 and 0.18 and gradients between 0.38 and 0.72 for sites with deciduous environments and gradients between 0.38 and 0.61 for sites in needle-leaf forest environments. The strong positive relationships suggest that canopy structural shading of the snow surface is exerting a primary control on LSA on clear sky days. Note again that each site encompassed several WPs, hence, in this evaluation, variation in VF_{Sun} is a function of the zenith and azimuth angle of the solar position as well as the local VF_{Snow}, which is explaining some of the spread.

Effect of solar zenith angle

To disentangle the effects of zenith angle and VF_{Snow} on LSA, data from a series of flights at the spruce site in Davos Laret over the course of one day is shown (Figure 5.8). At waypoints where the forest canopy is sparse ($VF_{Snow} > 0.3$), LSA decreases by up to 11% as zenith angle increases. This occurs due to the fact that an increasing solar zenith angle corresponds to an increased canopy shaded area of the snow surface, as long as the canopy is sparse enough to permit direct insolation of the forest floor.

Most of the decline in LSA happens at low to medium zenith angles (35 – 55°), while there is only a slight further decrease towards very large zenith angles (>75°) following sunrise and preceding sunset. In contrast, at waypoints with denser canopy ($VF_{Snow} < 0.25$), LSA was seen to increase by a few percent as zenith angle increases. In denser forest the proportion of sunlit snow is low at all times, and sun flecks become rare even in the middle of the day. As the solar zenith angle increases, the proportion of diffuse radiation in incoming solar radiation also increases. Hence, below a certain VF_{Snow}, this increase in diffuse radiation and the corresponding increase in multiple scattering leads to higher LSA around sunrise and sunset.

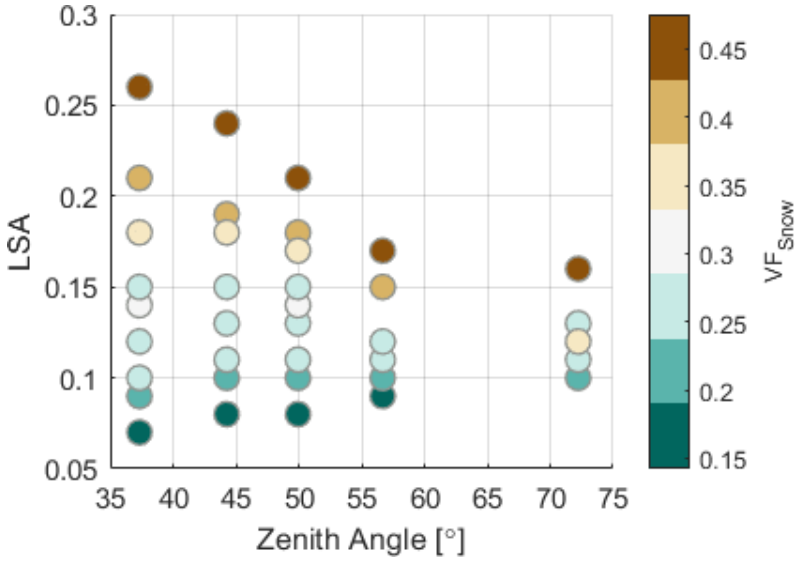

Figure 5.8: Measurements of LSA at different zenith angles and snow view fractions for a single clear sky day (18.4.18) at the spruce site in Davos Laret, Switzerland.

Effect of solar azimuth angle

In addition to zenith angle, the azimuth can also be important for LSA, as it controls the orientation of shadows on the snow surface. As an illustrative example data from the boreal pine site in Sodankylä is presented (Figure 5.9). The location of trees and

canopy gaps in relation to the solar position resulted in a large proportion of the snow surface being sunlit in the morning, while the site had a smaller sunlit view fraction at the same zenith angle in the afternoon. This resulted in a non-symmetrical diurnal signal of measured LSA during a clear sky day (Figure 5.9), with minimal change in LSA during the first half of the day, followed by a clear decrease in LSA of sparse WPs (canopy coverage $< 50\%$) during the afternoon.

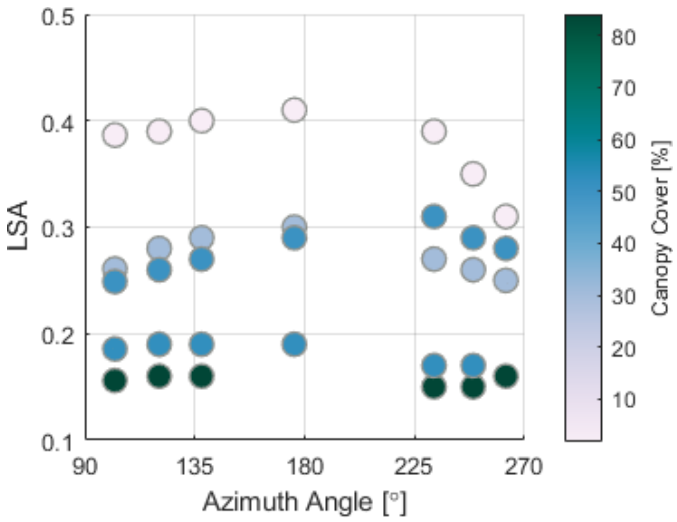

Figure 5.9: Measured LSA as a function of azimuth angle, on 26 April 2019 at the boreal pine site (Sodankylä, FIN). Color represents canopy coverage of individual WPs derived from CHMs.

5.2.4 Meteorological conditions

Meteorological boundary conditions can further influence LSA in seasonally snow-covered forests. Increased cloudiness generally corresponds to an increase in multiple scattering, leading to a higher LSA. However, during overcast conditions the potential for snow to be sunlit is diminished, leading to lower LSA values. Figure 5.10a contrasts LSA and ϵ_{sky} as a function of VF_{Snow} for the birch and pine sites in Sodankylä, Finland and the spruce site in Davos Laret, Switzerland. For denser forests ($VF_{Snow} < 0.4$), the difference in LSA between cloudy and clear sky conditions is small. No clear signal could be obtained from measurements conducted in sparse forests ($VF_{Snow} > 0.6$). Figure 5.10b further visualizes differences in LSA between cloudy and clear sky conditions. The median for LSA in cloudy conditions (0.12) is smaller compared to clear sky conditions (0.18), while the peak of the distribution function is steeper under cloudy conditions. Additionally, the spread in LSA for cloudy conditions appears to be smaller compared to clear sky conditions, although this could be due to the disproportionally small amount of measurements conducted in cloudy conditions.

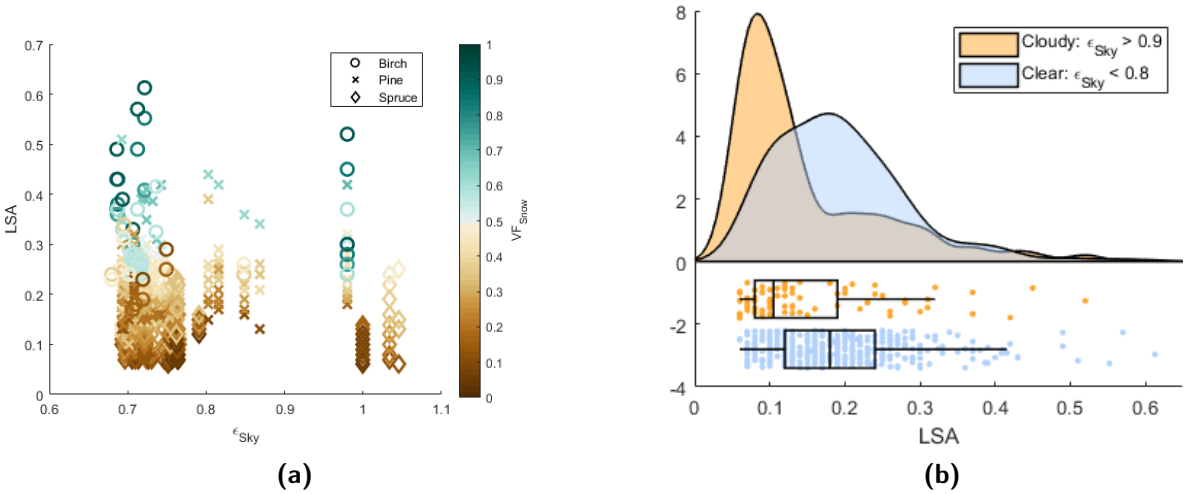

Figure 5.10: (a) UAV measurements of LSA compared with emissivity of the sky. Colour represents VF_{Snow} of individual WPs derived from down-looking hemispherical photographs. (b) Raincloud plot (Allen et al., 2019) showing distribution, box plot and data points for cloudy ($\epsilon_{Sky} > 0.9$) and clear sky ($\epsilon_{Sky} < 0.8$) conditions.

5.2.5 Fractional snow cover

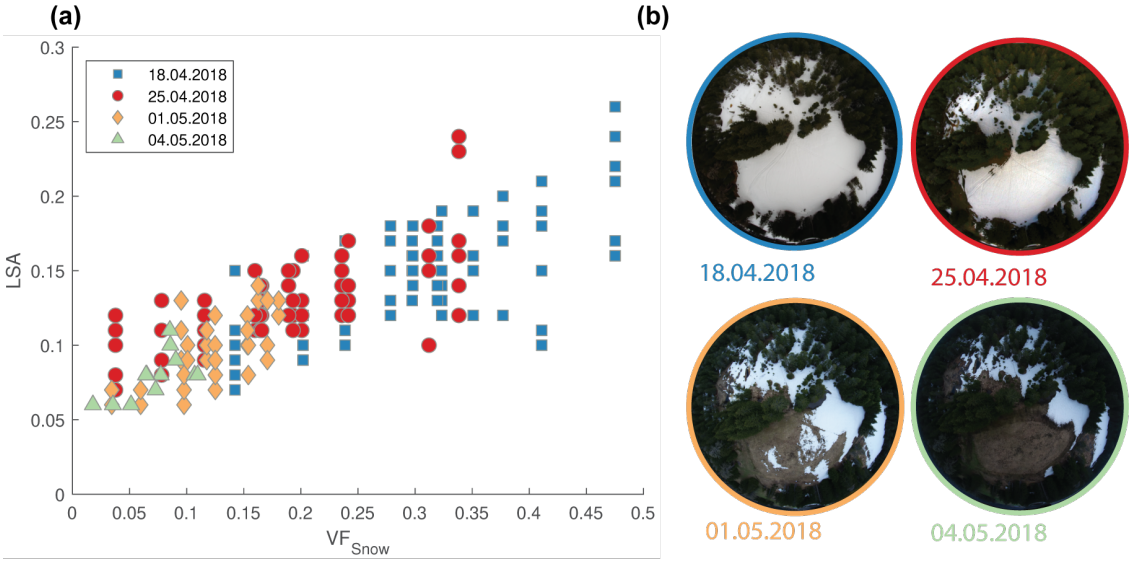

Figure 5.11: (a) UAV measurements of LSA compared with VF_{Snow} for the spruce site in Davos Laret from 3 measurement days during the melt period in the spring of 2018. (b) visualizes snow depletion for one particular WP between 18 April 2018 and 4 May 2018.

During the melt period in the spring, snow cover extent (SCE) transitions from full snow cover through the various stages of fractional snow cover until complete snow disappearance is reached. The effects of fractional snow cover on effective LSA were explored at three sites: the spruce site in Davos Laret during the 2018 melt period, and the pine and birch site in Sodankylä during the 2019 melt period. At each site, reference full-snow-cover

measurements were first conducted on a clear sky day before the onset of the melt-period. Subsequently, the sites were revisited at various points of the melting season (twice at pine site, three times at birch and spruce site). At each site, the same flight plan was used for the full-snow-cover flight as for the partial-snow-cover flights (see Section 3.2 for more detail), allowing to evaluate melting patterns at each distinct WP.

Figure 5.11(b) shows a series of hemispherical images to illustrate the development of the snow cover extent at WP1 of the spruce site throughout this transition: it starts with full (100%) snow cover conditions (18.04.2018), which diminishes to 80% (25.04.2018), to 44% (01.05.2018) and further to 19% (04.05.2018). Figure 5.12(b) and Figure 5.13(b) show similar developments for the birch and pine site. Note that at each individual WP snow-melt occurred at different rates. Figure 5.11(b), Figure 5.12(b) and Figure 5.13(b) are hence each only visualizing the SCE development of one exemplary WP.

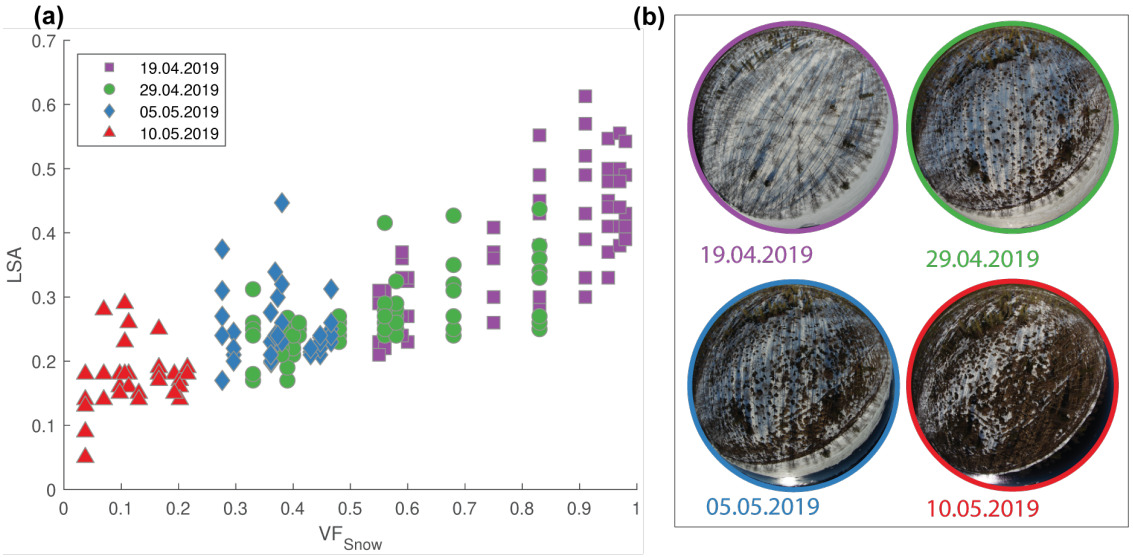

Figure 5.12: (a) VF_{Snow} versus LSA for the birch site in Sodankylä from 4 measurement days during the melt period in the spring of 2019. (b) visualizes snow depletion for one WP during those days.

To investigate the effect of fractional snow cover on LSA VF_{Snow} for each WP at each point in time was compared with the concurrently measured LSA. Results show positive relationships between LSA and VF_{Snow} for all three cases (see Figure 5.11(a), Figure 5.12(a), Figure 5.13(a)). In those figures, all flights performed at the individual WPs at the day of interest are included, explaining the vertical alignment of several LSA measurements in each of the graphs. At the sparser sites, differences in snow albedo itself contribute to the spread, as the snow continues to age and get shallower as the melt progresses, further affecting LSA.

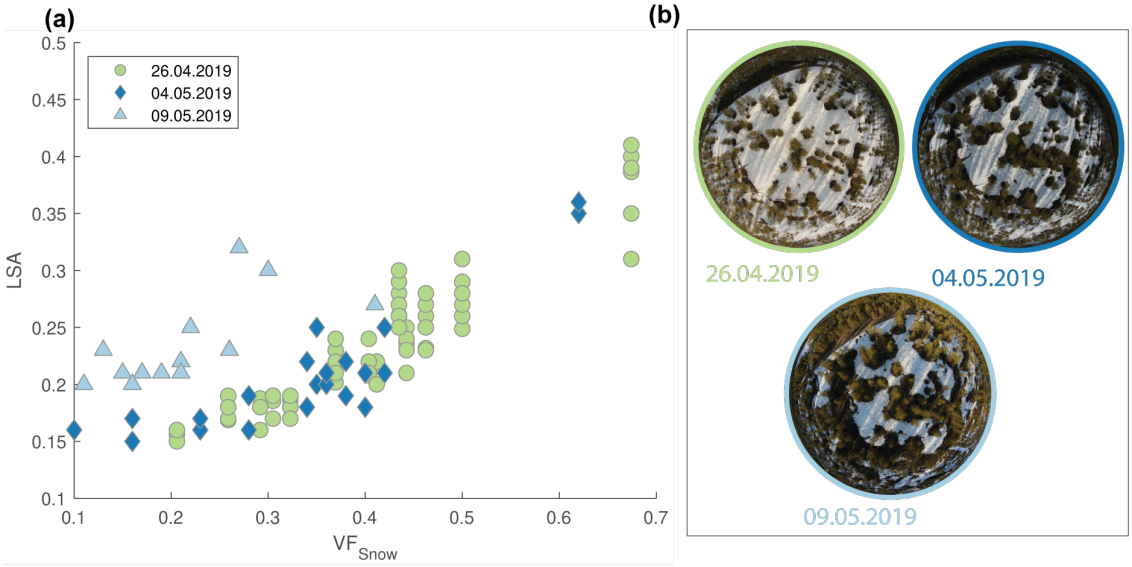

Figure 5.13: (a) VF_{Snow} versus LSA for the pine site in Sodankylä from 3 measurement days during the melt period in the spring of 2019. (b) visualizes snow depletion for one WP during those days.

5.3 Discussion

UAV-based measurements of LSA over seasonally snow-covered forest stands showed high spatiotemporal heterogeneity of LSA. In this study, the observed forest-induced heterogeneity of LSA was investigated with regards to the individual effects of tree species, interception events, solar angle, meteorological boundary conditions and fractional snow cover. Investigation of the dependency of LSA on tree species in both sub-alpine and boreal forest environments showed clear differences in the snow-masking effect of vegetation between needle-leaf and deciduous forest stands. Implications of this have previously been demonstrated by Loranty et al. (2014) who compared satellite observations and coupled climate model representations of LSA and and found simulated LSA of deciduous forests to be substantially larger than of needle-leaf forests. Furthermore, they found significantly worse model agreement with observed LSA for deciduous and mixed forest stands compared to needle-leaf forests. The finding was attributed to the fact that bio-physical characterization of forests relies heavily on needle-leaf evergreen forests, whereas deciduous and mixed forests remain poorly characterized in land surface models. Measurement results presented in this study, e.g. the clear differences between deciduous and needle-leaf LSA, underline the importance of addressing this shortcoming in future model development.

UAV-based measurements of LSA further showed intercepted snow in the canopy to be a strong modulator of LSA. Changes of LSA in response to intercepted snow in forest canopies have previously been reported by Stähli et al. (2009) and Bartlett and Verseghy (2015). Their studies, however, were based on stationary tower measurements, which are typically

located in relatively continuous forests and hence fail to incorporate the effect of gaps and edges. Webster and Jonas (2018) also performed UAV-based measurements of LSA during intercepted snow conditions, showing similar results to this study. The combination of the data collected by Webster and Jonas (2018) and measurements taken in this study creates a valuable dataset for future model evaluation efforts. Model representation of intercepted snow and unloading is paramount for accurate simulation of LSA (Stähli et al., 2009, Bartlett and Verseghy, 2015), which has received attention in recent land surface model development efforts. For example, a key new feature of the Community Land Model 5.0 (CLM5) is the introduction of separate storage terms for liquid and solid water phases in the canopy, with intercepted snow subject to wind- and temperature-induced unloading events (Lawrence et al., 2019). However, such parametrizations are based on tower measurements and/or satellite retrievals of LSA above needle-leaf evergreen forests, hence not incorporating discontinuous forest stands. Therefore, an avenue for future research is evaluating model performance of simulated LSA during intercepted snow conditions at heterogeneous forest stands.

This study further investigates the effects of solar angle and canopy structural shading on LSA. Statistical analysis demonstrated a strong positive correlation between LSA and VF_{Sun} across a large range of canopy structures in two climatically different locations. This highlights that canopy shading has a strong influence on LSA during clear sky conditions across a much wider range of canopy structures and plant functional types than initially demonstrated by Webster and Jonas (2018). In addition, results in this study strengthen the spatial transferability of shading as a key control on outgoing shortwave radiation below the forest canopy, shown at a single site by Malle et al. (2019). Overall, sub- and above-canopy measurements from these three studies demonstrate the importance of canopy shading for radiative processes in snow-dominated environments. This is underlined by canopy shading of the snow surface being controlled by the geometrical arrangement of trees in relation to the position of the sun and UAV measurements of LSA showing that both solar zenith and azimuth angles control the diurnal variability of LSA.

Additionally, this study examined influences of meteorological boundary conditions on LSA. LSA measurements taken during overcast conditions showed slightly less temporal variability compared to clear-sky conditions, but no statistically significant results could be drawn from the collected data. The effect of cloud cover on LSA has been studied extensively in unforested areas, suggesting snow albedos to be 3-15% higher on overcast days compared to clear-sky days (Carroll and Fitch, 1981, Konzelmann and Ohmura, 1995, Jonsell et al., 2003). This phenomena can be explained by three facts: (1) on overcast days, the vast majority of solar radiation is diffuse; (2) reflectance of snow is larger in visible than in infrared wavelengths and (3) diffuse radiation consists of a larger amount

of visible wavelengths (Wiscombe and Warren, 1980). Reflectance of vegetation, however, is not larger in the visible wavelengths, creating a less perspicuous case for seasonally snow-covered forest stands. Overall, LSA measurements taken for this study indicated higher LSA values during clear sky conditions compared to overcast conditions, which is in contrast to some previous studies (e.g. Betts and Ball, 1997) but in accordance with other studies (e.g. Kuusinen et al., 2012). However, analysis in this study was hampered by a disproportionally small amount of measurements conducted in cloudy conditions, suggesting the need for larger datasets of LSA under cloudy conditions in future studies.

The final part of this study explored the effects of SCE on LSA. Data from repeated flights during the snow-melt period demonstrated a positively correlated relationship between LSA and VF_{Snow}, whereby VF_{Snow} was used as an absolute SCE descriptor. During the snow melt season, as SCE transitions from 100% to 0%, solar insolation is high (e.g. $>$ 1000 W m^{-2} around solar noon in sub-alpine forests) compared to early or mid-winter. Consequently, accurately quantifying SCE in land surface models is of profound importance, as the effect of LSA on climatic processes tends to be amplified during springtime (Kuusinen et al., 2012). Furthermore, especially as the climate warms, SCE is a crucial indicator for snow cover changes in climate predictions (Mudryk et al., 2020). In addition to SCE, littering from canopy debris (e.g. Winkler et al., 2010) as well as snow aging due to increased surface grain size (Wiscombe and Warren, 1980) and thinning of the snow cover (allowing absorbance by the ground) affect LSA. Singling out their individual effects as well as evaluating their respective model representations requires further work by the scientific forest-snow community.

5.4 Chapter Summary

This study used temporally and spatially distributed in-situ measurements of Land Surface Albedo (LSA) to investigate the driving factors that control LSA in a seasonally snow-covered forest environment. An extensive dataset of airborne LSA measurements using an uncrewed aerial vehicle (UAV) collected directly alongside canopy structure and snow surface shading information, captured a large range of canopy structures and solar angles in alpine and sub-alpine (Switzerland) as well as boreal (Finland) locations. Clear differences in LSA were found between deciduous and needle-leaf evergreen forests, while no clear effect of overcast conditions on LSA was found. Intercepted snow in the canopy was shown to be a driver of LSA. Measurements conducted during various snow cover extent stages revealed a positive relationship between LSA and the fraction of snow visible from the view-point of the down-looking radiation sensor. Measurements further revealed a strong correlation between LSA and sunlit snow across a range of tree species, solar angles

and canopy structures, suggesting that canopy structural shading of the snow surface is exerting a primary control on LSA on clear sky days.

Chapter 6

Effect of forest canopy structure on wintertime Land Surface Albedo: Evaluating CLM5 simulations with in-situ measurements

The previous chapter demonstrated a large spatial and temporal heterogeneity in Land Surface Albedo (LSA) across seasonally snow covered forest stands. Different factors (e.g. shading of the snow, intercepted snow in the canopy) were shown to control LSA, but how well the underlying processes are represented by LSM remains uncertain. In order to identify such missing or poorly represented processes in LSM, there is a strong need to bridge the gap between the contrasting scales of model resolution and in-situ measurements (Williams et al., 2009). This chapter will contribute to this research effort by addressing the following research questions:

How well is LSA simulated by global climate models? Are radiative regimes implemented in such frameworks capable of representing measured spatial and temporal variability in LSA?

To answer these questions, the global-scale modelling algorithms of CLM5 were applied to the point scale by running CLM5 in point mode (PTCLM) as a single grid-cell, forced by hourly meteorological driving data and point-specific canopy descriptors. CLM5 simulations of LSA are then evaluated spatially and temporally as a function of solar angle and canopy structure by comparing model output to spatially and temporally distributed UAV-borne observations of LSA, as introduced in Section 3.1.2 and analysed in Chapter 5, further assessing the robustness of the current CLM5 radiative transfer schemes.

This chapter is currently under review as "*Effect of forest canopy structure on wintertime Land Surface Albedo: Evaluating CLM5 simulations with in-situ measurements*" in Journal of Geophysical Research: Atmospheres.

6.1 Methods

6.1.1 Site Description and data collection

Field experiments for this study were conducted in both sub-alpine (Swiss Alps) and boreal (Finnish Lapland) forest environments, hence covering two different climatic conditions. For this part of the study, the spruce site in Davos Laret, Switzerland and the pine site in Sodankylä (expanded upon in detail in Section 3.2) were used for measurements and corresponding model experiments. At each site, the DJI S1000 octocopter equipped with up- and down-looking Kipp and Zonen CMP3 shortwave radiation sensors was used (see Section 3.1.2) to measure spatially and temporally distributed LSA. These UAV-borne measurements of LSA were used to assess CLM5 model performance at the process level.

6.1.2 CLM5 model setup

CLM5, the land component of CESM 2.0, has a built-in feature (PTCLM5) whereby the land model can be scaled down and simulations ran at point mode. Firstly, field site specific surface datasets describing the surface characteristics needed by CLM5 have to be generated. Parameters in these surface datasets include soil color, soil texture, fraction of the grid cell covered by different land-unit types and fraction for different vegetation types, and are derived from CLM5 global grid datasets and raw data files at 0.5° resolution. In the following, PTCLM5 simulations will be referred to as CLM5 simulations.

For this study, each CLM5 simulation corresponds to a WP of a UAV flight path. These point-mode CLM5 simulations of snow pack mass and energy fluxes were run at 21 WPs, nine at the sub-alpine spruce site (Laret, CH) and twelve at the boreal pine site (Sodankylä, FIN), using site-specific meteorological forcing and waypoint-specific forest canopy data. While the two sites contained different tree species (spruce, pine), they were both classified by CLM5 as the PFT Needle-leaf Evergreen Trees (NET). Hence, each CLM5 run was set up to simulate a grid cell being fully (100%) covered by NET of variable densities. Meteorological driving data (incident short and longwave radiation, air temperature, relative humidity, wind speed, pressure and precipitation) at 1-hour temporal resolution was derived from automatic weather stations (AWS) in unforested, open locations within

1 km of each forest site (see Section 3.1.3). CLM5 simulations ran between January 2017 - August 2018 at Laret and between January 2018 - August 2019 at Sodankylä to coincide with evaluation data while also allowing one year of spin-up. A spin-up was necessary to ensure soil moisture and soil temperature were in equilibrium and not affecting temporal dynamics and physical properties of the simulated snow cover evolution.

In CLM5, vegetation structure for each PFT is described by monthly varying Leaf Area Index (LAI) and Stem Area Index (SAI), as well as heights of canopy top and bottom. The percentage PFT occupying a particular cell, monthly LAI and SAI are derived from MODIS satellite data (Lawrence and Chase, 2007). The combination of LAI and SAI results in the Plant Area Index (PAI). For CLM5 simulations in point-mode, however, these canopy descriptors were calculated from a combination of above-mentioned terrestrial LiDAR data (boreal sites; canopy heights), airborne LiDAR data (sub-alpine sites; canopy heights) and hemispherical photography (all sites; PAIs).

In-situ up-looking hemispherical images were taken at all 9 WPs in Laret and at 6 out of the 10 in Sodankylä, while at the remaining 4 boreal sites synthetic hemispherical images were generated from terrestrial LiDAR data following Webster et al. (2020). Hemispherical images were first binarized into tree and sky, using a threshold algorithm provided by the model HPEval (Jonas et al., 2020). PAI was then calculated using the image analysis software 'Hemisfer' (Schleppi et al., 2007) based on an algorithm introduced by Miller (1967). PAI was split into LAI and SAI by applying the proportions given in the 0.25° MODIS-derived LAI and SAI standard CLM5 input dataset (0.28 for Sodankylä, 0.33 for Laret).

In addition, synthetic experiments were set up for both Sodankylä and Laret: PAI was varied from 0 to 5 at 0.1 increments, while the meteorological and remaining point-specific canopy data remained the same. This allowed us to specifically investigate the sensitivity of simulated LSA to PAI.

6.1.3 Snow undercatch

Precipitation intensity and amount often show high small-scale variability. Furthermore, the trajectory of a snow flake is easily affected by wind speeds, resulting in solid precipitation being generally underestimated by precipitation gauges (e.g. Fassnacht, 2004). For the model experiments of this thesis, it was important to estimate this degree of snow undercatch at each site. Analysis of snow depth measurements at the AWS in Laret and Sodankylä in combination with CLM5 simulations at unforested open sites adjacent to forest measurement locations allowed to account for this gauge undercatch of measured

precipitation. Snow undercatch factors for solid precipitation were determined as 1.3 and 1.5 for Laret and Sodankylä respectively, both sites featuring unshielded gauges.

6.1.4 Model adaptations

Before CLM5 could be taken forward to address the research objectives a number of adjustments were made to the model to ensure melt-out occurred at the correct time so that simulated LSA could be faithfully compared to observed LSA.

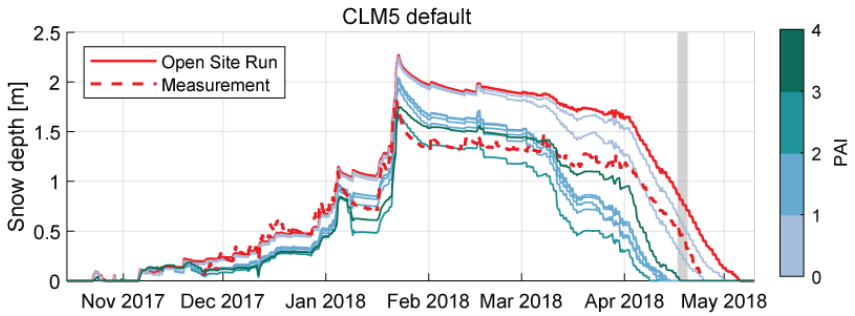

Figure 6.1: Simulated snow depth evolution for Davos Laret featuring default CLM5 model runs. Grey background indicates time period of intensive observation campaign, where full snow cover was observed at all waypoint locations.

Initial simulations at all forested sites showed that snow melted too quickly across all PAI when compared to observations (Figure 6.1). In order to obtain realistic snow depth and LSA simulation output at both open and forested areas, modifications of the CLM5 model code itself were necessary. Adaptations were made in three different areas: the turbulent transfer through the forest canopy, the snow covered area shape function, and the fraction of the canopy that is snow covered following interception events. Table 6.1 summarizes all model adaptions, the entirety of which led to realistic snow pack developments at all waypoint locations. In the following sections, all model adaptions are expanded upon in detail.

Turbulent transfer

The main issue which lead to exaggerated melt at forested sites was attributed to an overstated sensible heat exchange between the canopy air space and the snow surface, with up to 700 W m^{-2} of sensible heat flux going into the snow pack. This was mitigated by reducing the thermal resistance of the forest canopy as well as the wind speed within the canopy, each by a factor of 10. This adaption is a first order correction, which allowed CLM5 to be used for the purposes of this study. In CLM5, the unitless turbulent transfer coefficient for less-than-dense canopy ($csoil_{cn}$) is a function of the turbulent transfer

Table 6.1: CLM5 model setup and adaptions compared to the CLM5 default version.

Parameter description	CLM5 default	CLM5 modified
Sub-canopy wind speed (uaf)	$u_m \cdot \sqrt{\frac{1}{ram \cdot u_m}}$	$u_m \cdot \sqrt{\frac{1}{ram \cdot u_m}} \cdot \frac{1}{10}$
Turbulent transfer coeff. for less than dense canopy (csoil_{cn})	$csoil_b \cdot w + csoil_c \cdot (1-w)$	$\frac{csoil_b \cdot w + csoil_c \cdot (1-w)}{10}$
Snow-covered area shape function(n_{melt})	$\frac{200}{\sigma_{topo}}$	$\frac{200}{25}$
Fraction of canopy that is snow-covered (fcansno)	$\frac{snocan}{6 \cdot PAI} 0.15$	$\frac{snocan}{6 \cdot PAI}$

coefficient for soil under canopy ($csoil_c$), the turbulent transfer coefficient over bare soil ($csoil_b$), and canopy density (w). It is calculated by:

$$csoil_{cn} = csoil_b \cdot w + csoil_c \cdot (1-w) \tag{6.1}$$

$csoil_c$ [-] is set to 0.004, and $csoil_b$ [-] is parametrized based on the roughness length of the ground (z0) and the sub-canopy wind speed as:

$$csoil_b = \frac{0.4}{0.13(\frac{z0 \cdot uaf}{1.5E-5})^{0.45}} \tag{6.2}$$

Adjusting the turbulent transfer coefficient was not sufficient. In addition, the wind speed within the canopy (uaf) had to be decreased by a factor of 10. In CLM5, uaf is calculated as a function of wind speed at an open area (u_m, m s^{-1}), incorporating the stability effect, and aerodynamical resistance (ram):

$$uaf = u_m \cdot \sqrt{\frac{1}{ram \cdot u_m}} \tag{6.3}$$

where aerodynamical resistance is a function of friction velocity (u^* [m s^{-1}]):

$$ram = \frac{1}{u^* \cdot \frac{u^*}{u_m}} \tag{6.4}$$

Simply dividing uaf by a factor of 10 is quite a crude correction, which indirectly also affected the turbulent transfer coefficient csoil_{cn}. However, turbulent transfer through forest canopies is a major source of uncertainty (Link and Marks, 1999), and parametrizations tend to not be based on observations, as they are very difficult to obtain. This adaption should be viewed as a necessary tuning exercise for this specific study. There is, however, a

need to improve turbulent heat transfer parametrizations of forested environments, which will require attention in the future.

Snow-covered area shape function

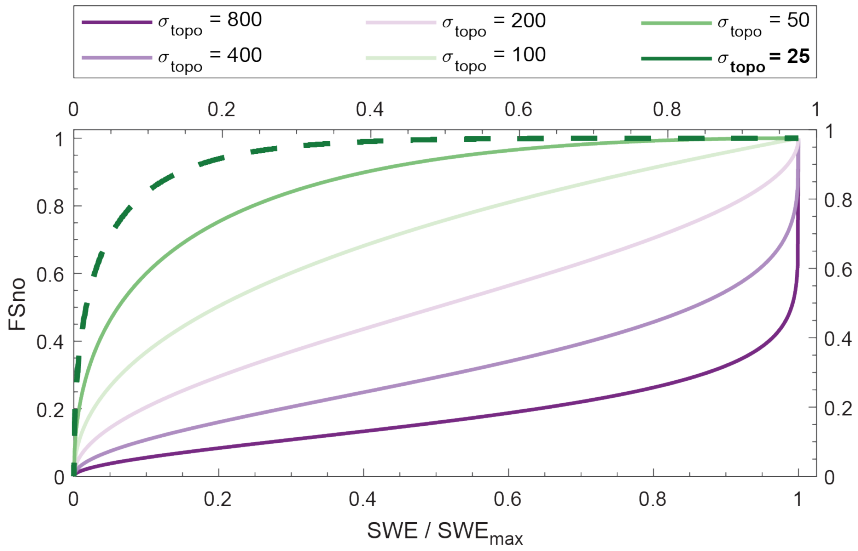

Figure 6.2: Fractional snow cover vs. dimensionless SWE during melt period for grid cells with varying standard deviation of topography (σ_{topo}) as calculated by Equation (6.5). Figure adapted from Swenson and Lawrence (2012). The green dashed line was used for this study.

The majority of model evaluation data was collected in the spring, right before and during the snow melt period, further requiring to match melt out patterns of observations and model simulations. Fractional snow-covered area (FSno) in CLM5 is calculated following Swenson and Lawrence (2012):

$$FSno = 1 - [\frac{1}{\pi} acos(2\frac{W}{W_{max}} - 1)]^{n_{melt}} \tag{6.5}$$

W is the simulated snow water equivalent (SWE) at the current time step and W_{max} is the maximum simulated SWE of the snow season. n_{melt} is the snow covered area shape function, which is determined from σ_{topo}, the standard deviation of topography within a grid cell by:

$$n_{melt} = \frac{200}{\sigma_{topo}} \tag{6.6}$$

For point-scale simulations, σ_{topo} was difficult to quantify. A top down approach was taken, by calculating FSno for a range of σ_{topo} and investigating which solution best matches observations at the field sites. Figure 6.2 shows calculated FSno for a range of σ_{topo} for the entire range of SWE. In accordance with observations, a low σ_{topo} was chosen (green dashed line in Figure 6.2), which delayed the onset of fractional snow cover and showed a rapid decline in snow cover extent towards the end of the melt season.

Fraction of canopy that is snow-covered

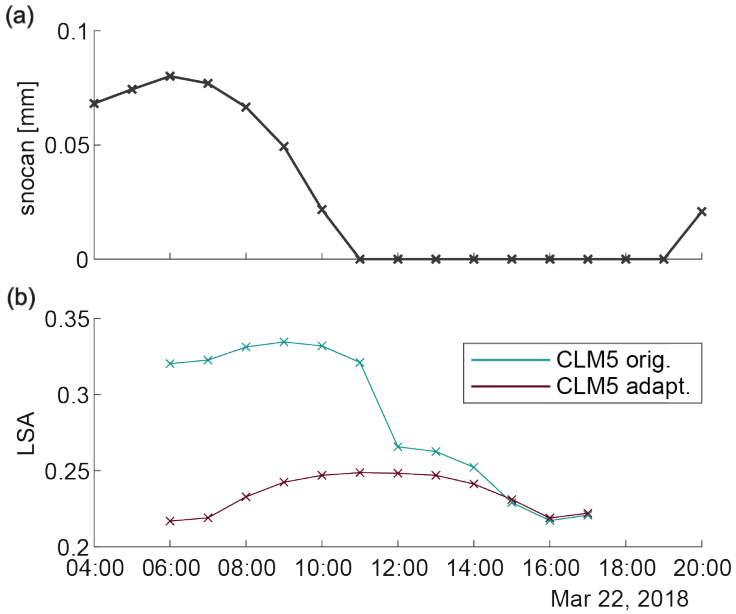

Figure 6.3: Intercepted snow (a) and the coinciding LSA (b) computed with the original and the adapted CLM5 model version for an exemplary clear sky day (22.3.2018) with no precedent snow fall event at a sparse forest canopy (PAI=1) site in Davos Laret.

The fraction of canopy that is snow-covered (fcansno) has substantial effects on LSA, however, in the CLM5 default model version LSA was unrealistically responsive to even tiny amounts of snow in the canopy. In the default CLM5 version, fcanso is based on the amount of intercepted snow in the canopy (snocan in mm H_2O, Figure 6.3), forest density (PAI), the maximum allowed dew (dewmx) and a parameter called "fraction of vegetation that is not covered by snow" ($fveg_{nosno}$):

$$.fcansno_{orig} = (\frac{dewmxi}{vegt \cdot 6 \cdot 10} \cdot snocan)^{0.15} = (\frac{snocan}{6 \cdot PAI})^{0.15} \tag{6.7}$$

$$vegt = fveg_{nosno} \cdot PAI \tag{6.8}$$

$$dewmxi = \frac{1}{dewmx} = \frac{1}{0.1} \tag{6.9}$$

The problem that arises from this parametrization, is that $fveg_{nosno}$ is a logical operator that can only be set to 0 or to 1. Hence, if even the smallest amount of dew is formed over night, it is already noticeable in the simulated LSA for the majority of the next day. Furthermore, it can be seen that the maximum amount of intercepted snow that can be held by a canopy is limited to $6 * PAI$, and because in the original parametrization snocan as a fraction of $snocan_{max}$ is taken to the power of 0.15, even smallest amounts of snocan result in relatively high values of $fcansno$ (e.g. 0.05 of $snocan_{max}$ will result in a $fcansno$ of 0.64, leading to an unrealistically high LSA). This problem was mitigated

by removing the power of 0.15, and omitting $fveg_{nosno}$ altogether, as $fcansno$ is only calculated if *snocan* is larger than 0. Results of implementing this adaption is shown in Figure 6.3. Figure 6.3 (a) shows the amount of intercepted snow modelled by CLM5 for an exemplary clear sky day with no precedent snow fall event at a sparse forest stand ($PAI = 1$). Figure 6.3 (b) shows the same day and forest stand, but contrasts the difference in simulated LSA between the original and the adapted CLM5 model version.

Collective effects

In order to visualize the collective effects of the CLM5 model adaptions, Figure 6.4 shows differences in snow pack evolution between CLM5 default and CLM5 adapted model runs for all WPs at the Davos Laret site. The CLM5 adapted runs showed less difference in melt-out date between WPs of different PAIs. This was crucial, as an important part of the LSA measurements were taken on 18.04.2018 (highlighted by a grey background in Figure 6.4), under full-snow-cover conditions. Hence, the entirety of the discussed model adaptions, resulting in CLM5 adapted model runs, accurately represented full-snow-cover conditions for that day and further allowed us to compare and evaluate CLM5 simulations on 18.04.2018.

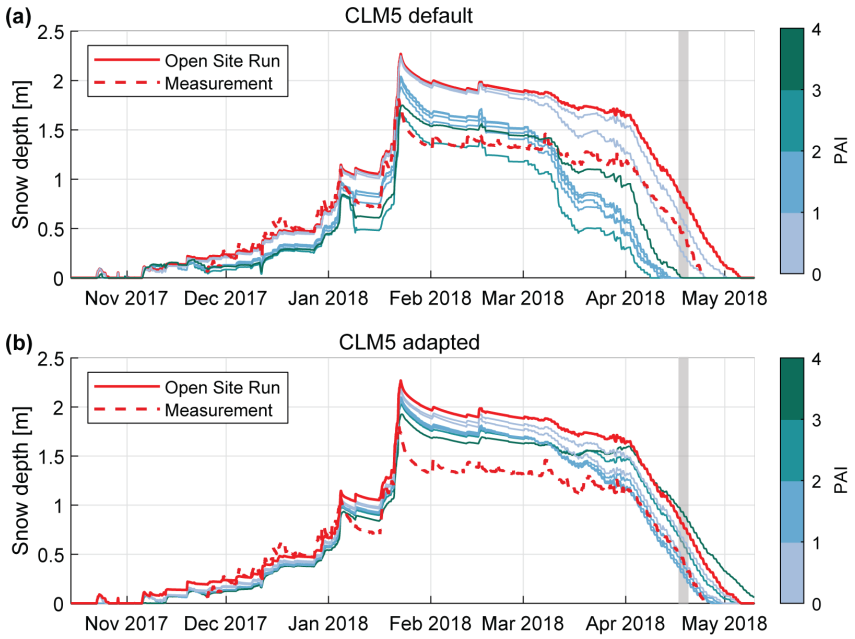

Figure 6.4: Simulated snow depth evolution for Davos Laret featuring a) default CLM5 and b) adapted CLM5 model runs. Grey background indicates time period of intensive observation campaign, where full snow cover was observed at all waypoint locations.

6.2 Results

The adapted CLM5 model version is now taken forward and driven by site-specific meteorological data and waypoint-specific descriptors of vegetation structure. The effects of (i) solar zenith angle (ii) solar azimuth angle and (iii) canopy and land surface descriptors and (iv) PAI are investigated. The simulated seasonal evolution of LSA is compared to measurements for a range of canopy covers. This facilitates the development of a first-order correction, further referred to as effective PAI correction, which was applied to CLM5 in order to replicate measured LSA.

6.2.1 Effect of solar zenith angle

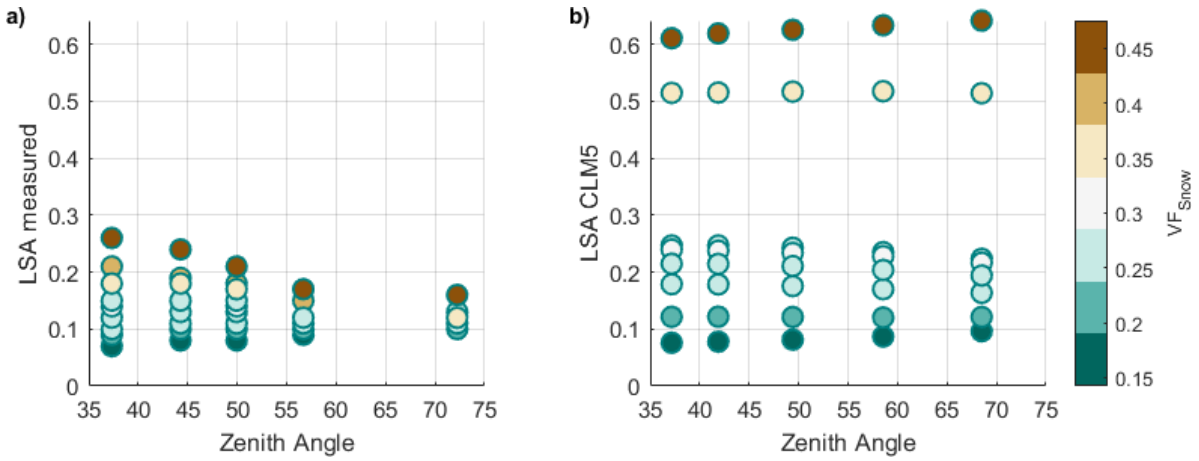

Figure 6.5: (a) Measurements of LSA and (b) CLM5 simulations of LSA at different zenith angles and snow view fractions for a single clear sky day (18.4.18) at the spruce site in Davos Laret, Switzerland. Note the difference in y-axis limits and the fact that light brown points in a) resulted in identical CLM5 simulation results and are hence overlapping in b).

Here data shown and discussed in Section 5.2.3 is built upon. Measurements originated from a series of flights at the spruce site in Davos Laret over the course of one day (Figure 6.5a), which revealed a strong effect of solar zenith angle on LSA. Depending on forest canopy sparsity, LSA was shown to either decrease or increase with increased solar zenith angle.

Corresponding CLM5 simulations (Figure 6.5b) show only a minimal response to diurnal changes of the zenith angle. Contrary to measurements, simulated LSA increases slightly with zenith angle even for very sparse points ($VF_{Snow} > 0.4$), but only by less than 5%. These small differences are a function of the interplay between forest floor snow albedo (dependent on grain size and the angle of incidence of the solar rays) and canopy radiative transfer calculations in CLM5. At WPs over denser canopy, CLM5 simulations replicate

magnitudes of measured LSA fairly well. Most notably, however, CLM5 simulations feature a large positive bias of up to 40% in LSA estimates for sparse canopy.

6.2.2 Effect of solar azimuth angle

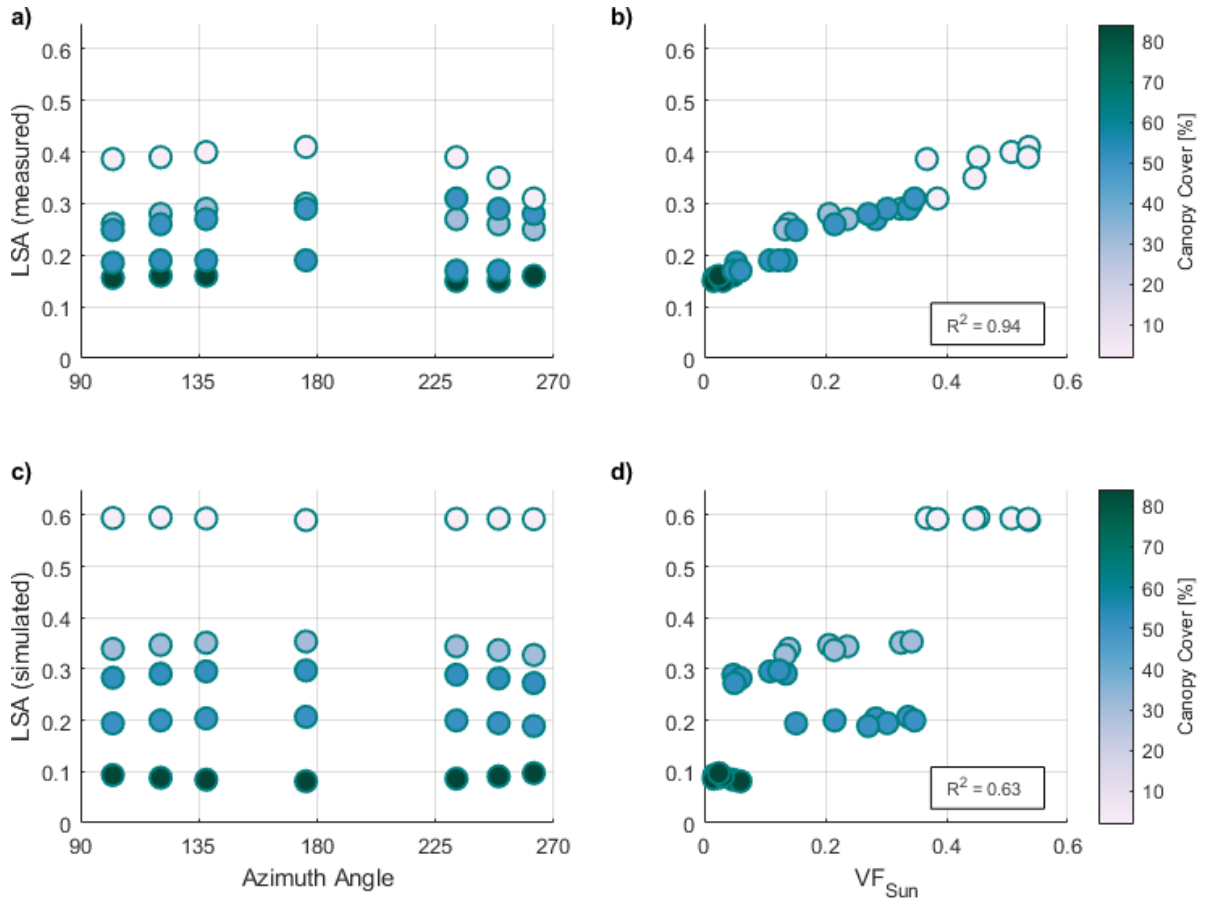

Figure 6.6: On 26 April 2019 at the boreal pine site (Sodankylä), (a) variability in measured LSA as a function of azimuth angle, and (b) in comparison to VF_{Sun}. Figures (c) and (d) replicate (a) and (b) with LSA simulated using CLM5. Color represents canopy coverage of individual WPs derived from CHMs.

In addition to zenith angle, the azimuth can also be important for LSA, as it controls the orientation of shadows on the snow surface. Again, the illustrative example shown in Section 5.2.3 from the boreal pine site in Sodankylä (Figure 6.6), which highlights the effects of azimuth angle on LSA, is built upon.

CLM5 simulations show only a minimal variation of the simulated LSA with azimuth angle (Figure 6.6c) and the measured decrease in LSA at WPs with sparse canopy during the second half of the solar cycle is not represented in the CLM5 output. CLM5 does not consider the azimuth angle, so any corresponding variation of LSA is of indirect nature only. Figure 6.6d further shows a strong response of simulated LSA to VF_{Sun} ($\mathrm{R}^2 = 0.63$),

however, only between WPs but not within each WP. Consistent with results for this site and day, simulated LSAs for sparse canopies were consistently overestimated, with a high bias of up to 20%.

6.2.3 Seasonal LSA evolution

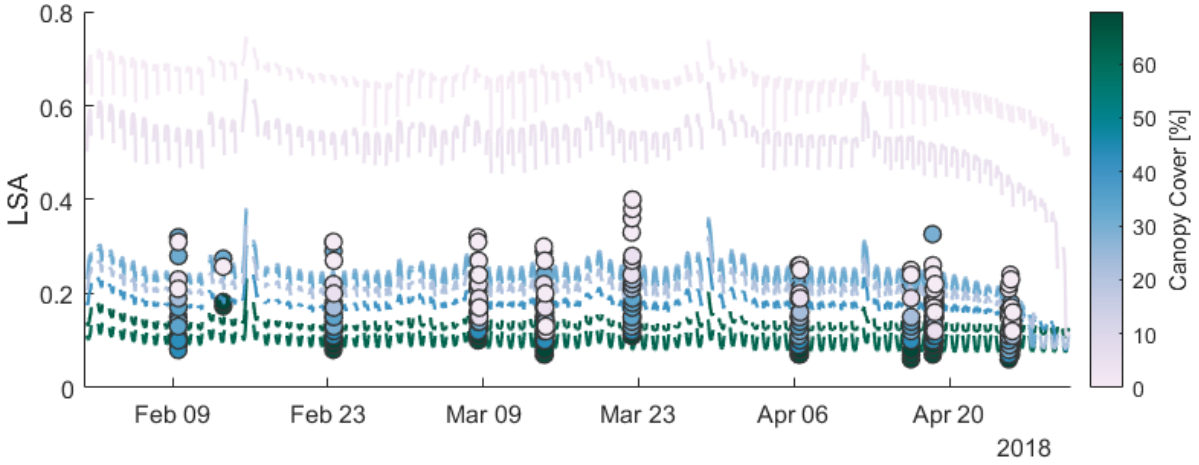

Figure 6.7: Seasonal development of LSA at each WP at the spruce site in Davos Laret, Switzerland. Solid lines are CLM5 simulations for different forest canopy coverage. Circles indicate UAV measurements of LSA at waypoints with different canopy cover. Data gaps correspond to night time periods.

Compared to all measurements taken in clear sky conditions between February and May 2018 at the spruce site in Davos Laret, CLM5 both over- and underestimated LSA. LSA in very sparse environments (CC $<$ 20%) was overestimated between 26-66%, while LSA was both under- and overestimated in dense canopies (CC $>$ 50%). Specifically, compared to the individual measurements throughout the season at both dense and sparse WPs, CLM5 simulations overestimated LSA by 0.5-66% at 67% of the cases and underestimated LSA by 1-12% in the remaining 33%. Underestimation of LSA predominantly occurred during low zenith angles around solar noon. Forest floor snow albedo also modulates overall LSA, and it is at the very sparse areas where it has the strongest effects. In most cases, however, the effect of the forest canopy prevails.

A clear response to interception events can be noted when spikes in simulated LSA coincide with snowfall events and resulting in snow added to the canopy. Furthermore, during mid-April, simulated LSA strongly declines responding to melt-out of snow on the ground, especially in sparse canopies. Simulated LSA in Figure 6.7 also demonstrates that, as canopy coverage decreases from dense to sparse, the diurnal shape of simulated albedo changes from a parabola shape with the vertex at the lowest point to an upside-down parabola, with this transition occurring at approximately 30% canopy coverage.

6.2.4 Effect of canopy and land surface descriptors

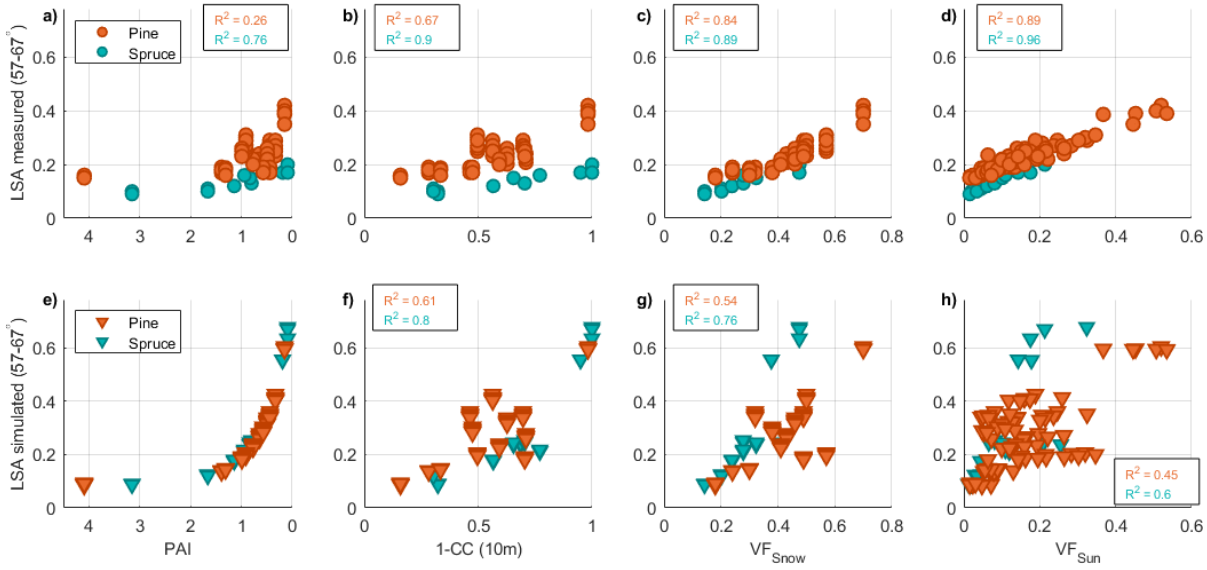

Figure 6.8: LSA compared to four different canopy and land surface descriptors for the pine (FIN) and spruce (CH) field sites: a-d show UAV-based measurements of LSA while e-h visualize CLM5 model output of LSA. The complexity of the parameter describing the forest canopy increases from left to right.

Measured LSA is strongly correlated to shadows cast by trees, which is a function of the position of the sun relative to the structure of the canopy surrounding each WP. In an attempt to isolate the relationship between LSA and various canopy descriptors from the effect of the moving sun, the following data analysis was limited to data from a confined range of zenith angles (57-67°), which was chosen to include the maximum amount of measurements at both the pine site in Sodankylä and the spruce site in Davos Laret. Figure 6.8 shows the correlation between either measured or simulated LSA and four different metrics that relate to canopy structure and radiation transfer (PAI, 1-CC, VF_{Snow}, VF_{Sun}). While CLM5 is built around a radiation transfer model that emphasizes an exponential relationship between LSA and PAI, measurements show comparatively little correlation between those variables. On the contrary, measurements suggest a strong correspondence between LSA and VF_{Sun}, a relationship that is currently unaccounted for in CLM5. Correlations for 1-CC and VF_{Snow} constitute a transition between the above extreme cases. The four descriptors represent a sequence of canopy metrics increasing in complexity from spatially generalized (PAI), to local environment (CC), to specifically accounting for the spatial arrangement of surrounding canopy elements independent of the position of the sun (VF_{Snow}), or in direct relation to the position of the sun (VF_{Sun}). Along this transition, correlation to LSA increases for observational data (Figure 6.8a-d), but decreases for CLM5 simulations (Figure 6.8e-h).

6.2.5 LSA sensitivity to PAI

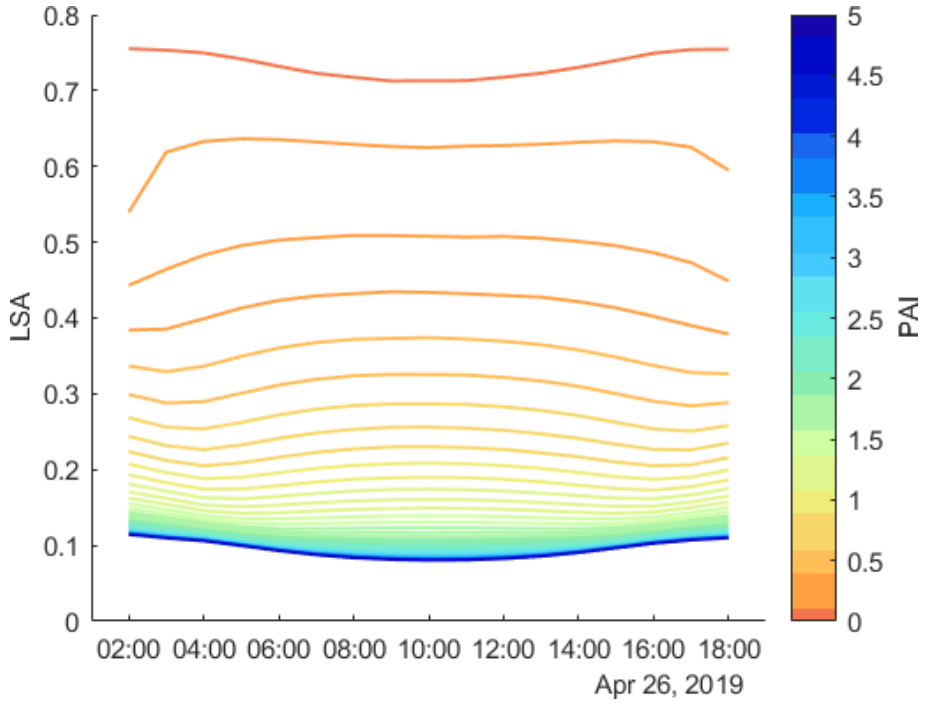

Figure 6.9: Simulated LSA (lines) as a function of PAI (0 <= PAI <= 5) for a clear sky day (26.4.2019) at the pine site in Sodankylä.

Data from WPs over sparse canopy environments have demonstrated considerable overestimation of CLM5 simulated LSA. In an attempt to explain the high bias, a sensitivity analysis is performed, which is based on the CLM5 LSA simulations with synthetically varying PAI, whose values were selected to lie between 0 and 5 at 0.1 increments. Focusing on one clear sky day in Sodankylä (26.04.2019), Figure 6.9 highlights that most of the reduction in simulated LSA with an increasing PAI happens between PAI 0 and PAI 1 (approximately 60%) while simulated LSA only decays marginally with PAI when PAI exceeds 2.

6.2.6 Effective PAI values

The systematic high biases in CLM5 compared to measurements suggest that the exponential relationship between LSA and PAI (Figure 6.8e) may exaggerate LSA increases with decreasing canopy density (Figure 6.9). This has raised the question, what effective PAI values would be needed in the radiation transfer equations to replicate measured LSA? To this end, an optimal PAI for each WP location was derived individually ("best fit PAI") by minimizing the error of each WP simulation. Best fit PAI values were mostly higher than those estimated from point specific hemispherical images, particularly for the spruce site. A logarithmic function was further fitted to those best fit PAI values, whereby each

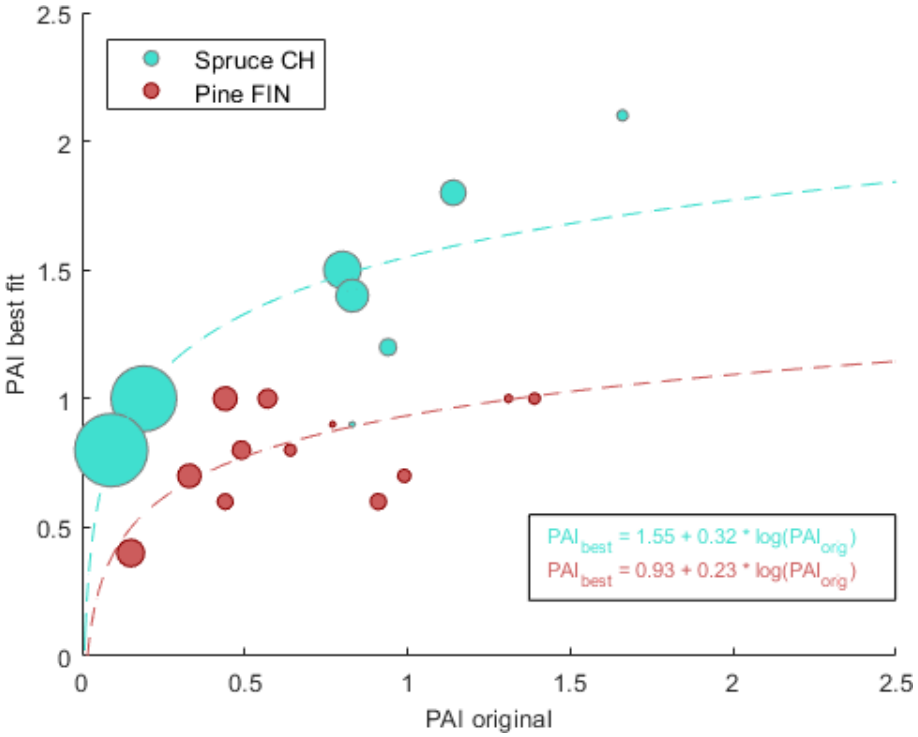

Figure 6.10: Original PAI of WPs derived from hemispherical photographs vs. the PAI which would result in the lowest difference between measured and simulated LSA ("best fit PAI"). Size of dots corresponds to the improvement of simulated LSA by using the "best fit PAI" across all measurement points.

data point was weighted dependent on the resulting improvement of simulated LSA when using the best fit PAI values. This approach provided a parametrization of effective PAI as a function of HP-derived PAI, the results of which are summarized in Figure 6.10. The shown best fit PAI equations were applied to compute effective PAIs at each WP location, which were subsequently used to re-run CLM5 simulations. CLM5 LSA simulations using these effective PAIs showed a substantial improvement for both the spruce (Figure 6.11a-b, 76% RMSE reduction) and the pine site (Figure 6.11c-d, 64% RMSE reduction).

6.3 Discussion

Assessment of LSM performance is complicated due to the often contrasting spatial scales of model resolution and in-situ measurements as well as the concurrence of parametric and structural uncertainties in modelling frameworks (Keenan et al., 2011). In this study, the combination of spatiotemporal LSA measurements with corresponding CLM5 simulations allowed identification of deficiencies in model process representation, e.g. canopy structural shading of the snow surface. UAV measurements showed both zenith and azimuth angles control diurnal variability of LSA. However, corresponding CLM5 simulations were not

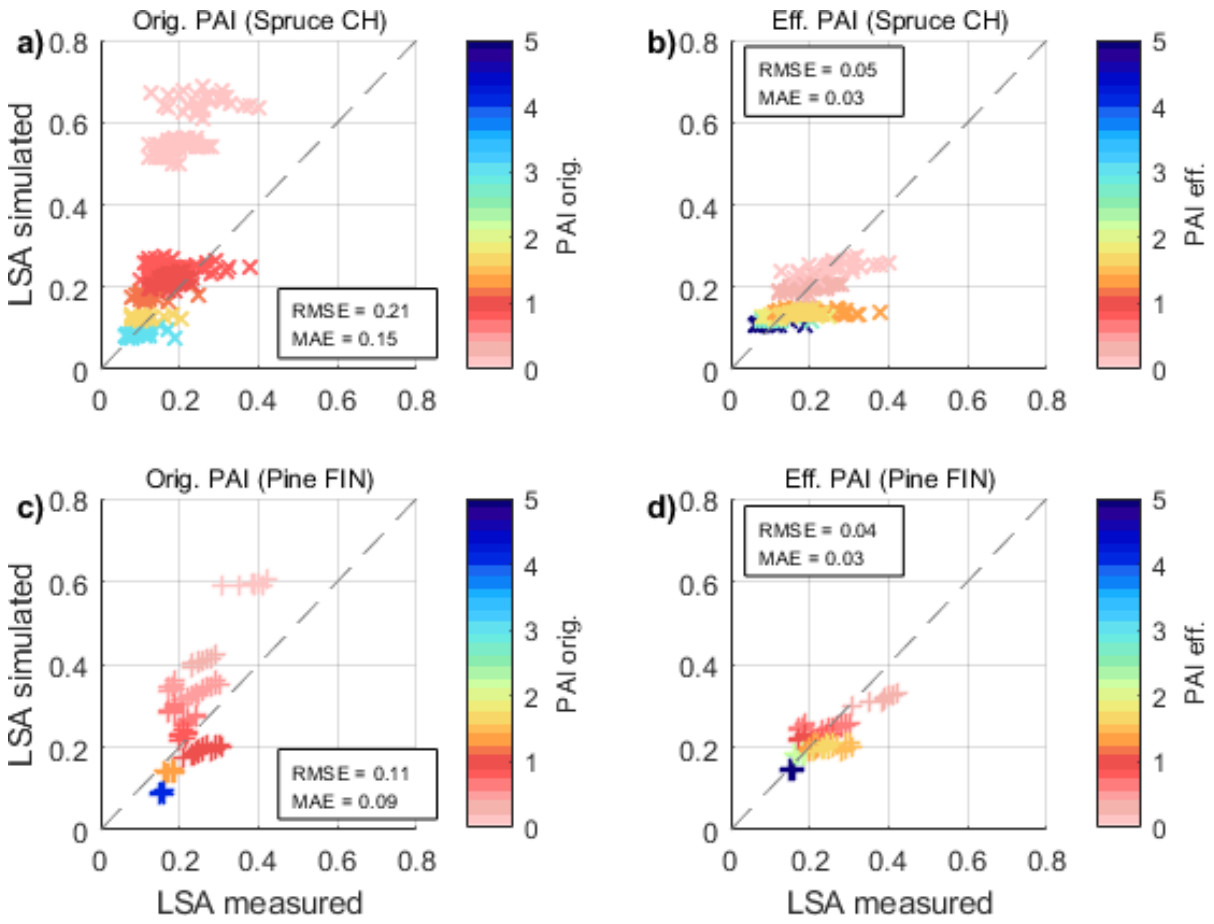

Figure 6.11: Measured vs. simulated LSA for simulations run with original PAI (a,c) and with effective PAIs following the equations in Figure 6.10, for both the spruce (a,b) and the pine (c,d) site.

able to replicate the observed diurnal or spatial variability in LSA. The two stream approximation used in CLM5 (Sellers, 1985) only takes zenith angle into account, which changes simulated LSA by marginal amounts in early mornings and late afternoons. Largest discrepancies between simulations and measurements of LSA were identified in sparse forest environments, consistent with Yuan et al. (2017), who found the two stream approximation performed best in dense forests with limited spatial heterogeneity. Gaps and edges, predominant in sparse forest environments, increase the potential for direct insolation of the snow surface and result in LSA which are highly variable in space and time. It is in these environments where CLM5 simulations showed most substantial deficiencies, and failed to replicate the measured diurnal and spatial variability in LSA.

CLM5 uses the big leaf approach which simplifies the canopy structure into a homogeneous layer of absorbent matter. Moreover, absorption is parameterized as a function of PAI, which is a spatially integrated metric that neglects any structural heterogeneity within the canopy of interest. In consequence, CLM5 is unable to reflect the complex interplay between solar position and gaps in the surrounding canopy as evidenced by sub-canopy

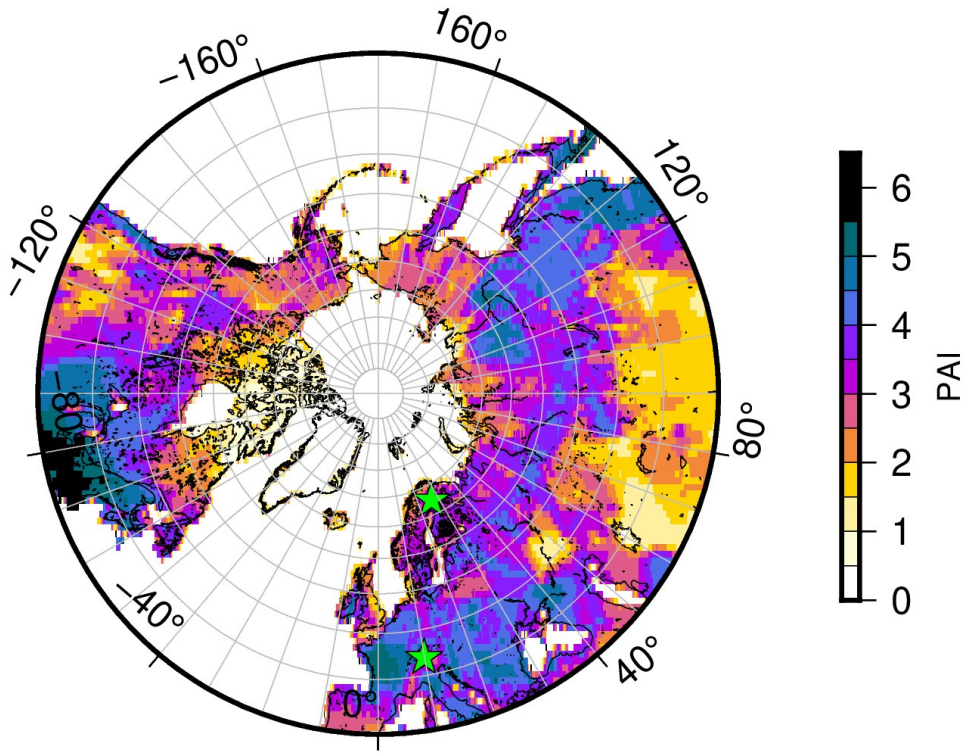

Figure 6.12: PAI magnitudes across the northern hemisphere extra-tropics derived from the 0.25 degree input surface dataset of CLM5. Locations of measurement sites in Laret, CH and Sodankylä, FIN are indicated by green stars.

radiation measurements (Malle et al., 2019, Mazzotti et al., 2019), which in turn influence LSA. The particularly striking biases for sparse canopies suggest that CLM5 not only over-represents the penetration of direct light through sparse canopy, but further does not account for the spatial and temporal heterogeneity in canopy snow surface shading. Simulations further showed how in sparse forest environments even small changes in PAI can have large effects on simulated LSA. This is in line with findings by Manninen and Jääskeläinen (2018), who albeit only looking at diffuse radiation, found that CLM4 LSA decays more steeply with increasing PAI compared to two other albedo schemes, the Canadian Land Surface Scheme (Verseghy et al., 1993) and the forest reflectance model PARAS (Rautiainen and Stenberg, 2005). Wang, Cole, Bartlett, Verseghy, Derksen, Brown, Von Salzen and Salzen (2016) also found that most of the LSA reduction in CLM4 happens as PAI is increased from 0 to 1, and that a LSA saturation occurs for PAI values exceeding 3. Furthermore, Wang, Cole, Bartlett, Verseghy, Derksen, Brown, Von Salzen and Salzen (2016) demonstrated that LSA in CLM4 is more sensitive to a PAI-induced bias in the visible compared to the near-infrared wavelengths, as greater disparities between snow and forests emerge in the visible wavelengths.

The global dataset of wintertime NET PAI (MODIS-derived, 0.25°) commonly used in CLM5 simulations (Figure 6.12), shows that sparse forest canopies (PAI < 2) are

found in approximately 8% of the NET covered pixels. These pixels are mostly located around the circumpolar taiga to tundra transition, an area particularly sensitive to climate change (Serreze et al., 2000, Swann et al., 2010). Dense forest canopies (PAI $>$ 2), on the other hand, account for approximately 92% of the NET area. Hence, across the northern hemisphere, differences in simulated LSA resulting from differences in canopy density are limited, as model sensitivity experiments showed that simulated LSA was relatively insensitive to increasing PAI values above 2, which is in stark contrast to what measurements suggested. This problem was partly mitigated by using effective PAI values. Effective PAIs could be a first step to remove the overall bias in LSA for sparse canopies without the need of structural changes to the radiation transfer scheme built into CLM5. However, such an approach would not help to fix the limited diurnal variation of simulated LSA, which would necessitate a more detailed representation of radiation transfer through canopy gaps.

Investigation into the relationship between model error and land surface descriptors showed that VF_{Sun} has the best correlation with measured LSA. While VF_{Sun} can be straightforward to measure in this instance, incorporating this variable into LSM would be much more challenging. In recent years, airborne LiDAR data has become a valuable source of detailed canopy structure information, which has motivated the development of models that can characterize radiation transfer through forest canopy at much greater detail (Musselman et al., 2013, Zellweger et al., 2019, Jonas et al., 2020). Recent efforts have resulted in methods that are efficient enough to resolve insolation patterns down to meter resolution even over fairly large areas ($\sim$ 1km2, Webster et al. (2020)).

The benefit of such a detailed representation of radiative transfer processes within a snow model was first demonstrated by Musselman et al. (2012). Currently, there are at least two forest snow models capable of fully-distributed simulations at very high spatial resolution, that include similarly detailed radiation transfer models and reproduce observed snow accumulation and melt dynamics more accurate than conventional models (Broxton et al., 2015, Mazzotti, Essery, Webster, Malle and Jonas, 2020). While these approaches may be too computationally expensive for inclusion in LSM intended for hemisphere-scale applications, they demonstrate the increasing potential for spatially distributed radiation transfer schemes capable of explicitly resolving radiation transfer through canopy gaps. In coarse scale LSM like CLM5, structural heterogeneity needs to be better described in order to explicitly account for diurnal variability of LSA. Inclusion of a metric which accounts for canopy structure in 2D, combined with a radiative transfer approach that allows for temporal interaction between solar position and such 2D canopy structures is proposed as a result of this study. Such an approach would allow the temporal variability

of canopy shading of the snow surface to be more explicitly represented, and should be a focus in the development of the next generation of LSM.

6.4 Chapter Summary

In this chapter, the previously presented airborne LSA measurements using an UAV co-registered to canopy structure and snow surface shading information (see Chapter 5) were used to evaluate the performance of the radiative transfer scheme implemented in the Community Land Model 5.0 (CLM5) over seasonally snow-covered forest stands in boreal and sub-alpine environments from a LSA perspective. Simulations did not adequately capture the measured spatial and temporal variability in LSA. This is partly due to the generalized canopy structure in the radiative transfer scheme, which over-simplifies the interaction between solar position and canopy heterogeneity. Additional errors then resulted in the amount of solar radiation incident at the snow surface, particularly in sparse forest environments. Analysis of diurnal patterns of measured LSA further revealed strong effects of both azimuth and zenith angles on LSA, which were not replicated by CLM5 simulations. Decay in simulated LSA with increasing Plant Area Index (PAI, the main canopy descriptor in CLM5) between 0 and 2 was too rapid. As simulations further showed strong overestimations of LSA in sparse forest environments, the use of effective PAI values as a simple first-order correction for this discrepancy is proposed. However, more complex canopy descriptors are needed which account for gaps and capture the structural heterogeneity of forest stands. Such model developments would help decrease uncertainty in LSA simulations across seasonally snow-covered forest environments, with profound implications for snow albedo feedbacks.

Chapter 7

Impacts of time-varying transmissivity on CLM5 simulations of sub-canopy shortwave radiation

Chapter 4 demonstrated sub-canopy incoming shortwave radiation to be highly variable in space and time. Subsequently, land surface albedo (LSA) was shown to be highly dependent on solar angle (see Chapter 5) and model experiments with the Community Land Model 5.0 (CLM5) revealed that CLM5 simulations did not adequately capture the measured spatial and temporal variability in LSA (Chapter 6). In this chapter, model evaluation efforts are expanded to sub-canopy incident shortwave radiation, as RQ2b is addressed:

Are radiative regimes implemented in LSM capable of representing measured spatial and temporal variability in sub-canopy incoming shortwave radiation?

Furthermore, potential avenues for future research are presented, as the importance of accounting for directionality of solar irradiance for simulation of sub-canopy incoming shortwave radiation is investigated and the impacts of integrating a time-varying transmissivity for direct shortwave radiation into the CLM5 radiation scheme are evaluated. The solar radiation algorithm HPEval from Jonas et al. (2020) is used to model sub-canopy direct and diffuse shortwave radiation along the cable car transect in Davos Laret (see Section 3.1.1 for a description of the applied measurement setup). This modelled sub-canopy shortwave radiation is used to force CLM5, bypassing the two-stream approximation, resulting in a model version herein referred to as *CLM5 modified*. Performance of the CLM5 default and CLM5 modified model versions are evaluated using independent cable car measurements of sub-canopy incoming shortwave radiation.

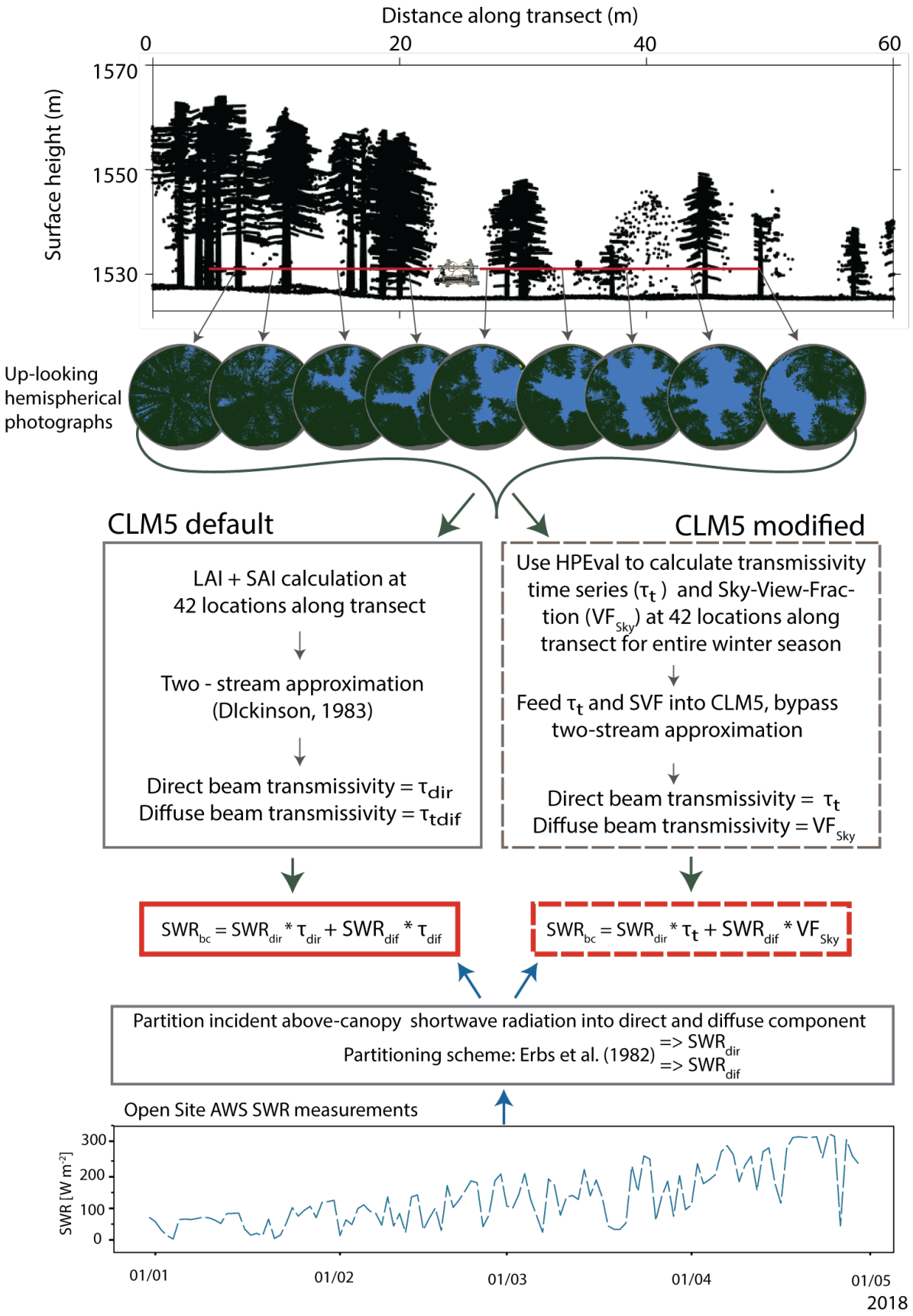

Figure 7.1: Overview of modelling strategies applied in this study: CLM5 default vs. CLM5 modified.

7.1 Methods

The CLM5 model configuration used in Chapter 6 is applied for point-simulations of both the CLM5 default and the CLM5 modified model experiments at forty-two locations along the 48m long cable car transect in Davos Laret (Switzerland). The only difference between the two CLM5 versions is the radiative transfer calculation (Figure 7.1). Both sets of experiments ran at an hourly temporal resolution between January 2017 - August 2018.

7.1.1 CLM5 default

The CLM5 default version uses the two-stream approximation, requiring Plant Area Index (PAI), Leaf Area Index (LAI) and Stem Area Index (SAI) as input parameters. These parameters were acquired using up-looking hemispherical images (Sony Alpha NEX6 camera) at the forty-two locations along the cable car transect, which were binarized into tree and sky using the image analysis software 'Hemisfer' (Schleppi et al., 2007) to allow calculation of PAI. Respective LAI and SAI were obtained using their respective proportions in the 0.25° MODIS-derived LAI and SAI standard CLM5 input dataset.

7.1.2 CLM5 modified

The CLM5 modified configuration is similar to the CLM5 default configuration, except the two-stream approximation is replaced by offline radiative transfer calculations. Figure 7.1 gives an overview of the applied modelling strategies. The forty-two hemispherical photographs taken along the cable car transect are used to parameterize HPEval (Jonas et al., 2020). HPEval calculates below forest radiation regimes at high temporal and spatial resolutions, providing estimates of sub-canopy incoming solar radiation. It accounts for terrain shading and solves for shortwave transmissivity at each of the forty-two points along the transect. Overall transmissivity (τ) is split into diffuse and direct components, where diffuse beam transmissivity is approximated by sky-view fraction (VF_{Sky}) and direct beam transmissivity, henceforth time-varying transmissivity (τ_t), is calculated as the fraction of the solar disk that is not obscured by the canopy or terrain. Transmissivities were calculated at a 2 minute temporal resolution, January 2017 through August 2018, and then aggregated to hourly resolution for forcing of CLM5. Computed HPEval transmissivities were assumed to be identical for NIR and visible wavelengths.

7.1.3 Sub-canopy radiation

Forest canopy transmissivities were applied to above canopy incoming shortwave radiation measurements to calculate sub-canopy incoming shortwave radiation. Open site shortwave radiation measurements were used as a proxy for above canopy measurements, which were partitioned into diffuse and direct components following Erbs et al. (1982). Calculated sub-canopy shortwave radiation was then evaluated based on spatiotemporal sub-canopy measurements of incident solar radiation, from the cable car system (Section 3.1.1). Cable car measurements were combined with open site AWS measurements in order to compute benchmark transmissivities of shortwave radiation.

7.2 Results

7.2.1 Measured transmissivities

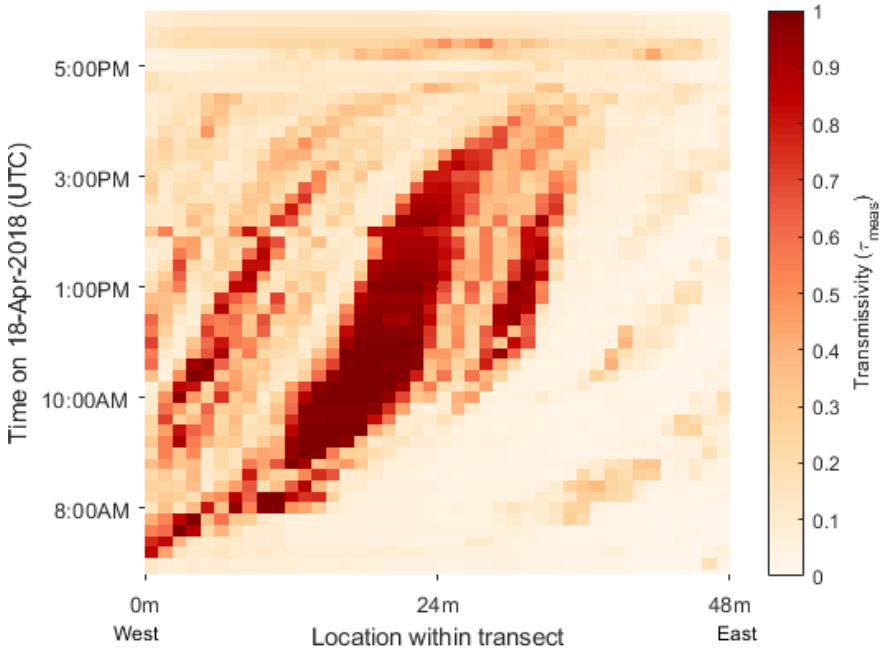

Figure 7.2: Measured transmissivity (τ_{meas}) along the cable car transect in Davos Laret for 18 April 2018 as calculated from cable car measurements along the transect and open site AWS measurements of SWR.

High transmissivity values were measured whenever the position of the sun combined with the overlying canopy structure allowed direct insolation of the ground surface (Figure 7.2). The transmissivity pattern mirrors that of sub-canopy incoming shortwave radiation (see Section 4.2.1), a diagonal pattern in the space-time domain resulting from high transmissivity values over the day tracking the sun path from East to West.

7.2.2 Modelled transmissivities

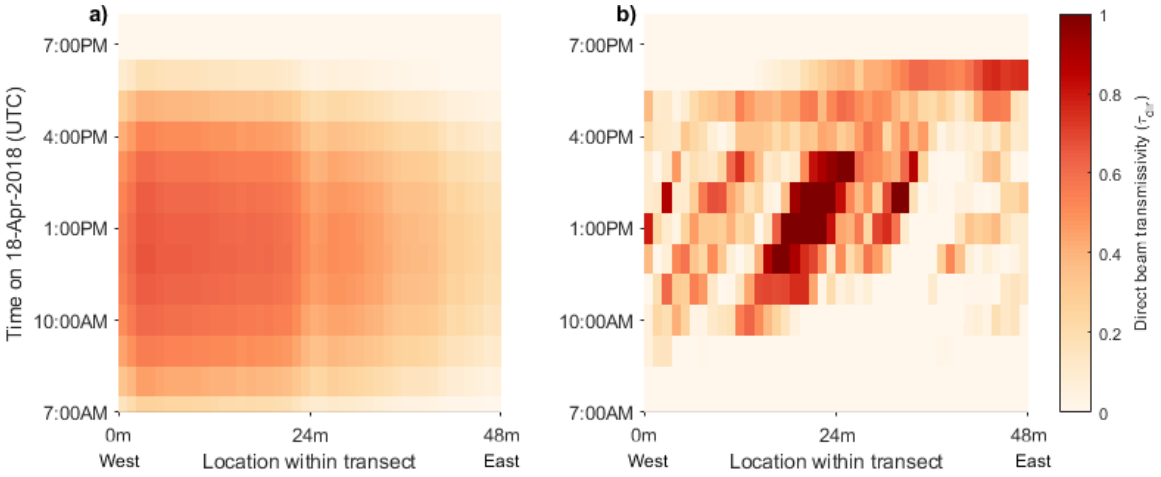

Figure 7.3: Direct beam transmissivity (τ_{dir}) along the cable car transect in Davos Laret for 18 April 2018 as simulated by a) default CLM5, using the two-stream approximation; b) modified CLM5, using the radiative transfer model HPEval.

CLM5 default simulations (Figure 7.3a) did not reproduce the observed spatio-temporal patterns of transmissivity (Figure 7.2), and showed minimal diurnal variability, due to the over-simplified geometrical representation of canopy elements. Discrepancies between measured and modelled transmissivities are particularly high in the middle of the transect, where the forest canopy was discontinuous and measurements showed large diurnal variabilities of solar transmission which were not replicated by the CLM5 default simulations.

Modified CLM5 simulations (Figure 7.3b) well reproduced measured transmissivities in the space-time domain. Differences were especially pronounced towards the east end of the transect at the end of the day, possibly emerging due to small camera alignment issues. Both CLM5 default and CLM5 modified runs were performed at one hour temporal resolution, which eventuated in coarser grid-cells, further explaining the visually noticeable coarseness in Figure 7.3 compared to the continuously taken cable car measurements shown in Figure 7.2.

7.2.3 Modelled vs. measured transmissivities

Difference between measured and modelled transect averaged sub-canopy shortwave radiation varied over the course of a clear-sky day. CLM5 default simulations overestimated sub-canopy incoming solar radiation by up to 130 W m^{-2} while CLM5 modified simulations represented measured solar transmission through the canopy well, both in location and magnitude. However, at around 17:00 hrs, CLM5 modified simulations briefly spike

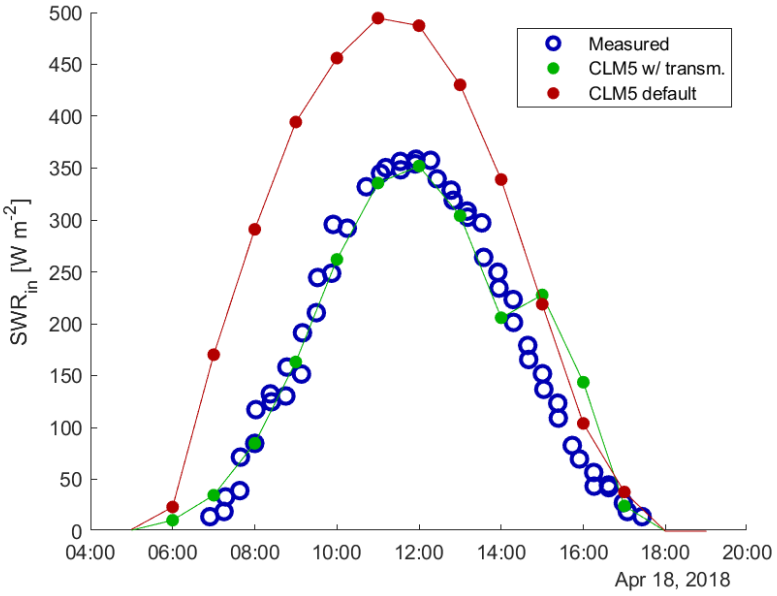

Figure 7.4: Temporal evolution of spatially averaged sub-canopy incoming shortwave radiation along the cable car transect in Davos Laret, Switzerland: Cable car measurements, CLM5 default and CLM5 modified, which is denoted as "CLM5 w/ transm." in the figure.

upwards, which is not replicated by measurements. This is most likely due to the hourly temporal model resolution in combination with small camera alignment issues.

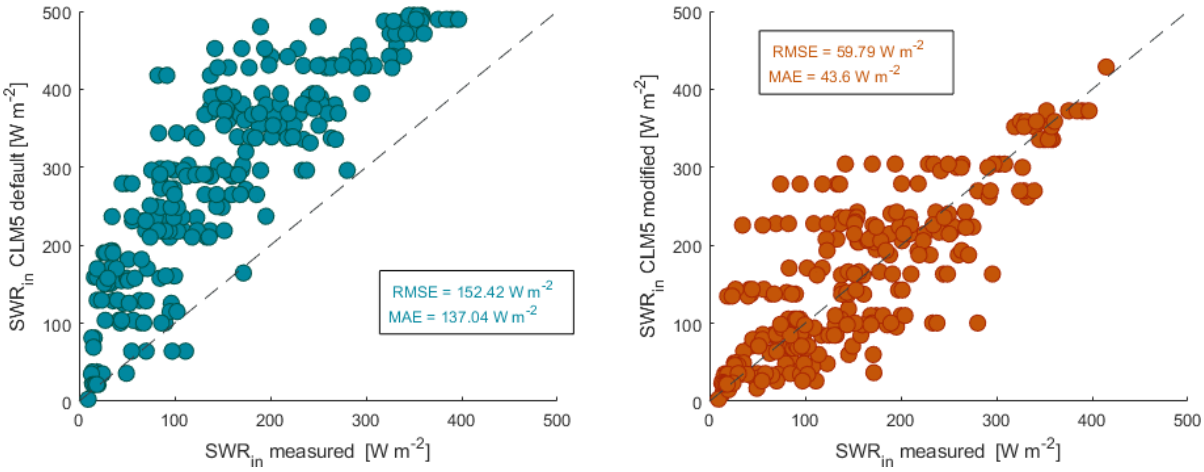

Figure 7.5: Measurements of sub-canopy incoming shortwave radiation (x axes) are plotted against model results (y axes) obtained with a) the CLM5 default and b) the CLM5 modified version.

Measured and modelled differences of all averaged cable car transects between January and May 2018 showed CLM5 modified simulations performed substantially better than the CLM5 default simulations, as RMSE and MAE were reduced by 61% and 68%, respectively.

7.3 Discussion

Cable car measurements demonstrated pronounced small-scale variability of solar transmission through the forest canopy, which was controlled by local canopy structure. Model experiments revealed that this variability in space and time was not captured effectively by CLM5 default simulations. This finding is in agreement with Rosati et al. (2020), who demonstrated radiative heterogeneities within a forest stand often remain unaccounted for in coarse-resolution LSM due to simplified canopy structure representation. The main canopy descriptor in CLM5 default simulations is PAI, a spatially integrated metric which neglects canopy structural heterogeneity. Consequently, the complex interplay between solar position and gaps in the surrounding canopy, as evidenced by measurements (Malle et al., 2019, Mazzotti et al., 2019), could not be represented by the two-stream approximation 'big leaf' approach of CLM5 default simulations. Findings are consistent with Yuan et al. (2017), who found the two-stream approximation performed best in dense forests with limited spatial heterogeneity, and Sellers (1985) showing the two-stream approximation only takes zenith angle into account, which does not allow for non-symmetrical radiative transfer through forest canopies.

In contrast, CLM5 modified simulations were able to replicate measured variability in space and time more accurately. Mazzotti, Essery, Webster, Malle and Jonas (2020) evaluated this approach using the snow model FSM2 (Essery, 2015), demonstrating benefits of accounting for detailed spatial patterns of shortwave radiation transfer from a snow model perspective. Performing transmissivity calculations offline with the radiative transfer algorithm of Jonas et al. (2020) allowed maintaining the original structure and computational efficiency of CLM5, which makes this approach feasible for potential larger-scale applications. HPEval used in-situ hemispherical photographs along cable car transects as part of this experimental design. The potential to apply this methodology over larger spatial extents is becoming possible using airborne lidar measurements of forest canopies to create detailed canopy structure information, which allows enhanced canopy characterization (Zellweger et al., 2019), and radiative transfer calculations, e.g. Musselman et al. (2013). Using lidar data, Webster et al. (2020) developed methods efficient enough to resolve insolation patterns over $\sim 1km^2$ by creating and enhancing synthetic hemispherical images and further using them as input to HPEval. Feasibility of pairing such approaches to large scale models like CLM5 is increasing and is critical to solve regional and global hydroclimatological questions. Such an approach would allow physical fidelity of canopy radiative transfer while also fulfilling computational demands of a global-scale land surface models.

Assessment of measured and modelled forest canopy shortwave radiative transfer demonstrated the importance of accounting for directionality of solar irradiance. However, the

comparative analysis of CLM5 default and CLM5 modified focused exclusively on the downward radiative transfer through the forest canopy. Yet in CLM5 default simulations, the two-stream approximation also accounts for upward radiative transfer to calculate overall LSA. Upward radiative transfer in CLM5 modified simulations was approximated by sky view fraction (VF_{Sky}), which in contrast to the two-stream approximation does not account for multiple reflections within the forest canopy. Future research on LSA should therefore focus on directly comparing above canopy LSA measurements with CLM5 default and modified simulations, from the point-scale to larger spatial extents. In particular, ensuring simulations are right for the right reasons (Kirchner, 2006), rather than over-compensating for underlying unrealistic premises which can not be explained by physical processes and observations, i.e. "right for the wrong reasons", is paramount Zhang et al. (2013).

7.4 Chapter Summary

In this chapter, the previously presented sub-canopy cable car measurements (see Chapter 5) were used to evaluate the performance of the radiative transfer scheme implemented in the Community Land Model 5.0 (CLM5) over seasonally snow-covered forest stands in a sub-alpine environment from a sub-canopy incoming shortwave radiation perspective. Default CLM5 simulations did not adequately reflect measured spatial and temporal variability in sub-canopy incoming shortwave radiation. Upon integration of a time-varying transmissivity for direct shortwave radiation into CLM5, directionality of solar irradiance could be taken into account. Results with this modified version of CLM5 showed measured variability of sub-canopy incoming shortwave radiation was replicated more accurately, as RMSE and MAE were reduced by 61% and 68%, respectively. This underlines the importance of accounting for directionality in shortwave radiation, which may help to decrease uncertainty in LSA simulations across seasonally snow-covered forested environments.

Chapter 8

Summary and Outlook

8.1 Summary

The overall aim of this research was to improve understanding of forest-snow-atmosphere interactions, and more specifically of radiative processes in seasonally snow-covered forests and their representation in land surface models. This was achieved through a combination of novel measurement techniques, extensive field data collection in boreal, sub-alpine and alpine forests stands, and model experiments with the most up-to-date Community Land Model 5.0 (CLM5). New data collection methods include a custom-made cable car system to capture radiative regimes below forest stands and a UAV system to capture radiative regimes above forest stands, both in conjunction with automatic weather stations to capture meteorological boundary conditions.

Trees exert a principal control on snow dynamics in forested environments (Musselman and Pomeroy, 2017, Roth and Nolin, 2017), which further affects energy exchanges between the land surface and the atmosphere (Bonan et al., 1992, Loranty et al., 2014). For accurate prediction of meltwater runoff from snow-dominated forested watersheds, as well as land-atmosphere energy fluxes, reliable estimates of radiative transfer processes through vegetation canopies to the forest floor are essential (Lawler and Link, 2011, Seyednasrollah and Kumar, 2014). Chapter 4 investigated sub-canopy radiation processes in seasonally snow-covered forest environments using distributed sub-canopy radiation measurements in a discontinuous evergreen needle-leaf forest stand in the Swiss Alps. A custom-made cable car system allowed measurement of incoming and outgoing shortwave and longwave radiation along a single transect in Davos Laret, Switzerland. In addition, hemispherical photographs taken concurrently from the cable car measured view fractions of shaded snow, sunlit snow, and bare ground at each measurement point along the transect. Spatiotemporal analysis of the sub-canopy shortwave radiation data collected during a clear-sky day revealed a strong linear relationship between outgoing shortwave

radiation and sunlit snow-view fraction (R = 0.94). This finding revealed canopy structural snow shading as a key control of the sub-canopy shortwave radiation budget. Moreover, sub-canopy shortwave radiation measurements during partial snow cover conditions showed effective albedo to decrease substantially with snow cover fraction. This demonstrated the importance of accurately quantifying partial snow cover extent when aiming to calculate sub-canopy outgoing shortwave radiation and the resulting effective albedo below a forest stand.

Sub-canopy incoming longwave radiation increased throughout the melt period due to elevated air and canopy temperatures. Furthermore, denser forest surroundings coincided with stronger longwave radiation enhancement. Fractional snow cover was shown to be of particular importance for outgoing longwave radiation, which was up to 60 W m^{-2} larger in areas where snow had melted, compared to a maximum outgoing longwave radiation of 309 W m^{-2} in areas with full snow cover. Net all-wave radiation was dominated by shortwave radiation whenever direct insolation of the forest floor occurred. However, at times and locations where canopy structure inhibited direct insolation, which was often most of the day, longwave radiation dominated the sub-canopy radiation budget.

The work outlined above greatly improved our understanding of the sub-canopy radiation budget, but an equally important component of the energy budget is the above-canopy LSA. The presence of trees generally leads to a reduction in LSA of snow-covered areas (Bonan et al., 1992), which has wide-ranging climatic implications (Abe et al., 2017). However, complex interactions controlling LSA continue to be a source of uncertainty in land surface models, with particularly large biases across boreal evergreen forests (Loranty et al., 2014, Thackeray et al., 2019). The task of reducing this uncertainty has been hampered by limited in-situ measurements, as LSA is usually measured from meteorological towers (point-scale) which struggle to represent areas greater than the sensor footprint. To address limitations of fixed sensor footprints, a UAV was used in this thesis, which allowed variable measurement heights and the flexibility to measure at multiple locations above a forest canopy. An extensive dataset of airborne LSA measurements, co-located with measurements of canopy structure and snow surface shading, captured a large range of canopy structures, solar angles and meteorological conditions in alpine, sub-alpine (Switzerland) and boreal (Finland) forested environments. The effects on LSA of tree species, intercepted snow, meteorological boundary conditions, fractional snow cover and canopy structural shading were all examined and quantified. The dependency of LSA on tree species in both sub-alpine and boreal forest environments showed clear differences in the snow-masking effect of vegetation between needle-leaf and deciduous forest stands. Intercepted snow in the canopy was shown to be a strong modulator of LSA, and measurements conducted during intercepted canopy snow conditions generated a

unique dataset for future model evaluation efforts, as model representation of intercepted snow and unloading is paramount for accurate simulation of LSA (Stähli et al., 2009, Bartlett and Verseghy, 2015). Measurements of solar angle and shading revealed strong correlations between LSA and sunlit-snow across a range of tree species, solar angles and canopy structures, further emphasizing the first order control canopy structural shading plays in modulating LSA. These results built on the findings of Chapter 4 by exploring the concept of shading as a key control on outgoing shortwave radiation in different environments, as well as expanding the scope by looking at processes above the forest canopy.

To bridge the gap between coarse-scale climate models and in-situ measurements, evaluation of CLM5 point-scale simulations allowed process level assessment of algorithms used within global climate modelling frameworks. Chapter 6 showed CLM5 simulations did not adequately capture the measured spatial and temporal variability in LSA. This problem was attributed to the generalized canopy structure in CLM5, which over-simplifies interactions between solar position and canopy heterogeneity. While measurements showed strong diurnal signals in LSA and distinct effects of solar zenith and azimuth angles, CLM5 simulations showed minimal diurnal variability. Furthermore, model sensitivity experiments showed that simulated LSA was relatively insensitive to increasing Plant Area Index (PAI) values above 2, which is in stark contrast to the measurements outlined herein. As shown in Figure 6.12, approximately 92% of the needle-leaf evergreen tree-covered pixels across the northern hemisphere have a PAI above two. This leaves only 8% of the needle-leaf evergreen tree-covered pixels where differences in canopy density are leading to differences in CLM5 simulated LSA. For this reason, CLM5 overestimated LSA by up to 66% in sparse forest environments. The use of effective PAI values as a simple first-order correction for this discrepancy between measured and simulated LSA in sparse forest environments substantially improved model results (64-76% RMSE reduction). However, the large biases suggest a more robust solution is needed, as the use of effective PAI values did not improve the ability of CLM5 to replicate diurnal variability in LSA. In that regard, more complex canopy descriptors are required in order to account for canopy gaps and capture the structural heterogeneity of forest stands.

Chapter 7 explored a potential avenue for future model development through integration of a time-varying transmissivity for direct shortwave radiation (e.g. HPEval, Jonas et al., 2020), allowing directionality of solar irradiance, which bypassed the default radiative scheme in CLM5 (two-stream approximation). Results showed measured variability of sub-canopy incoming shortwave radiation was replicated more accurately using the modified CLM5 scheme; with a 61% RMSE and 68% MAE reduction compared to the CLM5

default configuration. With further model development this approach may help to decrease uncertainty in LSA simulations across seasonally snow-covered forested environments.

8.2 Outlook

Results presented in this thesis have enhanced understanding of the temporal and spatial dynamics of forest-snow-albedo interactions. However, much scope for future research remains, both in terms of data acquisition over larger spatial extents and process-based modelling strategies across spatial and temporal scales.

8.2.1 Data acquisition

High-quality measurements will continue to be needed as benchmarks for land surface model evaluation as well as to enhance process-based understanding of land surface albedo. In future studies, both sub-canopy and above-canopy measurements should be expanded from broadband to spectral albedo, which would help quantify the impact of forests on spatiotemporal variability of snow surface properties. More specifically, the effects of litter and aerosols on land surface albedo could be investigated. However, such measurements would be more challenging to obtain, as spectrometers used for spectral albedo measurements are very sensitive to sensor tilt and uneven surfaces (Picard et al., 2020). UAV measurements could further be combined with RGB imagery, a concept proven by Ryan et al. (2017), which would allow evaluation of fractional snow cover extents and land surface albedo of forested environments over larger spatial extents.

Data collection methods such as UAVs are, however, only useful for model evaluation across small spatial scales (e.g. forest stand scale). Once model domains approach regional scales (e.g. the extent of Switzerland/Finland), such forest stand-scale studies need to be leveraged with emerging space-borne data. In terms of 3-D forest structure and vegetation distribution, active and passive remote sensing satellite LiDAR products are becoming more wide spread, e.g. NASA's ICESat2 satellite (Neuenschwander and Pitts, 2019, Narine et al., 2019), which carries the Advanced Topographic Laser Altimeter System (ATLAS) and gives high spatial (10-100m) but very low temporal resolution, or the Global Ecosystem Dynamics Investigations (GEDI, Dubayah et al., 2020) deployed at the International Space Station, which covers 51.6°N-51.6°S at a footprint resolution of 25 m. Such data could possibly be used in combination with TanDEM-X (TDX) mission data (Qi and Dubayah, 2016).

From an albedo standpoint, in addition to the commonly used moderate resolution imaging spectroradiometer (MODIS, e.g. Wang et al., 2004, Malmros et al., 2018) onboard the NASA Terra and Aqua satellites, the Ocean and Land Colour Instrument (OLCI) onboard Sentinel-3A/B (Kokhanovsky et al., 2019) provides spectral reflectance measurements in the range 400–1020 nm. OLCI hence has potential for future LSA retrievals across snow-covered forests, although spectral and broadband albedo are only provided at a spatial grid of 300m. Even the highest temporal resolution satellite data usually results in daily retrievals at best, which limits analysis of diurnal variability in LSA. Furthermore, such optical satellite retrievals are only possible under clear-sky conditions, as cloud coverage impairs the data quality. Measurements acquired under cloudy conditions are therefore mostly rejected (Schaaf et al., 2008). To mitigate this problem as well as the limited temporal and spatial resolution of satellite retrievals, future research should explore the concept of data assimilation by leveraging satellite retrievals, in-situ measurements and model simulations of LSA. In recent years, data assimilation approaches have gained popularity amongst snow modellers (Girotto et al., 2020, Largeron et al., 2020) but much potential remains for future studies.

Alternatively, machine learning algorithms, e.g. random forest or neural networks, are emerging tools (Ke et al., 2016) which could be useful for forest-snow-albedo related investigations. More specifically, the potential to combine relatively coarse resolution satellite data (e.g. OLCI 300m spatial grid) with machine learning algorithms is increasing (Cornejo-Bueno et al., 2019). Such an approach, for example in combination with higher resolution in-situ learning datasets (e.g. UAV-based LSA measurements) seems a promising avenue for future research, with great potential to enhance our understanding of forest-snow-albedo interactions.

8.2.2 Modelling strategies

High-resolution LSM approaches are gaining in popularity as tools to investigate small scale processes, often unaccounted for in coarser resolution predictions (Minder et al., 2016). As a first step, a multi-resolution model infrastructure would help to bridge the gap between exhaustive site scale measurements of individual processes and their global relevance. For example, evaluating CLM5 offline simulations over the spatial extent of Switzerland at decreasing spatial resolutions, e.g. hemispheric coarse (1°), hemispheric intermediate (0.25°), regional high (1km) and point-scale, would assess and mitigate the degradation of process representation arising from unresolved sub-grid variability as model resolution is reduced. At the same time, land surface heterogeneity could be fully resolved while also preserving consistent physics. Such an approach seems feasible, as Zhu et al.

(2020) has recently used CLM5 in a similar way to investigate effects of irrigation on hydrological dynamics for a watershed in the United States.

Computational efficiency is not yet sufficient for high resolution simulations to be run over extended periods of time across the entire northern hemisphere. Consequently, future research should also test variable resolution modelling within the same simulation, e.g. high-resolution refinement over highly variably forest stands/complex terrain. Such variable resolution approaches have proven to enhance simulations of Atlantic tropical storms (Zarzycki and Jablonowski, 2014) or precipitation over the rocky mountain range (Wu et al., 2017), although their highest resolution refined grid was only 0.25°. Nevertheless it demonstrates the feasibility of variable resolution modelling with CLM5, and shows great potential to decrease uncertainty associated with forest-snow-atmosphere interactions in coarse-scale models. Potentially an even more promising approach would be to use variable-resolution unstructured meshes which allow for smooth transitions from very fine to coarse resolution in an entirely flexible manner. This approach has been previously applied to cold regions hydrology for domains ranging from point scale to basin (100 km^2) to provincial ($>$ 1 000 000 km^2) scales (Marsh et al., 2020).

Such model experiments would quantify limitations in modelling vegetation as uniform, single layers, and identify scenarios where accounting for geometrical arrangement of canopy elements was important for accurate process representation of radiative processes. More specifically and following the findings of the modelling experiments of this thesis, accounting for directionality of solar radiation in coarse-scale models should be a particular focus. The potential for such model development endeavours is increasing, as recent efforts have resulted in methods that are efficient enough to resolve insolation patterns down to meter resolution over $\sim$ 1km^2 areas (Webster et al., 2020).

A multi-resolution model infrastructure in combination with variable resolution modelling within the same simulation would allow the investigation of many other forest-snow related questions. In particular, the representation of intercepted snow in coarse-scale models has much scope for improvement. Knowledge gaps remain in the quantitative description of snow mass in the canopy, which have profound implications for LSA. Together, such approaches will ultimately result in more accurate land surface albedo simulations, which will directly improve climate modelling via reduced uncertainties associated with forest-snow-atmosphere interactions. This will have far reaching implications for simulations of the snow albedo feedback strength over the Northern Hemisphere Extratropics.

Appendix A

Sensor calibration

Sensor calibration campaigns were performed on two days in Davos, Switzerland (19 June 2018, 23 May 2019) and on one day in Sodankylä, Finland (7 May 2019). On each day all senors (up- and down-looking Kipp & Zonen CMP3 SWR and CGR3 LWR sensors from the cable car and up- and down-looking CMP3 SWR sensors from UAV) were set up next to each other. In Davos, Switzerland the sensors were placed on a flat surface on top of the main SLF building. A white cloth was placed underneath the sensors and nothing obscured the view-field of the radiation sensors. In Sodankylä, the sensors were placed on top of the radiation tower, in proximity to the operational radiation sensors of FMI. Every few hours the sensors were checked and re-levelled, resulting in small data gaps in the calibration data, but ensuring high data quality.

A.1 LWR - CGR3 pyrgeometers

In the following LWR measurements taken with the two cable car CGR3s are shown for all three calibration campaign days. No correction was applied as the difference between sensors was minimal.

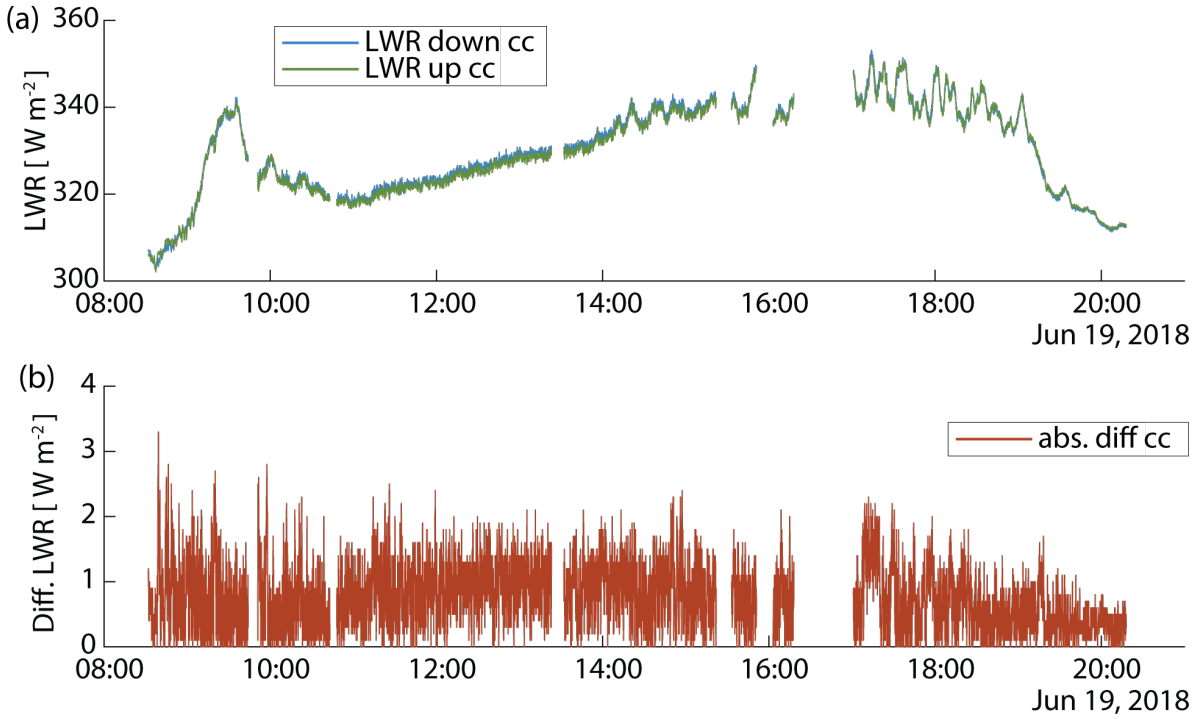

Figure A.1: LWR calibration performed in Davos on 19 June 2018. (a) shows measured LWR of each sensor and (b) visualizes absolute differences between the measured values of the respective sensors.

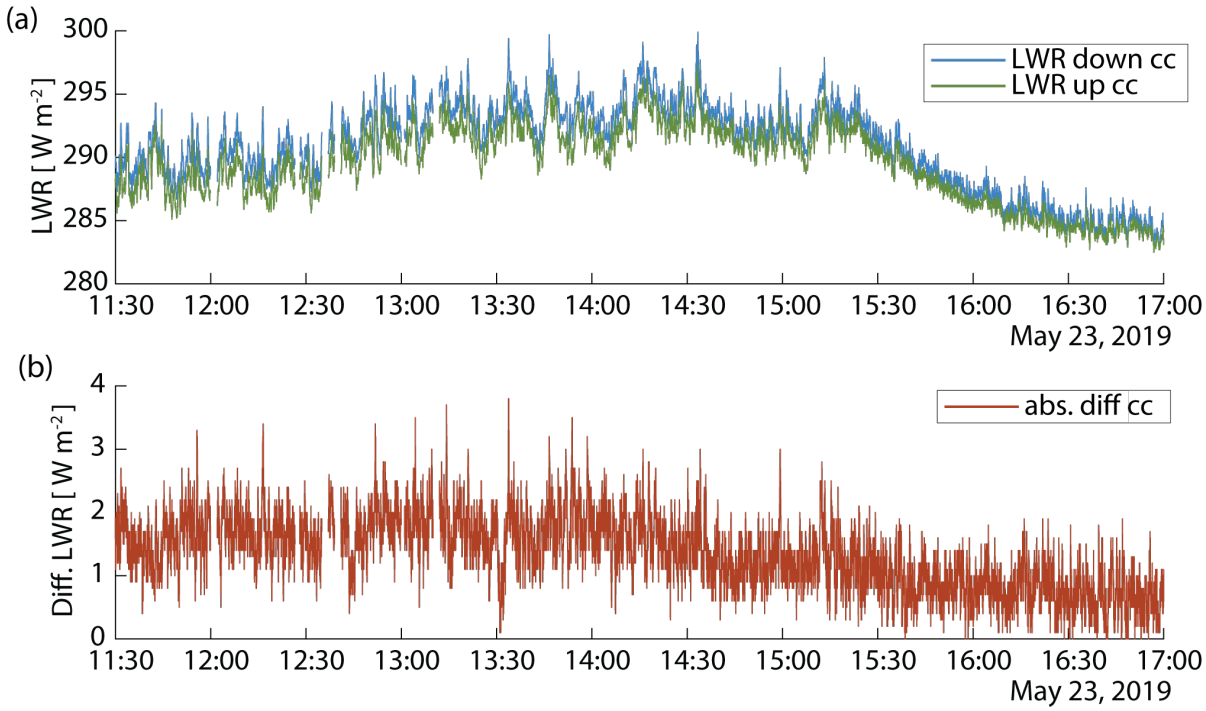

Figure A.2: LWR calibration performed in Davos (CH) on 23 May 2019. (a) shows measured LWR of each sensor and (b) visualizes absolute differences between the measured values of the respective sensors.

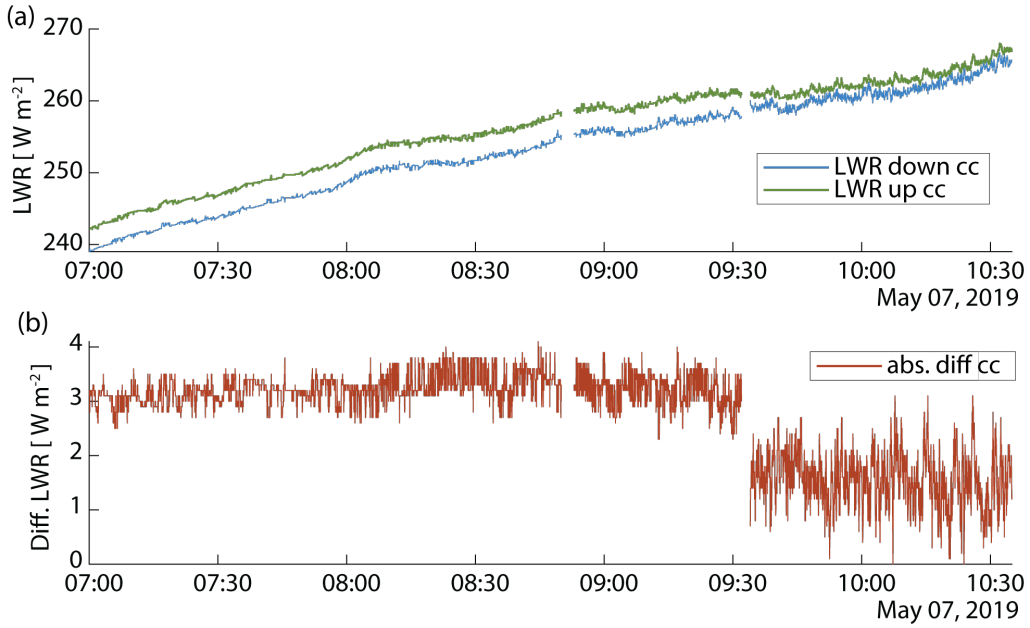

Figure A.3: LWR calibration performed in Sodankylä (FIN) on 07 May 2019. (a) shows measured LWR of each sensor and (b) visualizes absolute differences between the measured values of the respective sensors.

A.2 SWR - CMP3 pyranometers

In the following SWR measurements taken with the two cable car CGR3s as well as the two UAV CGR3s are shown for all three calibration campaign days.

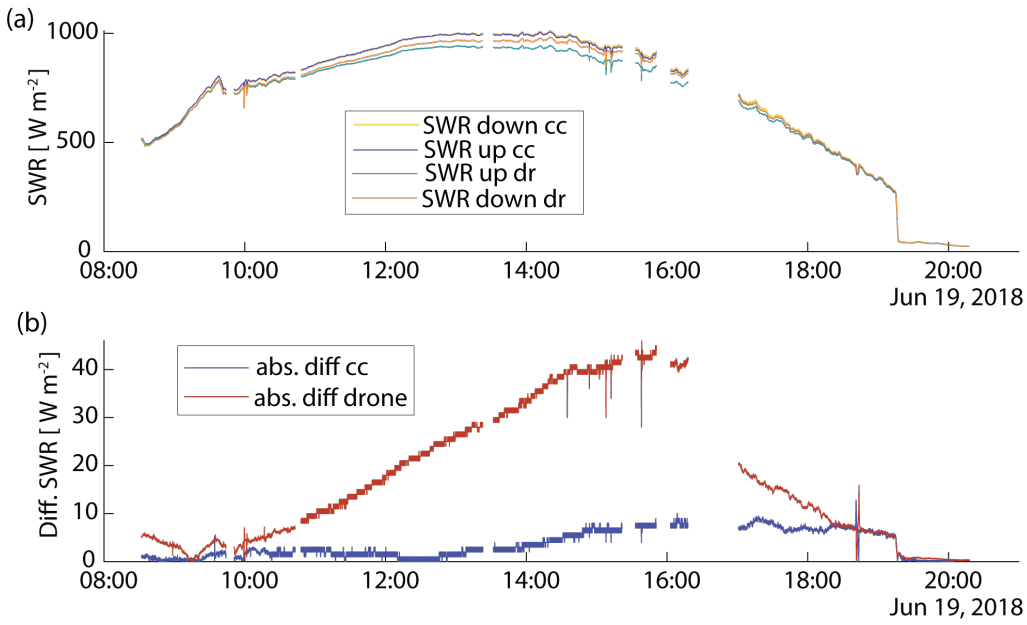

Figure A.4: SWR calibration performed in Davos on 19 June 2018. (a) shows measured SWR of each sensor and (b) visualizes absolute differences between the measured values of the respective sensors

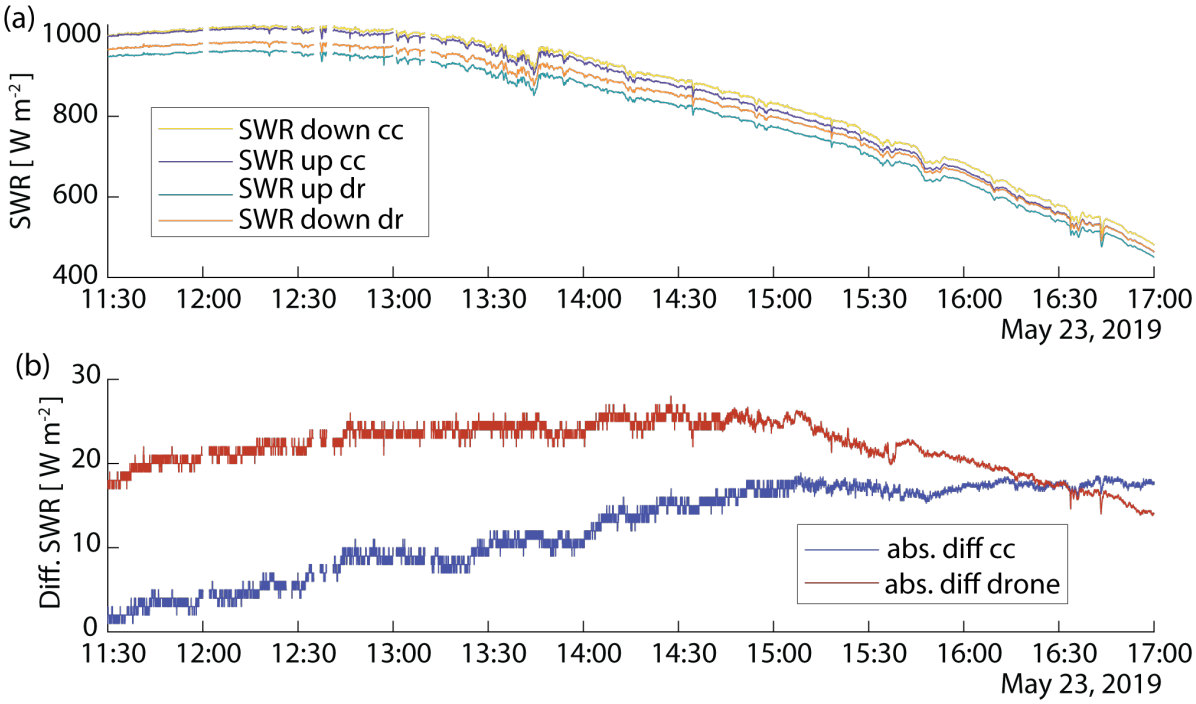

Figure A.5: SWR calibration performed in Davos (CH) on 23 May 2019. (a) shows measured SWR of each sensor and (b) visualizes absolute differences between the measured values of the respective sensors.

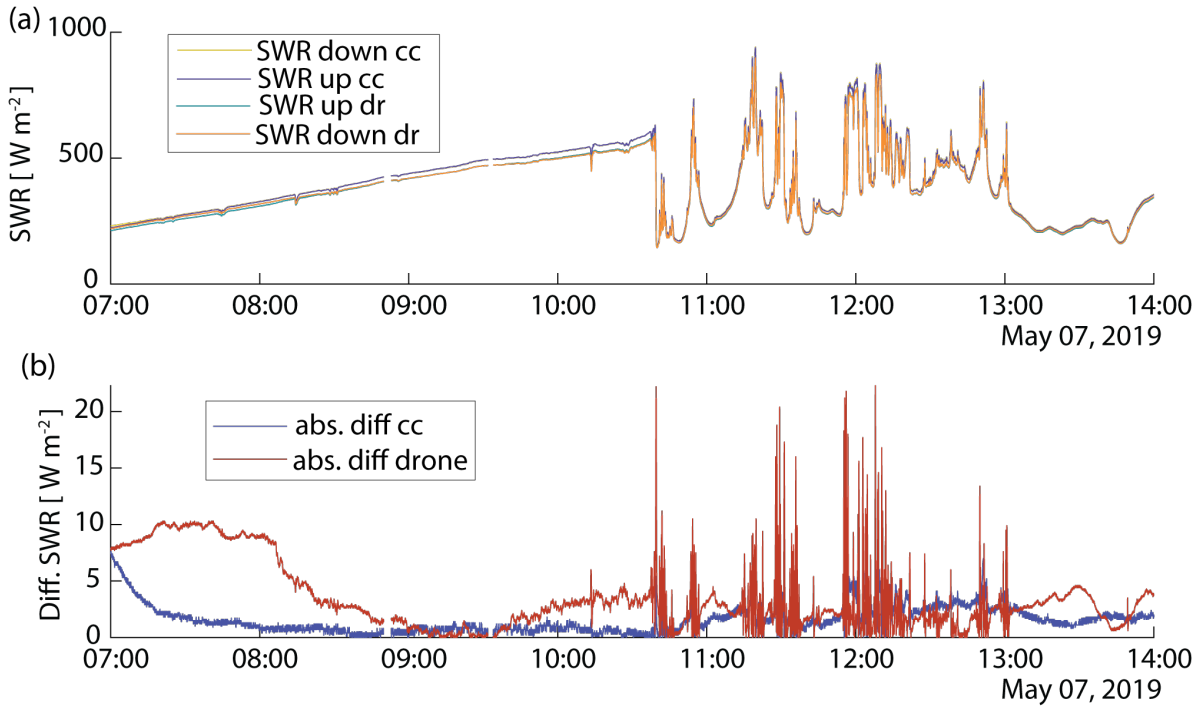

Figure A.6: SWR calibration performed in Sodankylä (FIN) on 07 May 2019. (a) shows measured SWR of each sensor and (b) visualizes absolute differences between the measured values of the respective sensors

The following (SWR magnitude dependent) relative correction was applied to the down-looking UAV sensor: SWR_{cor}= SWR x $0.978 + 0.297$, results of which are shown in the following plot.

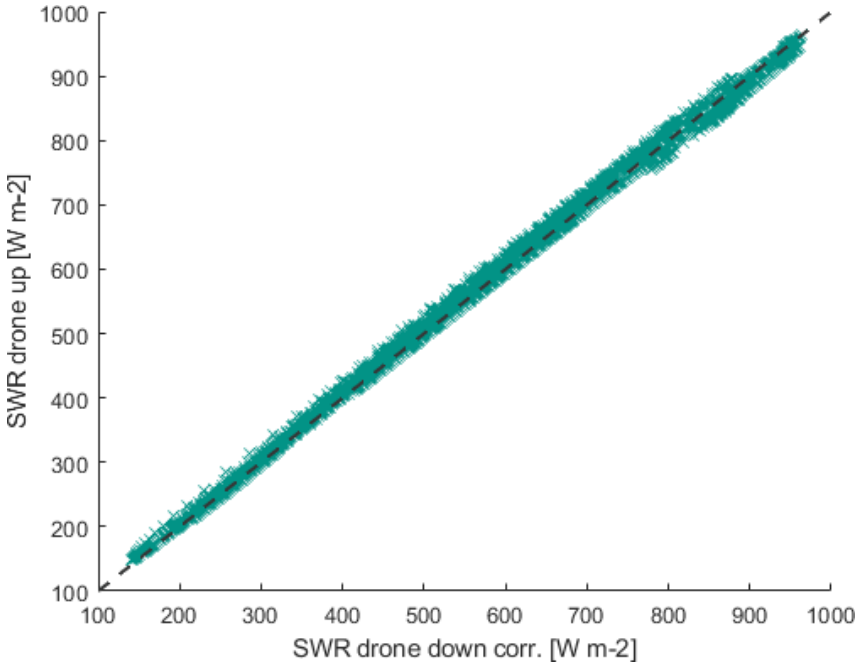

Figure A.7: Applied relative calibration for SWR sensors

References

Abe, M., Takata, K., Kawamiya, M. and Watanabe, S. (2017), 'Vegetation masking effect on future warming and snow albedo feedback in a boreal forest region of northern Eurasia according to MIROC-ESM', *Journal of Geophysical Research: Atmospheres* **122**(17), 9245–9261.

Allen, M., Poggiali, D., Whitaker, K., Marshall, T. R. and Kievit, R. A. (2019), 'Raincloud plots: a multi-platform tool for robust data visualization', *Wellcome open research* **4**, 63.

Anderson, E. A. (1976), A Point Energy and Mass Balance Model of a Snow Cover, Technical report, NOAA Tech. Rep. NWS 19.

Asner, G. P., Wessman, C. A., Schimel, D. S. and Archer, S. (1998), 'Variability in leaf and litter optical properties: Implications for BRDF model inversions using AVHRR, MODIS, and MISR', *Remote Sensing of Environment* **63**(3), 243–257.

Baartman, J. E., Melsen, L. A., Moore, D. and van der Ploeg, M. J. (2020), 'On the complexity of model complexity: Viewpoints across the geosciences', *Catena* **186**(February 2019), 104261.

Baldocchi, D. and Collineau, S. (1994), *The Physical Nature of Solar Radiation in Heterogeneous Canopies: Spatial and Temporal Attributes*, ACADEMIC PRESS, INC.

Barnett, T. P., Adam, J. C. and Lettenmaier, D. P. (2005), 'Potential impacts of a warming climate on water availability in snow-dominated regions.', *Nature* **438**(7066), 303–309.

Barnett, T. P., Pierce, D. W., Hidalgo, H. G., Bonfils, C., Santer, B. D., Das, T., Bala, G., Wood, A. W., Nozawa, T., Mirin, A. a., Cayan, D. R. and Dettinger, M. D. (2008), 'Human-Induced Changes in the Hydrology of the Western United States', *Science* **319**(February), 1080–1083.

Bartlett, P. A. and Verseghy, D. L. (2015), 'Modified treatment of intercepted snow improves the simulated forest albedo in the Canadian Land Surface Scheme', *Hydrological Processes* **29**(14), 3208–3226.

Berdahl, P. and Fromberg, R. (1982), 'The thermal radiance of clear skies', *Solar Energy* **29**(4), 299–314.

Berghuijs, W. R., Woods, R. A. and Hrachowitz, M. (2014), 'A precipitation shift from snow towards rain leads to a decrease in streamflow', *Nature Climate Change* **4**(7), 583–586.

Betts, A. K. and Ball, J. H. (1997), 'Albedo over the boreal forest', *Journal of Geophysical Research: Atmospheres* **102**(96), 901–909.

Blanken, P. D., Black, T. A., Neumann, H. H., Den Hartog, G., Yang, P. C., Nesic, Z. and Lee, X. (2001), 'The seasonal water and energy exchange above and within a boreal aspen forest', *Journal of Hydrology* **245**(1-4), 118–136.

Bogren, W. S., Burkhart, J. F. and Kylling, A. (2016), 'Tilt error in cryospheric surface radiation measurements at high latitudes: a model study', *The Cryosphere* **10**, 613–622.

Bonan, G. B. (2008), 'Forests and Climate Change: Forcings, Feedbacks, and the Climate Benefits of Forests', *Science* **320**(5882), 1444–1449.

Bonan, G. B., Bonan and Gordon B (1996), A Land Surface Model (LSM Version 1.0) for Ecological, Hydrological, and Atmospheric Studies : Technical Description and User's Guide, Technical report, National Center for Atmospheric Research.

Bonan, G. B., David, P. and Thompson, S. L. (1992), 'Effects of boreal forest vegetation on global climate', *Nature* **359**, 716–718.

Bonfils, C. J. W., Phillips, T. J., Lawrence, D. M., Cameron-Smith, P., Riley, W. J. and Subin, Z. M. (2012), 'On the influence of shrub height and expansion on northern high latitude climate', *Environmental Research Letters* **7**(1), 015503.

Boone, A. A. and Etchevers, P. (2001), 'An intercomparison of three snow schemes of varying complexity coupled to the same land surface model: Local-scale evaluation at an alpine site', *Journal of Hydrometeorology* **2**(4), 374–394.

Bright, R. M., Eisner, S., Lund, M. T., Majasalmi, T., Myhre, G. and Astrup, R. (2018), 'Inferring Surface Albedo Prediction Error Linked to Forest Structure at High Latitudes', *Journal of Geophysical Research: Atmospheres* **123**, 4910–4925.

Broxton, P. D., Harpold, A. A., Biederman, J. A., Troch, P. A., Molotch, N. P. and Brooks, P. D. (2015), 'Quantifying the effects of vegetation structure on snow accumulation and ablation in mixed-conifer forests', *Ecohydrology* **8**(6), 1073–1094.

Burrell, A. L., Evans, J. P. and De Kauwe, M. G. (2020), 'Anthropogenic climate change has driven over 5 million km2 of drylands towards desertification', *Nature Communications* **11**(1), 1–11.

Carlson, K. M., Coulthard, B. and Starzomski, B. M. (2017), 'Autumn Snowfall Controls the Annual Radial Growth of Centenarian Whitebark Pine (Pinus albicaulis) in the Southern Coast Mountains, British Columbia, Canada', *Arctic, Antarctic, and Alpine Research* **49**(1), 101–113.

Carroll, J. J. (1985), 'Global transmissivity and diffuse fraction of solar radiation for clear and cloudy skies as measured and as predicted by bulk transmissivity models', *Solar Energy* **35**(2), 105–118.

Carroll, J. J. and Fitch, B. W. (1981), 'Effects of solar elevation and cloudiness on snow albedo at the South Pole.', *Journal of Geophysical Research* **86**(C6), 5271–5276.

Chapin, F. S. (2005), 'Role of Land-Surface Changes in Arctic Summer Warming', *Science* **310**(5748), 657–660.

Chen, J. M., Rich, P. M., Gower, S. T., Norman, J. M. and Plummer, S. (1997), 'Leaf area index of boreal forests: Theory, techniques, and measurements', *Journal of Geophysical Research: Atmospheres (1984–2012)* **102**(D24), 29429–29443.

Church, J. A. and White, N. J. (2006), 'A 20th century acceleration in global sea-level rise', *Geophysical Research Letters* **33**(1), 94–97.

Cornejo-Bueno, L., Casanova-Mateo, C., Sanz-Justo, J. and Salcedo-Sanz, S. (2019), 'Machine learning regressors for solar radiation estimation from satellite data', *Solar Energy* **183**(March), 768–775.

Derksen, C. and Brown, R. (2012), 'Spring snow cover extent reductions in the 2008-2012 period exceeding climate model projections', *Geophysical Research Letters* **39**(19), 1–6.

Dickinson, R. E. (1983), 'Land surface processes and climate—surface albedos and energy balance', *Advances in Geophysics* **25**(C), 305–353.

Dorman, J. L. and Sellers, P. J. (1989), 'A Global Climatology of Albedo, Roughness Length and Stomatal Resistance for Atmospheric General Circulation Models as Represented by the Simple Biosphere Model (SiB)', *Journal of Applied Meteorology* **28**(9), 833–855.

Dubayah, R., Blair, J. B., Goetz, S., Fatoyinbo, L., Hansen, M., Healey, S., Hofton, M., Hurtt, G., Kellner, J., Luthcke, S., Armston, J., Tang, H., Duncanson, L., Hancock, S., Jantz, P., Marselis, S., Patterson, P. L., Qi, W. and Silva, C. (2020), 'The Global

Ecosystem Dynamics Investigation: High-resolution laser ranging of the Earth's forests and topography', *Science of Remote Sensing* **1**(January), 100002.

Ellis, C. R., Pomeroy, J. W., Brown, T. and MacDonald, J. (2010), 'Simulation of snow accumulation and melt in needleleaf forest environments', *Hydrology and Earth System Sciences* **14**(6), 925–940.

Ellis, C. R., Pomeroy, J. W., Essery, R. L. H. and Link, T. E. (2011), 'Effects of needleleaf forest cover on radiation and snowmelt dynamics in the Canadian Rocky Mountains', *Canadian Journal of Forest Research* **41**(March), 608–620.

Erbs, D. G., Klein, S. A. and Duffie, J. A. (1982), 'Estimation of the diffuse radiation fraction for hourly, daily and monthly-average global radiation', *Solar Energy* **28**(4), 293–302.

Essery, R. (2015), 'A factorial snowpack model (FSM 1.0)', *Geoscientific Model Development* **8**(12), 3867–3876.

Essery, R., Bunting, P., Rowlands, A., Rutter, N., Hardy, J., Melloh, R., Link, T., Marks, D. and Pomeroy, J. (2008), 'Radiative Transfer Modeling of a Coniferous Canopy Characterized by Airborne Remote Sensing', *Journal of Hydrometeorology* **9**(2), 228–241.

Essery, R., Morin, S., Lejeune, Y. and B Ménard, C. (2013), 'A comparison of 1701 snow models using observations from an alpine site', *Advances in Water Resources* **55**, 131–148.

Essery, R., Pomeroy, J., Ellis, C. and Link, T. (2008), 'Modelling longwave radiation to snow beneath forest canopies using hemispherical photography or linear regression', *Hydrological Processes* **22**(15), 2788–2800.

Essery, R., Rutter, N., Pomeroy, J., Baxter, R., Stähli, M., Gustafsson, D., Barr, A., Bartlett, P. and Elder, K. (2009), 'SNOWMIP2: An Evaluation of Forest Snow Process Simulations', *Bulletin of the American Meteorological Society* **90**(8), 1120–1135.

Fassnacht, S. R. (2004), 'Estimating alter-shielded gauge snowfall undercatch, snowpack sublimation, and blowing snow transport at six sites in the coterminous USA', *Hydrological Processes* **18**(18), 3481–3492.

Flanner, M. G., Shell, K. M., Barlage, M., Perovich, D. K. and Tschudi, M. A. (2011), 'Radiative forcing and albedo feedback from the Northern Hemisphere cryosphere between 1979 and 2008', *Nature Geoscience* **4**(3), 151–155.

Flanner, M. G. and Zender, C. S. (2005), 'Snowpack radiative heating: Influence on Tibetan Plateau climate', *Geophysical Research Letters* **32**(6), 1–5.

Fletcher, C. G., Thackeray, C. W. and Burgers, T. M. (2015), 'Evaluating biases in simulated snow albedo feedback in two generations of climate models', *Journal of Geophysical Research* **120**(1), 12–26.

Girotto, M., Musselman, K. N. and Essery, R. L. (2020), 'Data Assimilation Improves Estimates of Climate-Sensitive Seasonal Snow', *Current Climate Change Reports* **6**(3), 81–94.

Gouttevin, I., Lehning, M., Jonas, T., Gustafsson, D. and Mölder, M. (2015), 'A two-layer canopy model with thermal inertia for an improved snowpack energy balance below needleleaf forest (model SNOWPACK, version 3.2.1, revision 741)', *Geoscientific Model Development* **8**(8), 2379–2398.

Granger, R. J. and Gray, D. M. (1990), 'A net radiation model for calculating daily snowmelt in open environments', *Nordic Hydrology* **21**(4-5), 217–234.

Gregory, J. M. (2004), 'Threatened loss of the Greenland ice-sheet', *Nature Communications* **428**(April), 616.

Gudmundsson, L., Seneviratne, S. I. and Zhang, X. (2017), 'Anthropogenic climate change detected in European renewable freshwater resources', *Nature Climate Change* **7**(11), 813–816.

Hahn, D. and Shukla, J. (1976), 'An Apparent Relationship between Eurasian Snow Cover and Indian Monsoon Rainfall', *Journal of the Atmospheric Sciences.* **33**, 2461–2462.

Hall, A. (2004), 'The role of surface albedo feedback in climate', *Journal of Climate* **17**(7), 1550–1568.

Hamlet, A. F., Mote, P. W., Clark, M. P. and Lettenmaier, D. P. (2005), 'Effects of Temperature and Precipitation Variability on Snowpack Trends in the Western United States', *Journal of Climate* **18**(21), 4545–4561.

Hartmann, D., Klein Tank, Albert M.G. Rusticucci, M., Alexander, L. V., Broennimann, S., Charabi, Yassine Dentener, F. J., Dlugokencky, Edward J. Easterling, D. R., Kaplan, A., Soden, B., Thorne, P., Wild, M. and Zhai, P. (2013), Observations: Atmosphere and surface, *in* 'Climate Change 2013 the Physical Science Basis: Working Group I Contribution to the Fifth Assessment Report of the Intergovernmental Panel on Climate Change.', Cambridge University Press, pp. 159–254.

Hedstrom, N. and Pomeroy, J. (1998), 'Measurements and modeling of snow interception in the boreal forest', *Hydrological Processes* **12**(March), 1611–1625.

Hellström, R. (2000), 'Forest cover algorithms for estimating meteorological forcing in a numerical snow model', *Hydrological Processes* **14**(18), 3239–3256.

Hock, R., Rasul, G., Adler, C., Caceres, B., Gruber, S., Hirabayashi, Y., Jackson, M., Kaab, A., Kang, S., Kutuzov, S., Milner, A., Molau, U., Morin, S., Orlove, B. and Steltzer, H. (2019), High Mountain Areas, *in* H. Portner, D. Roberts, V. Masson-Delmotte, P. Zhai, M. Tignor, E. Poloczanska, K. Mintenbeck, A. Alegria, M. Nocolai, A. Okem, J. Petzold, B. Rama and N. Weyer, eds, 'IPCC Special Report on the Ocean and Cryosphere in a Changing Climate', Vol. 4, pp. 1–96.

Hoegh-Guldberg, O., Mumby, P., Hooten, A., Steneck, R., Greenfield, P., Gomez, E., Harvell, C., Sale, P., Edwards, A., Caldeira, K., Knowlton, N., C, E., Iglesias-Prieto, R., Muthiga, N., Bradbury, R., Dubi, A. and Hatziolos, M. (2007), 'Coral Reefs Under Rapid Climate Change and Ocean Acidification', *Science* **318**(December 2007), 1737–1743.

Hotovy, O. and Jenicek, M. (2020), 'The impact of changing subcanopy radiation on snowmelt in a disturbed coniferous forest', *Hydrological Processes* (October), 1–17.

Jonas, T. and Essery, R. (2011), 'Snow Cover and Snowmelt in Forest Regions', *Encyclopedia of Snow Ice and Glaciers* pp. 1033–1036.

Jonas, T., Marty, C. and Magnusson, J. (2009), 'Estimating the snow water equivalent from snow depth measurements in the Swiss Alps', *Journal of Hydrology* **378**(1-2), 161–167.

Jonas, T., Webster, C., Mazzotti, G. and Malle, J. (2020), 'HPEval: A canopy shortwave radiation transmission model using high-resolution hemispherical images', *Agricultural and Forest Meteorology* **284**(107903), 1–9.

Jonckheere, I., Fleck, S., Nackaerts, K., Muys, B., Coppin, P., Weiss, M. and Baret, F. (2004), 'Review of methods for in situ leaf area index determination Part I. Theories, sensors and hemispherical photography', *Agricultural and Forest Meteorology* **121**(1-2), 19–35.

Jonsell, U., Hock, R. and Holmgren, B. (2003), 'Spatial and temporal variations in albedo on Storglaciären, Sweden', *Journal of Glaciology* **49**(164), 59–68.

Joseph, J. H. and Wiscombe, W. J. (1976), 'The Delta-Eddington Approcimation for Radiative Flux Transfer', *Journal of the Atmospheric Sciences.* **33**, 2452–2459.

Karl, T. R. and Trenberth, K. E. (2003), 'Modern Global Climate Change', *Science* **302**(5651), 1719–1723.

Ke, Y., Im, J., Park, S. and Gong, H. (2016), 'Downscaling of MODIS One kilometer evapotranspiration using Landsat-8 data and machine learning approaches', *Remote Sensing* **8**(3), 1–26.

Keenan, T. F., Carbone, M. S., Reichstein, M. and Richardson, A. D. (2011), 'The model-data fusion pitfall: Assuming certainty in an uncertain world', *Oecologia* **167**(3), 587–597.

Kim, E., Gatebe, C., Hall, D., Newlin, J., Misakonis, A., Elder, K., Marshall, P., Hiemstra, C., Brucker, L., Marco, E. D., Crawford, C., Hyk Kang, D. and Entin, J. (2017), 'NASA's snowex campagin: Observing seasonal snow in a forested environement', *IEEE International Geoscience and Remote Sensing Symposium (Igarss)* pp. 1388–1390.

Kirchner, J. W. (2006), 'Getting the right answers for the right reasons: Linking measurements, analyses, and models to advance the science of hydrology', *Water Resources Research* **42**(3), 1–5.

Klos, P. Z. and Link, T. E. (2018), 'Quantifying shortwave and longwave radiation inputs to headwater streams under differing canopy structures', *Forest Ecology and Management* **407**(July 2017), 116–124.

Kokhanovsky, A., Lamare, M., Danne, O., Brockmann, C., Dumont, M., Picard, G., Arnaud, L., Favier, V., Jourdain, B., Meur, E. L., Di Mauro, B., Aoki, T., Niwano, M., Rozanov, V., Korkin, S., Kipfstuhl, S., Freitag, J., Hoerhold, M., Zuhr, A., Vladimirova, D., Faber, A. K., Steen-Larsen, H. C., Wahl, S., Andersen, J. K., Vandecrux, B., van As, D., Mankoff, K. D., Kern, M., Zege, E. and Box, J. E. (2019), 'Retrieval of snow properties from the Sentinel-3 Ocean and Land Colour Instrument', *Remote Sensing* **11**(19).

Konzelmann, T. and Ohmura, A. (1995), 'Radiative fluxes and their impact on the energy balance of the Greenland ice sheet', *Journal of Glaciology* **41**(139), 490–502.

Krinner, G., Derksen, C., Essery, R., Flanner, M., Hagemann, S., Clark, M., Hall, A., Rott, H., Brutel-Vuilmet, C., Kim, H., Ménard, C. B., Mudryk, L., Thackeray, C., Wang, L., Arduini, G., Balsamo, G., Bartlett, P., Boike, J., Boone, A., Chéruy, F., Colin, J., Cuntz, M., Dai, Y., Decharme, B., Derry, J., Ducharne, A., Dutra, E., Fang, X., Fierz, C., Ghattas, J., Gusev, Y., Haverd, V., Kontu, A., Lafaysse, M., Law, R., Lawrence, D., Li, W., Marke, T., Marks, D., Nasonova, O., Nitta, T., Niwano, M., Pomeroy, J., Raleigh, M. S., Schaedler, G., Semenov, V., Smirnova, T., Stacke, T., Strasser, U., Svenson, S., Turkov, D., Wang, T., Wever, N., Yuan, H. and Zhou, W. (2018), 'ESM-SnowMIP:

Assessing models and quantifying snow-related climate feedbacks', *Geoscientific Model Development Discussions* .

Kükenbrink, D., Schneider, F. D., Schmid, B., Gastellu-Etchegorry, J. P., Schaepman, M. E. and Morsdorf, F. (2020), 'Modelling of three-dimensional, diurnal light extinction in two contrasting forests', *Agricultural and Forest Meteorology* (August), 108230.

Kunkel, K. E., Robinson, D. A., Champion, S., Yin, X., Estilow, T. and Frankson, R. M. (2016), 'Trends and Extremes in Northern Hemisphere Snow Characteristics', *Current Climate Change Reports* **2**(2), 65–73.

Kuusinen, N., Kolari, P., Levula, J., Porcar-Castell, A., Stenberg, P. and Berninger, F. (2012), 'Seasonal variation in boreal pine forest albedo and effects of canopy snow on forest reflectance', *Agricultural and Forest Meteorology* **164**, 53–60.

Kuusinen, N., Lukeš, P., Stenberg, P., Levula, J., Nikinmaa, E. and Berninger, F. (2014), 'Measured and modelled albedos in Finnish boreal forest stands of different species, structure and understory', *Ecological Modelling* **284**, 10–18.

Largeron, C., Dumont, M., Morin, S., Boone, A., Lafaysse, M., Metref, S., Cosme, E., Jonas, T., Winstral, A. and Margulis, S. A. (2020), 'Toward Snow Cover Estimation in Mountainous Areas Using Modern Data Assimilation Methods: A Review', *Frontiers in Earth Science* **8**(September).

Law, B. E., Tuyl, S. V., Cescatti, A. and Baldocchi, D. D. (2001), 'Estimation of leaf area index in open-canopy ponderosa pine forests at different successional stages and management regimes in Oregon', *Agricultural and Forest Meteorology* **108**, 1–14.

Lawler, R. R. and Link, T. E. (2011), 'Quantification of incoming all-wave radiation in discontinuous forest canopies with application to snowmelt prediction', *Hydrological Processes* **25**(21), 3322–3331.

Lawrence, D. M., Fisher, R. A., Koven, C. D., Oleson, K. W., Swenson, S. C., Bonan, G., Collier, N., Ghimire, B., van Kampenhout, L., Kennedy, D., Kluzek, E., Lawrence, P. J., Li, F., Li, H., Lombardozzi, D., Riley, W. J., Sacks, W. J., Shi, M., Vertenstein, M., Wieder, W. R., Xu, C., Ali, A. A., Badger, A. M., Bisht, G., van den Broeke, M., Brunke, M. A., Burns, S. P., Buzan, J., Clark, M., Craig, A., Dahlin, K., Drewniak, B., Fisher, J. B., Flanner, M., Fox, A. M., Gentine, P., Hoffman, F., Keppel-Aleks, G., Knox, R., Kumar, S., Lenaerts, J., Leung, L. R., Lipscomb, W. H., Lu, Y., Pandey, A., Pelletier, J. D., Perket, J., Randerson, J. T., Ricciuto, D. M., Sanderson, B. M., Slater, A., Subin, Z. M., Tang, J., Thomas, R. Q., Val Martin, M. and Zeng, X. (2019), 'The Community Land Model Version 5: Description of New Features, Benchmarking,

and Impact of Forcing Uncertainty', *Journal of Advances in Modeling Earth Systems* **11**(12), 4245–4287.

Lawrence, D. M., Fisher, R. A., Koven, C., Oleson, K. W., Swenson, S. C. and Vertenstein, M. (2018), Technical Description of version 5.0 of the Community Land Model (CLM), Technical report, National Center for Atmospheric Research (NCAR).

Lawrence, P. J. and Chase, T. N. (2007), 'Representing a new MODIS consistent land surface in the Community Land Model (CLM 3.0)', *Journal of Geophysical Research: Biogeosciences* **112**(1).

Leblanc, S. G., Chen, J. M., Fernandes, R., Deering, D. W. and Conley, A. (2005), 'Methodology comparison for canopy structure parameters extraction from digital hemispherical photography in boreal forests', *Agricultural and Forest Meteorology* **129**(3-4), 187–207.

Lehning, M., Bartelt, P., Brown, B. and Fierz, C. (2002), 'A physical SNOWPACK model for the Swiss avalanche warning Part III: meteorological forcing, thin layer formation and evaluation', *Cold regions science and technology* **35**, 169–184.

Lemke, P., Ren, J., Alley, R., Allison, I., Carrasco, J., Flato, G., Fujii, Y., Kaser, G., Mote, P. and Thomas, R. (2007), Observations: changes in snow, ice and frozen ground, climate change 2007: the physical science basis., *in* 'Contribution of working group I to the fourth assessment report of the intergovernmental panel on climate change.', Cambridge University Press, Cambridge, pp. 337–383.

Leonard, R. E. and Eschner, A. R. (1968), 'Albedo of Intercepted Snow', *Water Resources Research* **4**(5), 931–935.

Lhermitte, S., Abermann, J. and Kinnard, C. (2014), 'Albedo over rough snow and ice surfaces', *Cryosphere* **8**(3), 1069–1086.

Li, X., Wang, J. and Strahler, A. H. (1995), 'A hybrid geometric optical-radiative transfer approach for modeling light absorption and albedo of discontinuous canopies', *IEEE Transactions on Geoscience and Remote Sensing* **33**(2), 466–480.

Link, T. E. and Marks, D. (1999), 'Point simulation of seasonal snow cover dynamics beneath boreal forest canopies', *Journal of Geophysical Research* **104**, 27841–27857.

Link, T. E., Marks, D. and Hardy, J. P. (2004), 'A deterministic method to characterize canopy radiative transfer properties', *Hydrological Processes* **18**(18), 3583–3594.

Lohmann, U., Lüönd, F. and Mahrt, F. (2016), *An Introduction to Clouds: From the Microscale to Climate*, Cambridge University Press, Cambridge.

López-Moreno, J. I., Pomeroy, J. W., Alonso-González, E., Morán-Tejeda, E. and Revuelto, J. (2020), 'Decoupling of warming mountain snowpacks from hydrological regimes', *Environmental Research Letters* **15**(11).

López-Moreno, J. I., Vicente-Serrano, S. M., Morán-Tejeda, E., Lorenzo-Lacruz, J., Kenawy, A. and Beniston, M. (2011), 'Effects of the North Atlantic Oscillation (NAO) on combined temperature and precipitation winter modes in the Mediterranean mountains: Observed relationships and projections for the 21st century', *Global and Planetary Change* **77**(1-2), 62–76.

Loranty, M. M., Berner, L. T., Goetz, S. J., Jin, Y. and Randerson, J. T. (2014), 'Vegetation controls on northern high latitude snow-albedo feedback: Observations and CMIP5 model simulations', *Global Change Biology* **20**(2), 594–606.

Lundquist, J. D., Chickadel, C., Cristea, N., Ryan, W., Henn, B. and Keenan, E. (2018), 'Separating snow and forest temperatures with thermal infrared remote sensing', *Remote Sensing of Environment* **209**(September 2017), 764–779.

Lundquist, J. D., Dickerson-Lange, S. E., Lutz, J. A. and Cristea, N. C. (2013), 'Lower forest density enhances snow retention in regions with warmer winters: A global framework developed from plot-scale observations and modeling', *Water Resources Research* **49**(10), 6356–6370.

Mahat, V., Tarboton, D. G. and Molotch, N. P. (2013), 'Testing above- and below-canopy representations of turbulent fluxes in an energy balance snowmelt model', *Water Resources Research* **49**(2), 1107–1122.

Male, D. H. and Granger, R. J. (1981), 'Snow surface energy exchange', *Water Resour. Res.* **17**(3), 609–627.

Malle, J., Rutter, N., Mazzotti, G. and Jonas, T. (2019), 'Shading by Trees and Fractional Snow Cover Control the Subcanopy Radiation Budget', *Journal of Geophysical Research: Atmospheres* **124**(6), 3195–3207.

Malmros, J. K., Mernild, S. H., Wilson, R., Tagesson, T. and Fensholt, R. (2018), 'Snow cover and snow albedo changes in the central Andes of Chile and Argentina from daily MODIS observations (2000–2016)', *Remote Sensing of Environment* **209**(March), 240–252.

Mankin, J. S., Viviroli, D., Singh, D., Hoekstra, A. Y. and Diffenbaugh, N. S. (2015), 'The potential for snow to supply human water demand in the present and future', *Environmental Research Letters* **10**(11), 114016.

Manninen, T. and Jääskeläinen, E. (2018), 'The effect of boreal forest canopy on snow covered terrain broadband albedo', *Geophysica* **53**(1), 9–29.

Manninen, T., Jääskeläinen, E. and Riihelä, A. (2020), 'Diurnal Black-Sky Surface Albedo Parameterization of Snow', *Journal of Applied Meteorology and Climatology* pp. 1–44.

Marsh, C. B., Pomeroy, J. W. and Wheater, H. S. (2020), 'The Canadian Hydrological Model (CHM) v1.0: a multi-scale, multi-extent, variable-complexity hydrological model - design and overview', *Geoscientific Model Development* **13**(1), 225–247.

Mazzotti, G., Essery, R., Moeser, C. D. and Jonas, T. (2020), 'Resolving Small-Scale Forest Snow Patterns Using an Energy Balance Snow Model With a One-Layer Canopy', *Water Resources Research* **56**(1).

Mazzotti, G., Essery, R., Webster, C., Malle, J. and Jonas, T. (2020), 'Process-level evaluation of a hyper-resolution forest snow model using distributed multi-sensor observations', *Water Resources Research* **56**, 1–25.

Mazzotti, G., Malle, J., Barr, S. and Jonas, T. (2019), 'Spatially continuous characterization of forest canopy structure and subcanopy irradiance derived from handheld radiometer surveys', *Journal of Hydrometeorology* **20**(7), 1417–1433.

Medhaug, I., Stolpe, M. B., Fischer, E. M. and Knutti, R. (2017), 'Reconciling controversies about the 'global warming hiatus'', *Nature* **545**(7652), 41–47.

Melloh, R. A., Hardy, J. P., Bailey, R. N. and Hall, T. J. (2002), 'An efficient snow albedo model for the open and sub-canopy', *Hydrological Processes* **3584**(September), 3571–3584.

Melloh, R. A., Hardy, J. P., Davis, R. E. and Robinson, P. B. (2001), 'Spectral albedo/reflectance of littered forest snow during the melt season', *Hydrological Processes* **15**(18), 3409–3422.

Menard, C. B., Essery, R., Krinner, G., Arduini, G., Bartlett, P., Boone, A., Brutel-Vuilmet, C., Burke, E., Cuntz, M., Dai, Y., Decharme, B., Dutra, E., Fang, X., Fierz, C., Gusev, Y., Hagemann, S., Haverd, V., Kim, H., Lafaysse, M., Marke, T., Nasonova, O., Nitta, T., Niwano, M., Pomeroy, J., Schädler, G., Semenov, V., Smirnova, T., Strasser, U., Swenson, S., Turkov, D., Wever, N. and Yuan, H. (2020), 'Scientific and human errors in a snow model intercomparison', *Bulletin of the American Meteorological Society* pp. 1–46.

Meredith, M., Sommerkorn, M., Cassotta, S., Derksen, C., Ekaykin, A., Hollowed, A., Kofinas, G., Mackintosh, A., Melbourne-Thomas, J., Muelbert, M., Ottersen, G. and

Pritchard, H. (2019), Polar Regions, *in* H. Portner, D. Roberts, V. Masson-Delmotte, P. Zhai, M. Tignor, E. Poloczanska, K. Mintenbeck, A. Alegria, M. Nocolai, A. Okem, J. Petzold, B. Rama and N. Weyer, eds, 'IPCC Special Report on the Ocean and Cryosphere in a Changing Climate'.

Miller, J. (1967), 'A formula for average foliage density', *Australian Journal of Botany* **15**, 141–144.

Minder, J. R., Letcher, T. W. and Skiles, S. M. K. (2016), 'An evaluation of high-resolution regional climate model simulations of snow cover and albedo over the rocky mountains, with implications for the simulated snow-albedo feedback', *Journal of Geophysical Research* **121**(15), 9069–9088.

Moeser, D., Morsdorf, F. and Jonas, T. (2015), 'Novel forest structure metrics from airborne LiDAR data for improved snow interception estimation', *Agricultural and Forest Meteorology* **208**, 40–49.

Moeser, D., Roubinek, J., Schleppi, P., Morsdorf, F. and Jonas, T. (2014), 'Canopy closure, LAI and radiation transfer from airborne LiDAR synthetic images', *Agricultural and Forest Meteorology* **197**, 158–168.

Monin, A. S. and Obukhov, A. M. (1954), 'Basic laws of turbulent mixing in the surface layer of the atmosphere', *Q J R Meteorol Soc* **24**(151), 163–187.

Morris, E. (1989), 'Turbulent Transfer over Snow and Ice', *Journal of Hydrology* **105**, 205–223.

Mott, R., Egli, L., Grünewald, T., Dawes, N., Manes, C., Bavay, M. and Lehning, M. (2011), 'Micrometeorological processes driving snow ablation in an Alpine catchment', *Cryosphere* **5**(4), 1083–1098.

Mott, R., Schirmer, M., Bavay, M., Grünewald, T. and Lehning, M. (2010), 'Understanding snow-transport processes shaping the mountain snow-cover', *Cryosphere* **4**(4), 545–559.

Mudryk, L., Santolaria-Otín, M., Krinner, G., Ménégoz, M., Derksen, C., Brutel-Vuilmet, C., Brady, M. and Essery, R. (2020), 'Historical Northern Hemisphere snow cover trends and projected changes in the CMIP-6 multi-model ensemble', *The Cryosphere* **14**(January), 2495–2514.

Musselman, K. N., Clark, M. P., Liu, C., Ikeda, K. and Rasmussen, R. (2017), 'Slower snowmelt in a warmer world', *Nature Climate Change* **7**(3), 214–219.

Musselman, K. N., Margulis, S. A. and Molotch, N. P. (2013), 'Estimation of solar direct beam transmittance of conifer canopies from airborne LiDAR', *Remote Sensing of Environment* **136**, 402–415.

Musselman, K. N., Molotch, N. P., Margulis, S. A., Kirchner, P. B. and Bales, R. C. (2012), 'Influence of canopy structure and direct beam solar irradiance on snowmelt rates in a mixed conifer forest', *Agricultural and Forest Meteorology* **161**, 46–56.

Musselman, K. N. and Pomeroy, J. W. (2017), 'Estimation of Needleleaf Canopy and Trunk Temperatures and Longwave Contribution to Melting Snow', *Journal of Hydrometeorology* **18**(2), 555–572.

Musselman, K. N., Pomeroy, J. W. and Link, T. E. (2015), 'Variability in shortwave irradiance caused by forest gaps: Measurements, modelling, and implications for snow energetics', *Agricultural and Forest Meteorology* **207**, 69–82.

Narine, L. L., Popescu, S., Neuenschwander, A., Zhou, T., Srinivasan, S. and Harbeck, K. (2019), 'Estimating aboveground biomass and forest canopy cover with simulated ICESat-2 data', *Remote Sensing of Environment* **224**, 1–11.

Natali, S. M., Watts, J. D., Rogers, B. M., Potter, S., Ludwig, S. M., Selbmann, A. K., Sullivan, P. F., Abbott, B. W., Arndt, K. A., Birch, L., Björkman, M. P., Bloom, A. A., Celis, G., Christensen, T. R., Christiansen, C. T., Commane, R., Cooper, E. J., Crill, P., Czimczik, C., Davydov, S., Du, J., Egan, J. E., Elberling, B., Euskirchen, E. S., Friborg, T., Genet, H., Göckede, M., Goodrich, J. P., Grogan, P., Helbig, M., Jafarov, E. E., Jastrow, J. D., Kalhori, A. A., Kim, Y., Kimball, J. S., Kutzbach, L., Lara, M. J., Larsen, K. S., Lee, B. Y., Liu, Z., Loranty, M. M., Lund, M., Lupascu, M., Madani, N., Malhotra, A., Matamala, R., McFarland, J., McGuire, A. D., Michelsen, A., Minions, C., Oechel, W. C., Olefeldt, D., Parmentier, F. J. W., Pirk, N., Poulter, B., Quinton, W., Rezanezhad, F., Risk, D., Sachs, T., Schaefer, K., Schmidt, N. M., Schuur, E. A., Semenchuk, P. R., Shaver, G., Sonnentag, O., Starr, G., Treat, C. C., Waldrop, M. P., Wang, Y., Welker, J., Wille, C., Xu, X., Zhang, Z., Zhuang, Q. and Zona, D. (2019), 'Large loss of CO2 in winter observed across the northern permafrost region', *Nature Climate Change* **9**(11), 852–857.

Nerem, R. S., Beckley, B. D., Fasullo, J. T., Hamlington, B. D., Masters, D. and Mitchum, G. T. (2018), 'Climate-change–driven accelerated sea-level rise detected in the altimeter era', *Proceedings of the National Academy of Sciences of the United States of America* **115**(9), 2022–2025.

Neuenschwander, A. and Pitts, K. (2019), 'The ATL08 land and vegetation product for the ICESat-2 Mission', *Remote Sensing of Environment* **221**(April 2018), 247–259.

Nijssen, B. and Lettenmaier, D. P. (1999), 'A simplified approach for predicting shortwave radiation transfer through boreal forest canopies', *Journal of Geophysical Research Atmospheres* **104**(D22), 27859–27868.

Nobis, M. and Hunziker, U. (2005), 'Automatic thresholding for hemispherical canopy-photographs based on edge detection', *Agricultural and Forest Meteorology* **128**(3-4), 243–250.

Oleson, K. W., Lawrence, D. M., Gordon, B., Flanner, M. G., Kluzek, E., Peter, J., Levis, S., Swenson, S. C., Thornton, E., Dai, A., Decker, M., Dickinson, R., Feddema, J., Heald, C. L., Lamarque, J.-F., Niu, G.-y., Qian, T., Running, S., Sakaguchi, K., Slater, A., Stöckli, R., Wang, A., Yang, L., Zeng, X. X., Zeng, X. X., Bonan, G. B., Flanner, M. G., Kluzek, E., Lawrence, P. J., Levis, S., Swenson, S. C., Thornton, P. E., Dai, A., Decker, M., Dickinson, R., Feddema, J., Heald, C. L., Hoffman, F., Lamarque, J.-F., Mahowald, N., Niu, G.-y., Qian, T., Randerson, J., Running, S., Sakaguchi, K., Slater, A., Stöckli, R., Wang, A., Yang, Z.-L., Zeng, X. X. and Zeng, X. X. (2010), Technical Description of version 4 . 0 of the Community Land Model (CLM), Technical Report April, National Center for Atmospheric Research.

Pan, Y., Birdsey, R. A., Fang, J., Houghton, R., Kauppi, P. E., Kurz, W. A., Phillips, O. L., Shvidenko, A., Lewis, S. L., Canadell, J. G., Ciais, P., Jackson, R. B., Pacala, S. W., McGuire, A. D., Piao, S., Rautiainen, A., Sitch, S. and Hayes, D. (2011), 'A Large and Persistent Carbon Sink in the World's Forests', *Science* **333**(6045), 988–993.

Pattyn, F., Ritz, C., Hanna, E., Asay-Davis, X., DeConto, R., Durand, G., Favier, L., Fettweis, X., Goelzer, H., Golledge, N. R., Kuipers Munneke, P., Lenaerts, J. T., Nowicki, S., Payne, A. J., Robinson, A., Seroussi, H., Trusel, L. D. and van den Broeke, M. (2018), 'The Greenland and Antarctic ice sheets under 1.5 °C global warming', *Nature Climate Change* **8**(12), 1053–1061.

Petit, J. R., Jouzel, J., Raynaud, D., Barnola, J. M., Basile, I., Bender, M., Chappellaz, J., Davis, M., Delaygue, G., Delmotte, M., Kotlyakov, V. M., Legrand, M., Lipenkov, V. Y., Loriu, C., Pepin, L., Ritz, C., Saltzman, E. and Stievenard, M. (1999), 'Climate and atmospheric history of the past 420,000 years from the Vostok ice core, Antarctica', *Nature* **399**, 429–436.

Picard, G., Dumont, M., Lamare, M., Tuzet, F., Larue, F., Pirazzini, R. and Arnaud, L. (2020), 'Spectral albedo measurements over snow-covered slopes: Theory and slope effect corrections', *Cryosphere* **14**(5), 1497–1517.

Pirazzini, R. (2004), 'Surface albedo measurements over Antarctic sites in summer', *Journal of Geophysical Research D: Atmospheres* **109**(20), 1–15.

Pithan, F. and Mauritsen, T. (2014), 'Arctic amplification dominated by temperature feedbacks in contemporary climate models', *Nature Geoscience* **7**(3), 181–184.

Pohl, S., Marsh, P. and Liston, G. E. (2006), 'Spatial-temporal variability in turbulent fluxes during spring snowmelt', *Arctic, Antarctic, and Alpine Research* **38**(1), 136–146.

Pomeroy, J. and Schmidt, R. (1993), 'The use of fractal geometry in modelling intercepted snow accumulation and sublimation', *Proceedings of the Eastern Snow Conference* **50**, 1–10.

Pomeroy, J. W., Marks, D., Link, T., Ellis, C., Hardy, J., Rowlands, A. and Granger, R. (2009), 'The impact of coniferous forest temperature on incoming longwave radiation to melting snow', *Hydrological Processes* **23**(17), 2513–2525.

Pritchard, H. D. (2019), 'Asia's shrinking glaciers protect large populations from drought stress', *Nature* **569**(7758), 649–654.

Pulliainen, J., Aurela, M., Laurila, T., Aalto, T., Takala, M., Salminen, M., Kulmala, M., Barr, A., Heimann, M., Lindroth, A., Laaksonen, A., Derksen, C., Mäkelä, A., Markkanen, T., Lemmetyinen, J., Susiluoto, J., Dengel, S., Mammarella, I., Tuovinen, J.-P. and Vesala, T. (2017), 'Early snowmelt significantly enhances boreal springtime carbon uptake', *Proceedings of the National Academy of Sciences* p. 201707889.

Pulliainen, J., Luojus, K., Derksen, C., Mudryk, L., Lemmetyinen, J., Salminen, M., Ikonen, J., Takala, M., Cohen, J., Smolander, T. and Norberg, J. (2020), 'Patterns and trends of Northern Hemisphere snow mass from 1980 to 2018', *Nature* **581**(7808), 294–298.

Qi, W. and Dubayah, R. O. (2016), 'Combining Tandem-X InSAR and simulated GEDI lidar observations for forest structure mapping', *Remote Sensing of Environment* **187**(2016), 253–266.

Qin, Y., Abatzoglou, J. T., Siebert, S., Huning, L. S., AghaKouchak, A., Mankin, J. S., Hong, C., Tong, D., Davis, S. J. and Mueller, N. D. (2020), 'Agricultural risks from changing snowmelt', *Nature Climate Change* **10**(5), 459–465.

Qu, X. and Hall, A. (2007), 'What controls the strength of snow-albedo feedback?', *Journal of Climate* **20**(15), 3971–3981.

Qu, X. and Hall, A. (2014), 'On the persistent spread in snow-albedo feedback', *Climate Dynamics* **42**(1-2), 69–81.

Rautiainen, M. and Stenberg, P. (2005), 'Application of photon recollision probability in coniferous canopy reflectance simulations', *Remote Sensing of Environment* **96**(1), 98–107.

Reid, T. D. and Essery, R. L. H. (2013), 'New Methods to Quantify Canopy Structure of Leafless Boreal Birch Forest from Hemispherical Photographs', *Open Journal of Forestry* **03**(2), 70–74.

Robinson, D. A. and Frei, A. (2000), 'Seasonal Variability of Northern Hemisphere Snow Extent Using Visible Satellite Data', *Professional Geographer* **52**(2), 307–315.

Rosati, A., Wolz, K. J., Murphy, L., Ponti, L. and Jose, S. (2020), 'Modeling light below tree canopies overestimates net photosynthesis and radiation use efficiency in understory crops by averaging light in space and time', *Agricultural and Forest Meteorology* **284**, 107892.

Roth, T. R. and Nolin, A. W. (2017), 'Forest impacts on snow accumulation and ablation across an elevation gradient in a temperate montane environment', *Hydrology and Earth System Sciences* **21**(11), 5427–5442.

Rutter, N., Essery, R., Pomeroy, J., Altimir, N., Andreadis, K., Baker, I., Barr, A., Bartlett, P., Boone, A., Deng, H., Douville, H., Dutra, E., Elder, K., Ellis, C., Feng, X., Gelfan, A., Goodbody, A., Gusev, Y., Gustafsson, D., Hellström, R., Hirabayashi, Y., Hirota, T., Jonas, T., Koren, V., Kuragina, A., Lettenmaier, D., Li, W. P., Luce, C., Martin, E., Nasonova, O., Pumpanen, J., Pyles, R. D., Samuelsson, P., Sandells, M., Schädler, G., Shmakin, A., Smirnova, T. G., Stähli, M., Stöckli, R., Strasser, U., Su, H., Suzuki, K., Takata, K., Tanaka, K., Thompson, E., Vesala, T., Viterbo, P., Wiltshire, A., Xia, K., Xue, Y. and Yamazaki, T. (2009), 'Evaluation of forest snow processes models (SnowMIP2)', *Journal of Geophysical Research Atmospheres* **114**(6).

Ryan, J. C., Hubbard, A., Irvine-Fynn, T. D., Doyle, S. H., Cook, J. M., Stibal, M. and Box, J. E. (2017), 'How robust are in situ observations for validating satellite-derived albedo over the dark zone of the Greenland Ice Sheet?', *Geophysical Research Letters* **44**(12), 6218–6225.

Sailor, D. J. and Fan, H. (2002), 'Modeling the diurnal variability of effective albedo for cities', *Atmospheric Environment* **36**(4), 713–725.

Sanmiguel-Vallelado, A., Camarero, J. J., Morán-Tejeda, E., Gazol, A., Colangelo, M., Alonso-González, E. and López-Moreno, J. I. (2021), 'Snow dynamics influence tree growth by controlling soil temperature in mountain pine forests', *Agricultural and Forest Meteorology* **296**, 108205.

Sanmiguel-Vallelado, A., López-Moreno, J. I., Morán-Tejeda, E., Alonso-González, E., Navarro-Serrano, F. M., Rico, I. and Camarero, J. J. (2020), 'Variable effects of forest canopies on snow processes in a valley of the central Spanish Pyrenees', *Hydrological Processes* **34**(10), 2247–2262.

Saunois, M., Jackson, R. B., Bousquet, P., Poulter, B. and Canadell, J. G. (2016), 'The growing role of methane in anthropogenic climate change', *Environmental Research Letters* **11**(12), 1–5.

Schaaf, C., Martonchik, J., Pinty, B., Govaerts, Y., Gao, F., Lattanzio, A., Liu, J., Strahler, A. and Taberner, M. (2008), Retrieval of Surface Albedo from Satellite Sensors BT - Advances in Land Remote Sensing: System, Modeling, Inversion and Application, Springer Netherlands, Dordrecht, pp. 219–243.

Schleppi, P., Conedera, M., Sedivy, I. and Thimonier, A. (2007), 'Correcting non-linearity and slope effects in the estimation of the leaf area index of forests from hemispherical photographs', *Agricultural and Forest Meteorology* **144**(3-4), 236–242.

Schuur, E. A. G., McGuire, A. D., Schädel, C., Grosse, G., Harden, J. W., Hayes, D. J., Hugelius, G., Koven, C. D., Kuhry, P., Lawrence, D. M., Natali, S. M., Olefeldt, D., Romanovsky, V. E., Schaefer, K., Turetsky, M. R., Treat, C. C. and Vonk, J. E. (2015), 'Climate change and the permafrost carbon feedback', *Nature* **520**(7546), 171–179.

Sellers, P. J. (1985), 'Canopy reflectance, photosynthesis and transpiration', *International Journal of Remote Sensing* **68**(68), 1335–1372.

Sellers, P. J., Mintz, Y., Sud, Y. and Dalcher, A. (1986), 'A Simple Biosphere Model (SiB) for Use within General Circulation Models', *Journal of the Atmospheric Sciences.* **43**(6), 505–531.

Serreze, M. C., Barrett, A. P., Stroeve, J. C., Kindig, D. N. and Holland, M. M. (2009), 'The emergence of surface-based Arctic amplification', *Cryosphere* **3**(1), 11–19.

Serreze, M. C., Walsh, J. E., Chapin, F. S., Osterkamp, T., Dyurgerov, M., Romanovsky, V., Oechel, W. C., Morison, J., Zhang, T. and Barry, R. G. (2000), 'Observational Evidence of Recent Change in the Northern High-Latitude Environment', *Climatic Change* **46**, 159–207.

Seyednasrollah, B. and Kumar, M. (2014), 'Net radiation in a snow-covered discontinuous forest gap for a range of gap sizes and topographic configurations', *Journal of Geophysical Research Atmospheres* **119**, 10323 – 10342.

Sicart, J. E., Essery, R. L. H., Pomeroy, J. W., Hardy, J., Link, T. and Marks, D. (2004), 'A Sensitivity Study of Daytime Net Radiation during Snowmelt to Forest Canopy and Atmospheric Conditions', *Journal of Hydrometeorology* **5**, 774–784.

Sicart, J. E., Pomeroy, J. W., Essery, R. L. H. and Bewley, D. (2006), 'Incoming long-wave radiation to melting snow: observations, sensitivity and estimation in northern environments', *Hydrological Processes* **20**(November 2008), 3697–3708.

Skiles, S. M. K., Flanner, M., Cook, J. M., Dumont, M. and Painter, T. H. (2018), 'Radiative forcing by light-absorbing particles in snow', *Nature Climate Change* **8**(11), 964–971.

Slater, A. G., Pitman, A. J. and Desborough, C. E. (1998), 'The validation of a snow parameterization designed for use in general circulation models', *International Journal of Climatology* **18**(6), 595–617.

Stähli, M., Jonas, T. and Gustafsson, D. (2009), The role of snow interception in winter-time radiation processes of a coniferous sub-alpine forest, *in* 'Hydrological Processes', Vol. 23, pp. 2498–2512.

Stott, P. (2016), 'How climate change affects extreme weather events', *Science* **352**(6293), 1517–1518.

Sturm, M., Goldstein, M. and Parr, C. (2017), 'Water and life from snow: A trillion dollar science question', *Water Resources Research* **53**, 3534–3544.

Sturm, M., Taras, B., Liston, G. E., Derksen, C., Jonas, T. and Lea, J. (2010), 'Estimating snow water equivalent using snow depth data and climate classes', *Journal of Hydrometeorology* **11**(6), 1380–1394.

Sun, N., Wigmosta, . M., Zhou, T., Lundquist, J., Dickerson-Lange, S., Cristea, . N., Wigmosta, M., Zhou, T., Sun, N., Cristea, N., Lange, S. D. and Lundquist, J. (2018), 'Evaluating the functionality and streamflow impacts of explicitly modelling forest – snow interactions and canopy gaps in a distributed hydrologic model', *Hydrological Processes* **32**(February), 2128–2140.

Sun, S., Jin, J. and Xue, Y. (1999), 'A simple snow-atmosphere-soil transfer model', *Journal of Geophysical Research Atmospheres* **104**(D16), 19587–19597.

Swann, A. L., Fung, I. Y., Levis, S., Bonan, G. B. and Doney, S. C. (2010), 'Changes in arctic vegetation amplify high-latitude warming through the greenhouse effect', *Proceedings of the National Academy of Sciences of the United States of America* **107**(4), 1295–1300.

Swenson, S. C. and Lawrence, D. M. (2012), 'A new fractional snow-covered area parameterization for the Community Land Model and its effect on the surface energy balance', *Journal of Geophysical Research Atmospheres* **117**(21), 1–20.

Thackeray, C. W., Derksen, C., Fletcher, C. G. and Hall, A. (2019), 'Snow and Climate: Feedbacks, Drivers, and Indices of Change', *Current Climate Change Reports* **5**(4), 322–333.

Thackeray, C. W. and Fletcher, C. G. (2016), 'Snow albedo feedback: Current knowledge, importance, outstanding issues and future directions', *Progress in Physical Geography* **40**(3), 392–408.

Todt, M., Rutter, N., Fletcher, C. G., Wake, L. M., Bartlett, P. A., Jonas, T., Kropp, H., Loranty, M. M. and Webster, C. (2018), 'Simulation of Longwave Enhancement in Boreal and Montane Forests', *Journal of Geophysical Research: Atmospheres* **123**(24), 13,731–13,747.

Toon, O. B., McKay, C. P., Ackerman, T. P. and Santhanam, K. (1989), 'Rapid calculation of radiative heating rates and photodissociation rates in inhomogeneous multiple scattering atmospheres', *Journal of Geophysical Research* **94**(D13), 287–301.

Trujillo, E., Molotch, N. P., Goulden, M. L., Kelly, A. E. and Bales, R. C. (2012), 'Elevation-dependent influence of snow accumulation on forest greening', *Nature Geoscience* **5**(10), 705–709.

Van Den Hurk, B., Kim, H., Krinner, G., Seneviratne, S. I., Derksen, C., Oki, T., Douville, H., Colin, J., Ducharne, A., Cheruy, F., Viovy, N., Puma, M. J., Wada, Y., Li, W., Jia, B., Alessandri, A., Lawrence, D. M., Weedon, G. P., Ellis, R., Hagemann, S., Mao, J., Flanner, M. G., Zampieri, M., Materia, S., Law, R. M. and Sheffield, J. (2016), 'LS3MIP (v1.0) contribution to CMIP6: The Land Surface, Snow and Soil moisture Model Intercomparison Project - Aims, setup and expected outcome', *Geoscientific Model Development* **9**(8), 2809–2832.

Varhola, A., Coops, N. C., Weiler, M. and Moore, R. D. (2010), 'Forest canopy effects on snow accumulation and ablation: An integrative review of empirical results', *Journal of Hydrology* **392**(3-4), 219–233.

Vaughan, D., Comiso, J., Allison, I., Carrasco, J., Kaser, G., Kwok, R., Mote, P., Murray, T., Paul, F., Ren, J., Rignot, E., Solomina, O., Steffen, K. and Zhang, T. (2013), Observations: Cryosphere, *in* Intergovernmental Panel on Climate Change, ed., 'Climate Change 2013 - The Physical Science Basis', Cambridge University Press, Cambridge, pp. 317–382.

Verseghy, D. L., McFarlane, N. A. and Lazare, M. (1993), 'Class—A Canadian land surface scheme for GCMS, II. Vegetation model and coupled runs', *International Journal of Climatology* **13**(4), 347–370.

Vrugt, J. A., Bouten, W., Dekker, S. C. and Musters, P. A. D. (2002), 'Transpiration dynamics of an Austrian Pine stand and its forest floor: identifying controlling conditions using artificial neural networks', *Advances in Water Resources* **25**, 293–303.

Wang, L., Cole, J. N. S., Bartlett, P., Verseghy, D., Derksen, C., Brown, R., Von Salzen, K. and Salzen, K. (2016), 'Investigating the spread in surface albedo for snow-covered forests in CMIP5 models', *Journal of Geophysical Research* **121**, 1104–1119.

Wang, Z., Erb, A. M., Schaaf, C. B., Sun, Q., Liu, Y., Yang, Y., Shuai, Y., Casey, K. A. and Román, M. O. (2016), 'Early spring post-fire snow albedo dynamics in high latitude boreal forests using Landsat-8 OLI data', *Remote Sensing of Environment* **185**, 71–83.

Wang, Z., Zeng, X., Barlage, M., Dickinson, R., Gao, F. and Schaaf, C. (2004), 'Using MODIS BRDF and Albedo Data to Evaluate Global Model Land Surface Albedo', *Journal of Hydrometeorology* **5**, 3–14.

Warren, S. G. (1982), 'Optical properties of snow', *Reviews of Geophysics* **20**(1), 67–89.

Webster, C. and Jonas, T. (2018), 'Influence of canopy shading and snow coverage on effective albedo in a snow-dominated evergreen needleleaf forest', *Remote Sensing of Environment* **214**(May), 48–58.

Webster, C., Mazzotti, G., Essery, R. and Jonas, T. (2020), 'Enhancing airborne LiDAR data for improved forest structure representation in shortwave transmission models', *Remote Sensing of Environment* **249**(July), 112017.

Webster, C., Rutter, N. and Jonas, T. (2017), 'Improving representation of canopy temperatures for modeling subcanopy incoming longwave radiation to the snow surface', *Journal of Geophysical Research: Atmospheres* **122**(17), 9154–9172.

Webster, C., Rutter, N., Zahner, F. and Jonas, T. (2016*a*), 'Measurement of Incoming Radiation below Forest Canopies : A Comparison of Different Radiometer Configurations', *Journal of Hydrometeorology* **17**, 853–864.

Webster, C., Rutter, N., Zahner, F. and Jonas, T. (2016*b*), 'Modeling subcanopy incoming longwave radiation to seasonal snow using air and tree trunk temperatures', *Journal of Geophysical Research* **121**(3), 1220–1235.

Webster, C., Westoby, M., Rutter, N. and Jonas, T. (2018), 'Three-dimensional thermal characterization of forest canopies using UAV photogrammetry', *Remote Sensing of Environment* **209**(March 2017), 835–847.

Weihs, P., Lenoble2, J., Blumthaler, M., Martin, T., Seckmeyer5, G., Lenoble, J., Blumthaler, M., Martin, T., Seckmeyer, G., Casiniere, A. D., Sergent, C., Pichler, T., Pougatch, E., Rengarajan, G., Schmucki, D. and Simic, S. (2001), 'Modeling the effect of an inhomogeneous surface albedo on incident UV radiation in mountaineous terrain: determination of an effective surface albedo', **28**(16), 3111–3114.

White, I., Mottershead, D. and Harrison, S. (1998), *Environmental Systems. An introductory text.*, 2 edn, Stanley Thornes, Cheltenham.

Wild, M., Ohmura, A., Gilgen, H., Morcrette, J. J. and Slingo, A. (2001), 'Evaluation of downward longwave radiation in general circulation models', *Journal of Climate* **14**(15), 3227–3239.

Wilks, D. S. (2006), *Statistical Methods in the Atmospheric Sciences*, 2nd ed. edn, Academic press.

Williams, M., Richardson, A. D., Reichstein, M., Stoy, P. C., Peylin, P., Verbeeck, H., Carvalhais, N. and Jung, M. (2009), 'Improving land surface models with FLUXNET data', *Biogeosciences* **6**, 1341–1359.

Winkler, R., Boon, S., Zimonick, B. and Baleshta, K. (2010), 'Assessing the effects of post-pine beetle forest litter on snow albedo', *Hydrological Processes* **24**(6), 803–812.

Wiscombe, W. and Warren, S. (1980), 'A Model for the Spectral Albedo of Snow. I: Pure Snow', *Journal of the Atmospheric Sciences.* **37**, 2712–2733.

WMO (2020), State of the Global Climate 2020 (Provisional report), Technical report, World Meteorological Organization (WMO).

Wolter, P. T., Berkley, E. A., Peckham, S. D., Singh, A. and Townsend, P. A. (2012), 'Exploiting tree shadows on snow for estimating forest basal area using Landsat data', *Remote Sensing of Environment* **121**, 69–79.

Wu, C., Liu, X., Lin, Z., Rhoades, A. M., Ullrich, P. A., Zarzycki, C. M., Lu, Z. and Rahimi-Esfarjani, S. R. (2017), 'Exploring a Variable-Resolution Approach for Simulating Regional Climate in the Rocky Mountain Region Using the VR-CESM', *Journal of Geophysical Research: Atmospheres* **122**(20), 10,939–10,965.

Xie, Z., Hu, Z., Ma, Y., Sun, G., Gu, L., Liu, S., Wang, Y., Zheng, H. and Ma, W. (2019), 'Modeling Blowing Snow Over the Tibetan Plateau With the Community Land Model: Method and Preliminary Evaluation', *Journal of Geophysical Research: Atmospheres* **124**(16), 9332–9355.

Yang, F., Mitchell, K., Hou, Y. T., Dai, Y., Zeng, X., Wang, Z. and Liang, X. Z. (2008), 'Dependence of land surface albedo on solar zenith angle: Observations and model parameterization', *Journal of Applied Meteorology and Climatology* **47**(11), 2963–2982.

Yuan, H., Dai, Y., Dickinson, R. E., Pinty, B., Wei, S., Zhang, S., Wang, L. and Zhu, S. (2017), 'Reexamination and further development of two-stream canopy radiative transfer models for global land modeling', *Journal of Advances in Modeling Earth Systems* **9**, 113–129.

Yuan, H., Dickinson, R. E., Dai, Y., Shaikh, M. J., Zhou, L., Shangguan, W. and Ji, D. (2014), 'A 3D canopy radiative transfer model for global climate modeling: Description, validation, and application', *Journal of Climate* **27**(3), 1168–1192.

Zarzycki, C. M. and Jablonowski, C. (2014), 'A multidecadal simulation of Atlantic tropical cyclones using a variable-resolution global atmospheric general circulation model', *Journal of Advances in Modeling Earth Systems* **6**, 805–828.

Zellweger, F., Baltensweiler, A., Schleppi, P., Huber, M., Küchler, M., Ginzler, C. and Jonas, T. (2019), 'Estimating below-canopy light regimes using airborne laser scanning: An application to plant community analysis', *Ecology and Evolution* **9**(16), 9149–9159.

Zhang, D. L., Lin, Y., Zhao, P., Yu, X., Wang, S., Kang, H. and Ding, Y. (2013), 'The Beijing extreme rainfall of 21 July 2012: Right results but for wrong reasons', *Geophysical Research Letters* **40**(7), 1426–1431.

Zhang, T. (2005), 'Influence of the seasonal snow cover on the ground thermal regime: an overview', *Rev. Geophys.* **43**(June), 1–5.

Zhang, Y., Chen, J. M. and Miller, J. R. (2005), 'Determining digital hemispherical photograph exposure for leaf area index estimation', *Agricultural and Forest Meteorology* **133**(1-4), 166–181.

Zhang, Z., Zimmermann, N. E., Stenke, A., Li, X., Hodson, E. L., Zhu, G., Huang, C. and Poulter, B. (2017), 'Emerging role of wetland methane emissions in driving 21st century climate change', *Proceedings of the National Academy of Sciences of the United States of America* **114**(36), 9647–9652.

Zhao, H. and Moore, G. W. (2004), 'On the relationship between Tibetan snow cover, the Tibetan plateau monsoon and the Indian summer monsoon', *Geophysical Research Letters* **31**(14), 1–4.

Zhu, B., Huang, M., Cheng, Y., Xie, X., Liu, Y., Zhang, X., Bisht, G., Chen, X., Missik, J. and Liu, H. (2020), 'Effects of irrigation on water, carbon, and nitrogen budgets in a

semi-arid watershed in the Pacific Northwest: A modelling study', *Journal of Advances in Modeling Earth Systems* **12**, 1–20.